# UC Irvine
## UC Irvine Electronic Theses and Dissertations

**Title**
Mathematical and Computational Models of Fluctuating Vesicles in Time-Varying Flows

**Permalink**
https://escholarship.org/uc/item/10x7234q

**Author**
Wang, Wei

**Publication Date**
2019

Peer reviewed|Thesis/dissertation

UNIVERSITY OF CALIFORNIA,
IRVINE


Mathematical and Computational Models of Fluctuating Vesicles in Time-Varying Flows

DISSERTATION


submitted in partial satisfaction of the requirements
for the degree of


DOCTOR OF PHILOSOPHY

in Mathematics


by


Wei Wang


Dissertation Committee:
Professor John Lowengrub, Chair
Professor Long Chen
Professor Qing Nie


2019

# TABLE OF CONTENTS

# LIST OF FIGURES

# LIST OF TABLES

# ACKNOWLEDGMENTS

First and foremost, I would like to express my sincere gratitude to my advisor Prof. John Lowengrub for the continuous support of my Ph.D. study and related research, for his patience, motivation, and immense knowledge. His guidance helped me in all the time of research and writing of this thesis. I could not have imagined having a better advisor and mentor for my Ph.D. study.

Besides my advisor, I would like to thank the rest of my thesis committee: Prof. A, Prof. B, for their insightful comments and encouragement, and helpful questions.

During the past six years of study at UCI, the Math Department gave me lots of support and help. Here I would like to thank all professors who taught me, Prof. John Lowengrub on asymptotic analysis, Prof. Long Chen on computational PDEs, Prof. Hongkai Zhao on numerical methods, Prof. Frederic Wan on stochastic differential equations.

I would like to thank Dr. Kai Liu for the stimulating discussions and his valuable suggestions and feedback on my research. Many thanks to Min Wen, Fei Yu, Zhenlin Guo, and other students in the Math Department.

Last but not least, I would like to thank my family for all their love and encouragement. For my parents, who raised me with a love of science and supported me in all my pursuits. And for my fiancé who faithfully supported me during the final stage of this Ph.D. Thank you.

# CURRICULUM VITAE

## Wei Wang

**EDUCATION**

**Doctor of Philosophy in Mathematics** **2019**
The University of California, Irvine *Irvine, CA*

**Master of Science in Mathematics** **2015**
The University of California, Irvine *Irvine, CA*

**Master of Science in Mathematics** **2013**
The University of Science and Technology of China *Hefei, China*

**Bachelor of Science in Mathematics** **2011**
The University of Science and Technology of China *Hefei, China*

**RESEARCH EXPERIENCE**

**Graduate Research Assistant** **2015–2019**
The University of California, Irvine *Irvine, California*

**TEACHING EXPERIENCE**

**Teaching Assistant** **2016–2019**
The University of California, Irvine *Irvine, California*

# ABSTRACT OF THE DISSERTATION

Mathematical and Computational Models of Fluctuating Vesicles in Time-Varying Flows

By

Wei Wang

Doctor of Philosophy in Mathematics

University of California, Irvine, 2019

Professor John Lowengrub, Chair

Modeling vesicle dynamics involves a complicated moving boundary problem while the shapes of vesicles are determined dynamically from a balance between interfacial forces and fluid stresses. In this thesis, we investigate the dynamics of a two-dimensional fluctuating vesicle in a viscous fluid.

Firstly we develop a two-dimensional stochastic immersed boundary method (SIBM) and analyze thermal fluctuations by matching the numerical results with a theoretical solution [46]. Then we apply the SIBM with fitted thermal fluctuations to study the long term dynamics of an impermeable vesicle in a periodically time-reversed flow. The wrinkling process contains three stages. In the first stage, high-order modes are excited by the negative surface tension and wrinkles appear. In the second stage, low Fourier modes increase, the high-order wrinkles decay, and the shapes of vesicles keep relatively stable. In the last stage, the second Fourier mode grows and dominates. The shapes of the vesicle are ellipse-like with inclination angle $\theta \approx 45°$. Then by performing an asymptotic linear analysis of a quasi-circular vesicle, we derive and solve the deterministic and stochastic equations for the motion of membrane interface numerically. The linear theory also indicates this three stage process.

Finally, we investigate the nonlinear wrinkling dynamics of a permeable vesicle using an

extension of the SIBM. We observe the vesicle shrinkage and the wrinkles on the membrane caused by a large osmosis pressure. We extend the linear theory to account for permeability and find a good agreement between linear and fully nonlinear vesicle dynamics.

# Chapter 1

# Introduction

## 1.1 Background

### 1.1.1 Biomembranes and Red Blood Cell

Biomembranes are enclosing or separating membranes that act as selectively permeable barriers within living beings [11, 2]. For example, a cell is bounded by a plasma membrane which separates the interior of the cell from the outside environment. The plasma membrane is primarily composed of bilayer amphiphilic molecules, in which proteins are usually embedded. This enables the membrane to protect intracellular components from the extracellular environment, transport nutrients and toxic substances between the cell, and adjust its shape according to the environment. Figure 1.1 illustrates the components for which a biomembrane is made.

Many important physiological processes occur on the cell membrane or are adjusted by the cell membrane, like immune response, signal transduction, and transmission of substances [11]. Because of the complicated internal structures of a normal cell, the role of the cell
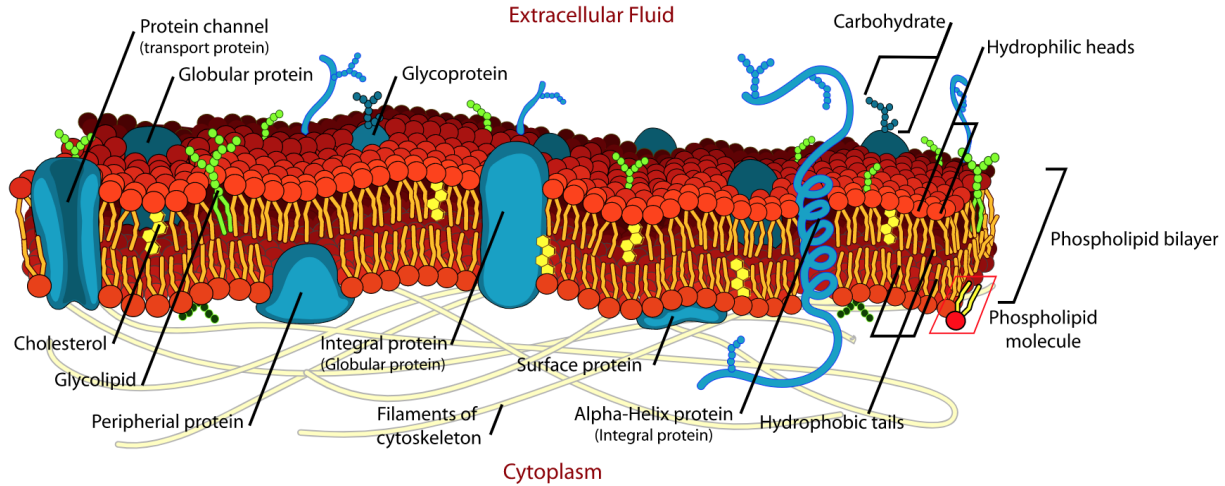
Figure 1.1: Cartoon of a cell membrane.

membrane is still not known precisely. As a simple model, biologists have focused on the red blood cell (RBC) which lacks a cell nucleus and most organelles, to accommodate maximum space for hemoglobin [20]. A typical RBC only contains hemoglobin that is used to carry oxygen and saline solution.

## 1.1.2 Vesicles

Although the structure of RBC is relatively simple, there are still two components: the phospholipid membrane and the cytoskeleton. Since there is no protein or cytoskeleton, vesicles serve most often as models to study red blood cell dynamics and membrane biophysics [36, 37, 17, 1]. For example, a giant unilamellar vesicle is used to mimic essential characteristics of the red blood cell, such as its equilibrium biconcave shape.

A giant unilamellar lipid vesicle (see Figure 1.2), is a small structure within a cell. It consists of fluid enclosed by a lipid bilayer. Besides, vesicles play a critical role in the processes of secretion (exocytosis), uptake (phagocytosis and endocytosis) and transport of materials within the cytoplasm [4]. Vesicles also function as containers for biochemical reactions

[45, 28], and vectors for targeted drug and gene delivery [3, 22].
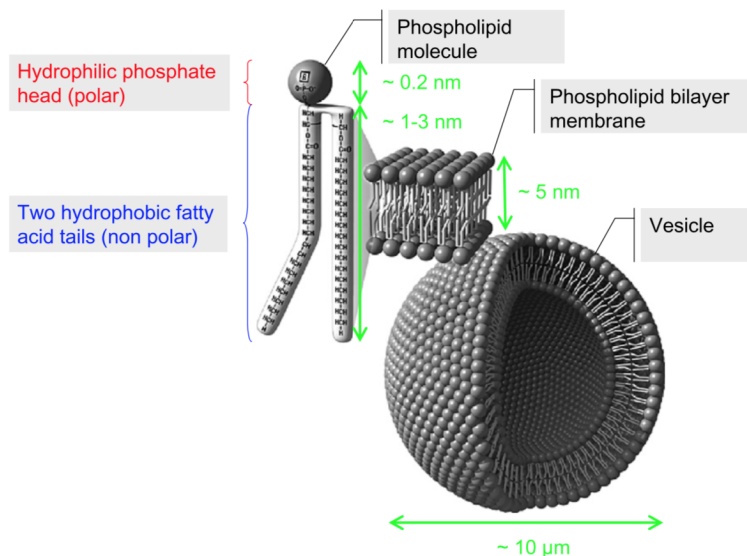


Figure 1.2: Cartoon of a vesicle and the molecular structure of its membrane.

Scientists concentrate on synthesizing vesicles by a variety of molecules. Whereas theoretical researchers are focused more on the shape of the vesicle, dynamics, phase separations, etc. Recently, a transient wrinkling dynamics of a vesicle in external elongation flow has been observed by Kantsler [27]. It was found that high-order deformation modes can be excited transiently by the negative surface tension if the direction of the applied flow is suddenly reversed [57]. However, the wrinkles are not stationary and are excited only for a limited amount of time. They are smoothed out once the surface tension becomes positive again and the vesicle aligns with the new extensional flow direction. So we want to see whether we can modify the shapes of the vesicle by reversing the direction of the flow periodically. In this thesis, we study the wrinkling dynamics of vesicles, subjected to time-varying applied flows.

## 1.2 Related Work

Due to the importance of vesicles and their applications in biomedicine, the dynamics of vesicles in a viscous fluid has become an important research topic. Scientists have tried to explain the shapes and dynamics of the vesicles using analytical and numerical approaches.

The analytic work started from an investigation of the biconcave shape of a red blood cell. Helfrich improved Canham's model of the local free energy of the RBC membranes to [12, 25]

$$E_\kappa = \frac{1}{2} \int \big(\kappa(H - C_0)^2 + \kappa_G K\big) dA, \tag{1.1}$$

where $\kappa$ is the bending rigidity, $\kappa_G$ is the Gaussian bending rigidity, $H$ is the mean curvature, and $K$ is the Gaussian curvature. Because the Gaussian curvature depends only on the genus number of the surface (Gauss-Bonnet formula), Gaussian curvature can be neglected when the topological structure of the membrane remains unchanged or the Gaussian bending rigidity is uniform.

In 1987, Helfrich and Ou-Yang added the volume and area constraints into the model [64],

$$E_\kappa = \frac{1}{2} \int \big(\kappa(H - C_0)^2 + \kappa_G K + \sigma\big) dA + \Delta P V, \tag{1.2}$$

where $\sigma$ is the surface tension, $\Delta P$ is the osmotic pressure jump between the inner and outer fluid, and $V$ is the volume enclosed by the membrane. By taking the variational derivative of the free energy [64] and solving the corresponding Euler-Lagrange equation for the equilibrium shapes [43], they got a biconcave shape similar to RBCs.

Afterward, following Helfrich free energy model, more continuum models have been developed. Many previous studies focus on a quasi-spherical vesicle and describe the shape of

the vesicles as an expression of spherical harmonics, e.g., [52, 33, 57]. For two dimensional models, the Fourier series is used to describe the quasi-circular shape of a vesicle [19, 39]. Although the asymptotic linear theory is developed for quasi-spherical vesicles, the theory accurately describes for elongated vesicles and matches with experimental results [33, 27, 16, 39]. More recently thermal, fluctuations have been included in the analysis [19, 35].

Because the Helfrich-type models are highly nonlinear and involve high-order equations, numerical methods are needed to describe the fully nonlinear dynamics. These methods mainly differ in their representation of the interface, e.g., the boundary integral method [60, 59], the phase-field method [10], the level set methods [26, 13, 63, 14, 40], grid-based particle methods[34], etc.

The immersed boundary method (IBM) was first developed by Peskin in 2002[49]. Then lots of variants of IBM have been developed [58, 23]. Later thermal fluctuations were incorporated[31]. Moreover, Atzberger extended IBM to stochastic immersed boundary methods(SIBM) and simulate the interactions between fluids structures and thermal fluctuations [5, 8, 6]. This method has been further utilized to study the dynamics of a vesicle in external flows [18, 38].

By coupling the Euler and Lagrange coordinates, IBM overcomes two major problems for moving boundary problems- the difficulty to fit simple orthogonal grids to a moving boundary, and the complicated grid generation and corresponding high computational time. And the thermal fluctuations can be incorporated straightforwardly.

## 1.3 Major Achievements

In this thesis, we study the dynamics of a 2D vesicle in a viscous fluid.

- We investigate and analyze thermal fluctuations in two dimensions. Because the scaling of 2D and 3D thermal fluctuations are different, to achieve a proper 2D thermal fluctuation, we define a spatial scale $L_d$ and choose it by matching the nonlinear results of a fluctuating filament with a theoretical formula [46].

- We identify a nonlinear relationship between the spatial scale and the computational domain size numerically and theoretically.

- We observe a three-stage process of the long-term wrinkling dynamics of an impermeable vesicle in a periodically time-varying flow, and achieve a good agreement with the linear analysis. We examine the effects of different parameters.

- We develop a stochastic immersed boundary method to study the wrinkling dynamics of a permeable vesicle. We observe the vesicle shrinkage and wrinkles on the membrane.

- We perform a linear theory on the dynamics of a quasi-circular permeable vesicle. We derive and solve the equation system of motion for the shape perturbation terms numerically.

## 1.4  Overview of this Thesis

This thesis is organized as follows.

In Chapter 2, we develop a 2D stochastic immersed boundary method (SIBM) to simulate the wrinkling dynamics of a fluctuating vesicle in a viscous fluid by appropriately defining a spatial scale $L_d$ for a two-dimensional thermal force. We compute the spatial scale $L_d$ by matching numerical results with a theoretical solution [46] for a fluctuating filament. We investigate how $L_d$ depends on the computational domain size and formulate a theory to explain the results.

In Chapter 3, we apply the stochastic immersed boundary method with the suitable spatial scale $L_d$ to compute the wrinkling dynamics of a fluctuating vesicle in a viscous fluid with a time-varying flow. Then we apply a linear approach to analyze the wrinkling dynamics induced by reversing the direction of extensional flow of a quasi-circular vesicle. We solve the equation system for the shape perturbations numerically and compare the solution with the nonlinear results.

In Chapter 4, we investigate the dependence of the wrinkling dynamics with the extensional flow strength $S$ and the threshold $C_h$.

In Chapter 5, we focus on the dynamics of vesicles with a semi-permeable membrane. We simulate the osmotic pressure relevant to the vesicles and extend the Stochastic Immersed Boundary Methods (SIBM) to study the wrinkling dynamics of a vesicle with a permeable membrane. Then we present a linear theory for quasi-circular vesicles, and the analysis achieves good agreement with the nonlinear simulation.

In Chapter 6, we review the entire thesis and results. In the end, we present future work.

# Chapter 2

# Immersed Boundary Method and A Spatial Scale $L_d$

In this chapter, we formulate a stochastic immersed boundary method (SIBM) to simulate the wrinkling dynamics of a fluctuating 2D vesicle in a time-varying flow. The wrinkles are induced by instantaneous changing the direction of an applied extensional flow [27]. We define a spatial scale $L_d$ to consistently develop a model of thermal fluctuations in 2D. To choose $L_d$, we match the average equilibrium length of a fluctuating filament obtained from the stochastic immersed boundary method with the theoretical length of a fluctuating filament calculated by Odijk [46]. We determine how $L_d$ depends on the computational domain size and develop an analytical theory to explain the result.

## 2.1  Stochastic Immersed Boundary Methods (SIBM)

The main idea of the Immersed Boundary Method (IBM) is to use a Dirac delta function to couple the fluid and structure and reduce the complexity of the nonlinear moving boundary

problem. As such, the IBM provides a convenient method for simulating fluid-structure interactions. Because thermal fluctuations in the aqueous environment become significant at the small length scale of vesicles, which is on the order of micrometers, the IBM has been extended to account for thermal fluctuations [5, 8, 6]. Because the length scale is small, Reynolds number is very small. We can neglect the nonlinear advection term in the fluid equation. As the dynamical time scales arising from Brownian motion, in general, are fast, we will not drop the time derivative term of the velocity [8].

The time-dependent Stokes equations for an incompressible viscous fluid are [5, 8, 6, 30]

$$\rho\frac{\partial \mathbf{u}}{\partial t} = \eta\nabla^2\mathbf{u} - \nabla p + \mathbf{f}_{\text{total}}, \tag{2.1}$$

$$\nabla \cdot \mathbf{u} = 0. \tag{2.2}$$

Where $\mathbf{u}$ is the velocity of the fluid, $\rho$ is the uniform fluid density, $p$ is the pressure, $\eta$ is the viscosity and $\mathbf{f}_{\text{total}}$ is the total force density acting on the fluid.

The force density $\mathbf{f}_{\text{total}}$ arises from two sources. The first one is the force applied to the fluid by the immersed structure (the membrane). This component of the force density results from the elastic deformations of immersed structure (the membrane), denoted as $\mathbf{f}_{\text{mem}}$. The second one is the force that arises from thermal fluctuations, denoted by $\mathbf{f}_{\text{thm}}$. That is

$$\mathbf{f}_{\text{total}} = \mathbf{f}_{\text{mem}} + \mathbf{f}_{\text{thm}}. \tag{2.3}$$

Let $\mathbf{X}$ be the configuration of the structure (the membrane), $\mathbf{F_X}$ be the elastic force density on the membrane, then

$$\mathbf{f}_{\text{mem}} = \Lambda(\mathbf{F_X}), \tag{2.4}$$

$$\frac{d\mathbf{X}}{dt} = \Upsilon(\mathbf{u}), \tag{2.5}$$

9

where $\Lambda$ and $\Upsilon$ are linear structure-fluid coupling operators,

$$\Lambda\left(\mathbf{F_X}\right) = \int_{S(t)} \mathbf{F_X}(t)\delta_a(\mathbf{x} - \mathbf{X}(s,t))ds, \tag{2.6}$$

$$\Upsilon(\mathbf{u}) = \int_{D} \mathbf{u}(\mathbf{x},t)\delta_a(\mathbf{x} - \mathbf{X}(s,t))d\mathbf{x}. \tag{2.7}$$

See [6] for a complete derivation.

## 2.1.1    Free Energy and Elastic Force Density $\mathbf{F_X}$

The free energy of a two-dimensional vesicle [25] is

$$E = E_b + E_\sigma, \tag{2.8}$$

where $E_b$ is the bending energy, given by

$$E_b = \frac{1}{2}\int_{\mathcal{S}(t)} \kappa H^2 ds, \tag{2.9}$$

where $\kappa$ is the bending rigidity, and $H$ is the mean curvature. $E_\sigma$ is the elastic energy used to ensure the arc length constraint, given by

$$E_\sigma = \int_{\mathcal{S}(t)} \sigma ds, \tag{2.10}$$

where $\sigma$ is the elastic tension, which can be considered as a Lagrange multiplier to ensure the membrane is inextensible (local and global length do not change). Note that $E_b$ and $E_\sigma$ have the same form as in 3D but are surface integrals in 3D.

The elastic force density $\mathbf{F_X}$ is the variational derivative of the elastic energy $E$ [48],

$$\mathbf{F_X} = -\frac{\delta E}{\delta \mathbf{X}} = \left( \kappa \frac{\partial^2 H}{\partial s^2} + \frac{\kappa}{2} H^3 - H\sigma \right) \mathbf{n} + \frac{\partial \sigma}{\partial s} \mathbf{t}, \tag{2.11}$$

where $\mathbf{n}$ is the outward normal vector and $\mathbf{t}$ is the tangent vector. A detailed derivation is given in Appendix A.1 and reference [48].

## 2.1.2 Thermal Fluctuations

The influence of thermal fluctuations on a mechanical system is typically represented by the addition of a thermal forcing term $\mathbf{f}_{\mathrm{thm}}$, which decorrelates rapidly in time. The stochastic forcing $\mathbf{f}_{\mathrm{thm}}$ can be represented by an approximation of the 'white-noise' process. Here we assume that the (impermeable) membrane moves with the fluid, so there is an energy balance between the thermal force and dissipation of the system. A corresponding fluctuation-dissipation theorem for the system is satisfied [32].

In three dimensions, to ensure mass and momentum conservation, $\mathbf{f}_{\mathrm{thm}}$ is proportional to the divergence of a stochastic flux $\mathbf{W}$[5, 8, 9, 51, 15].

$$\mathbf{f}_{\mathrm{thm}} = \sqrt{\eta k_{\mathrm{B}} T} \nabla \cdot \mathbf{W}, \tag{2.12}$$

where $\mathbf{W}$ denotes a stochastic flux that is modeled as a white-noise Gaussian random tensor with uncorrelated components

$$\langle W_{ij}(\mathbf{x}, t) W_{kl}(\mathbf{y}, \tau) \rangle = 2\delta_{ik}\delta_{jl}\delta_{\mathbf{x}}(\mathbf{x} - \mathbf{y})\delta_t(t - \tau), \tag{2.13}$$

here $\langle \cdot \rangle$ denotes the expectation, $\delta_{ik}, \delta_{jl}$ are Kronecker delta functions, $\delta_{\mathbf{x}}$ is the spatial delta function, and $\delta_t$ is the one-dimensional temporal delta function.

Note that, it's unclear how to generate a 2D version because the scalings of the thermal fluctuations in 2D and 3D are different. In three dimensions, scaling of the white-noise Gaussian random tensor is $W_{3D} \sim (L^3\tau)^{-1/2}$ where $L$ is a characteristic length and $\tau$ is a characteristic time. However, the scaling in two dimensions is $W_{2D} \sim (L^2\tau)^{-1/2}$. Here we introduce a 2D spatial scale $L_d$, and the 2D stochastic force is taken to be,

$$\mathbf{f}_{\mathrm{thm,2D}} = \sqrt{\eta k_{\mathrm{B}}T/L_{\mathrm{d}}}\nabla \cdot \mathbf{W}_{\mathrm{2D}} \tag{2.14}$$

Effectively this means that the strength of the 2D thermal fluctuations is modulated by the unknown scale $L_d$. We next develop a theory for choosing $L_d$, following [38].

## 2.2 The Parameter $L_d$ And Odijk Model

### 2.2.1 Odijk Model

To choose the spatial scale $L_d$, we consider $L_d$ as a fitting parameter to match the average equilibrium length of a fluctuating filament, which was determined analytically by Odijk [46].
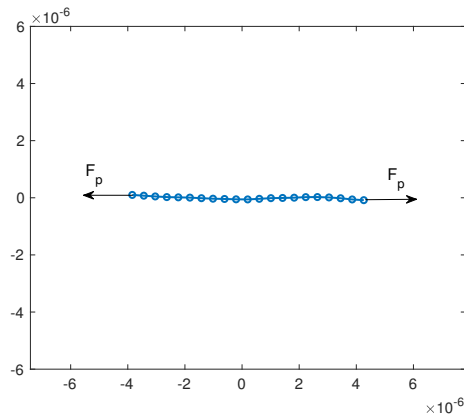


Figure 2.1: A schematic diagram of a fluctuating filament under tension.

Assuming that a filament is immersed in an initially quiescent fluid with no applied flow and constant forces $F_p$ are applied at the two ends of the filament. A schematic diagram is shown in Figure 2.1. The filament is expressed by $N_s$ (here $N_s = 20$) nodes (blue circle in Figure 2.1) that are connected by springs with spring constant $\lambda_L$. A theoretical filament length is calculated by Odijk [46] (see Eq. (2.15) below). The mean equilibrium length of the filament is [46]

$$\langle L \rangle = L_0(1 - k_B T/(2\sqrt{\kappa F_p})) + F_p N_s/\lambda_L, \tag{2.15}$$

where $L_0$ is the length of the filament in the absence of tension and fluctuations, and $F_p$ is the tension applied at the ends of the filament. Note that the equation is valid only when $L_0 k_B T/\sqrt{\kappa F_p} \ll F_p N_s/\lambda_L$. See [46] for a derivation of Eq. (2.15).

## 2.2.2   Numerical Method

To choose $L_d$, we solve a discretized version of the SIBM in a square domain $D$ with side length $L_C$ and match the average equilibrium length of a fluctuating filament from our numerical solution with the theoretical filament length calculated by Eq. (2.15).

We use a finite difference scheme to discretize the fluid equations Eq. (2.1) and (2.2). The filament is discretized using $N_s$ springs, each with elastic spring constant $\lambda_L$, to connect the discretization nodes. The velocity $\mathbf{u} = \mathbf{u}_p + \mathbf{u}^\infty$, where $\mathbf{u}_p$ is the velocity induced by the membrane and $\mathbf{u}^\infty$ is the applied extensional flow velocity. The discretized system is given

by,

$$\rho \frac{\mathbf{u}_p^{n+1} - \mathbf{u}_p^n}{\Delta t} = \eta L \mathbf{u}_p^{n+1} - \nabla \tilde{p} + \Lambda_a^D(\mathbf{F_X}) + \mathbf{f}_{\text{thm}}^{n+1}, \tag{2.16}$$

$$D \cdot \mathbf{u}_p^{n+1} = 0, \tag{2.17}$$

$$\frac{\mathbf{X}_{[i]}^{n+1} - \mathbf{X}_{[i]}^n}{\Delta t} = \Upsilon_a^D(\mathbf{u}_p)_i + \mathbf{u}_{\infty,i}^n, \tag{2.18}$$

where $\tilde{p} = p - (\nabla_{\mathbf{X}}\Lambda)k_B T$ is a modified pressure, and the discrete versions of the structure-fluid coupling operators is given by $\Lambda_a^D$ and $\Upsilon_a^D$:

$$[\Lambda_a^D(\mathbf{F_{X^n}})]_{\mathbf{m}} = \sum_i \mathbf{F}_{\mathbf{X}_{[i]}^n}(t)\delta_a(\mathbf{x_m} - \mathbf{X}_{[i]}^n)\Delta s_i, \tag{2.19}$$

$$\Upsilon_a^D(\mathbf{u})_i = \sum_{\mathbf{m}} \mathbf{u}^{n+1}(\mathbf{x_m})\delta_a(\mathbf{x_m} - \mathbf{X}_{[i]}^n)\Delta x^2, \tag{2.20}$$

where a smoothed function $\delta_a$ is used to replace the two dimensional Dirac delta function with

$$\delta_a(x,y) = \frac{1}{a^2}\varphi\left(\frac{|x|}{a}\right)\varphi\left(\frac{|y|}{a}\right), \tag{2.21}$$

where

$$\varphi(r) = \begin{cases} \frac{1}{8}(3 - 2r + \sqrt{1 + 4r - 4r^2}, & 0 \le r \le 1 \\ \frac{1}{8}(5 - 2r - \sqrt{-7 + 12r - 4r^2}, & 1 < r \le 2 \\ 0, & 2 < r. \end{cases} \tag{2.22}$$

Here we choose $a = \Delta x$. Note that the nodes are connected by springs, instead of discretization of the inextensibility equation, we use a sufficiently large spring constant $\lambda_L$ to maintain local inextensibility within 1%.

Initially, the filament is a straight line segment with length $L$, equally divided into $N_s$ sub-

segments, with each sub-segment has a length of $\Delta L = L/N$. The discrete bending energy is

$$E = \sum_{i=1}^{N_s} \frac{1}{2} \kappa H_{[i]}^2 \Delta L_{[i]} \tag{2.23}$$

where $\Delta L_{[i]}$ is the arclength associated with $i^{th}$ node, $H_{[i]} = \pi - \psi_{[i]}/\Delta L_{[i]}$ is the curvature at node i, and $\psi_{[i]}$ is the angle formed by $\mathbf{X}_{[i-1]}\mathbf{X}_{[i]}$ and $\mathbf{X}_{[i+1]}$, for $i = 2, 3, ..., N_s$. Set $H_{[1]}$ and $H_{[N_s+1]}$ to be zero. The boundary condition for the first node is $F_1 = -\kappa(H_{[2]} - H_{[1]})/\Delta L_{1,2}$.

In the filament simulations, we consider a filament with initial length $L = 8 \times 10^{-6}m$, and $N_s = 20$. So $\Delta L = L/N_s = 4 \times 10^{-7}m$. We set the bending stiffness $\kappa = 10^{-26}J$, the spring constant $\lambda_L = 10^{-4}N/m$ and $\Delta t = 10^{-6}s$. The force on the ends varies from $3 \times 10^{-11}N$ to $15 \times 10^{-11}N$. We run up to $10^5$ steps for each sample, and compute the mean length of the filament for steps $> 10^3$ as the mean equilibrium length of a fluctuating filament. We plot the nonlinear part of Eq.(2.15), $\Delta L = \langle L \rangle - L_{\text{Hook}}$, where $L_{\text{Hook}} = L_0 + F_p N_s/\lambda_L$. The analytical solution of Eq.(2.15) is shown in Figure 2.2 in dot-dashed and numerical solutions with different spatial scales $L_d$ are in symbols. In Figure 2.2, the computational domain size is $L_C = 4 \times 10^{-4}$ $m$. A good agreement is achieved between the SIBM when the spatial scale $L_d = 4 \times 10^{-4}$ $m$ (blue start) and the Odijk model (dot-dashed).

### 2.2.3 Analysis of $L_d$

We next study how $L_d$ varies if we change the size of the computational domain. If the filament is fixed, we want the numerical simulations with fitted $L_d$ to be independent of the size of the computational domain. Let $L_C$ be the side length of the computational domain.

Here we consider a filament immersed in an initially quiescent fluid (no applied flow). The filament (red segment) is placed at the center of the domains, where $\Omega_0$ (blue dot-dash) is
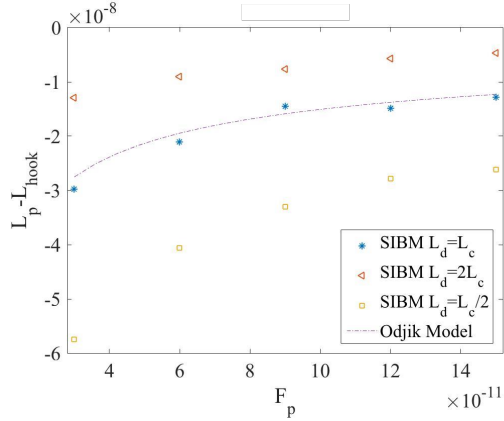
Figure 2.2: The equilibrium length of a fluctuating filament under tension. Agreement between the discrete stochastic immersed boundary method (SIBM, symbols) and the analytical solution from Eq.(2.15) (Odijk, dot-dashed) is achieved when the spatial scale $L_d = L_C = 4 \times 10^{-4}$ $m$. Here we plot the nonlinear part of Eq.(2.15), $\Delta L = \langle L \rangle - L_{\text{Hook}}$, where $L_{\text{Hook}} = L_0 + F_p N_s / \lambda_L$.

the square exactly contains the filament, i.e., the side length of $\Omega_0 = L$, where $L$ is the length of the filament, $\Omega_{\text{Small}}$ (green dot-dash) is a square that is slightly larger than $\Omega_0$ and $\Omega_{\text{Large}}$(black dot-dash) is a square that is much larger than $\Omega_0$. See Figure 2.3 as a schematic.
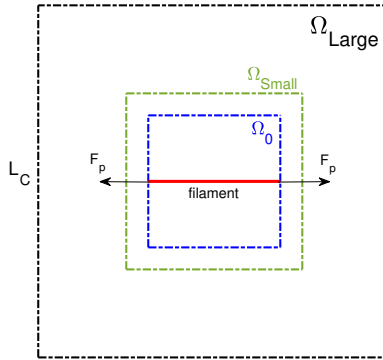


Figure 2.3: A filament(red segment) is placed at the center of domains $\Omega_0$, $\Omega_{\text{Small}}$ and $\Omega_{\text{Large}}$, constant tension $\mathbf{F}_p$ are applied at the ends of the filament.

Assume that the fluid velocity field satisfies periodic boundary conditions. Because the fluid is initially quiescent with no applied flow, the mean of the velocity of fluid $\mathbf{u}$ over the domain

16

satisfies

$$\langle \mathbf{u}_x \rangle = 0, \ \langle \mathbf{u}_y \rangle = 0, \quad \text{in } \Omega_0, \tag{2.24}$$

where $\mathbf{u}_\alpha$ is the fluid velocity alone $\alpha$-direction, $\alpha \in \{x, y\}$, $\langle \cdot \rangle$ is the mean value over the domain.
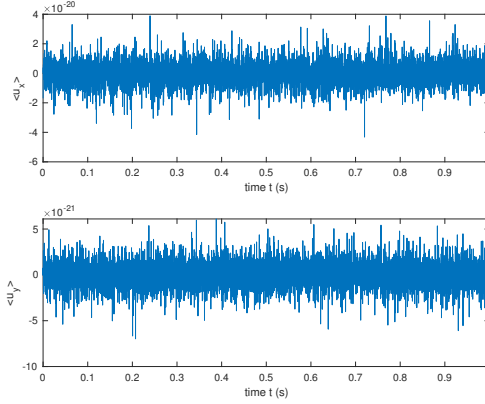


Figure 2.4: The mean value of the fluid velocity $\mathbf{u}_\alpha$ over a small domain $\Omega_{\text{Small}}$ versus time t.

We run a stochastic simulation in $\Omega$ with the side length $L_C = 1.28 \times 10^{-5} m$. (Note the length of the filament is $L_0 = 8 \times 10^{-6} m$), the spatial scale $L_d = 4 \times 10^{-4} m$. Here we collect the $\langle \mathbf{u}_x \rangle$ and $\langle \mathbf{u}_y \rangle$ at each time step, and show them in Figure 2.4. The magnitudes of $\langle \mathbf{u}_x \rangle$ and $\langle \mathbf{u}_y \rangle$ oscillate around 0 in the order of $10^{-20}$.

Then we change the size of the computational domain $L_C = 4 \times 10^{-4} m \gg L_0$, keep all the other parameters fixed and run another stochastic simulation. The results are shown in Figure 2.5. In this larger domain, The magnitudes of $\langle \mathbf{u}_x \rangle$ and $\langle \mathbf{u}_y \rangle$ are in the order of $10^{-19}$, about an order of magnitude larger than the smaller domain.

Figure 2.6 shows a positive relationship between the standard deviation over time of $\langle \mathbf{u}_x \rangle$ and the domain size $L_C$. Thus to keep thermal fluctuations stable for the same filament structure in different domains, the spatial scale $L_d$ needs to be increased when $L_C$ increases.

17
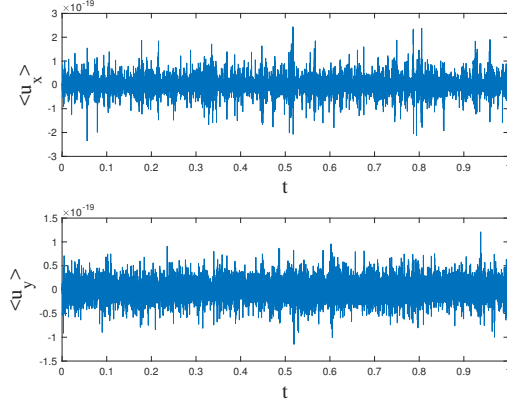
Figure 2.5: The mean value of the fluid velocity $\mathbf{u}_\alpha$ over a large domain $\Omega_{\text{Large}}$ versus time t.
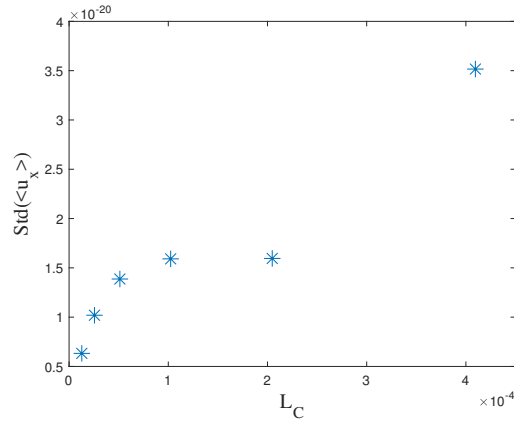


Figure 2.6: The standard deviation over time of $\langle \mathbf{u}_x \rangle$ versus the domain size $L_C$.

## Numerical Computation for $L_d$

In this section, we match the numerical results with the Odijk model and find the fitted $L_d$ for different domains. The filament is considered as a straight line segment which is equally divided into N sub-segments and fixes the filament at the center of a square domain $D$ with side length $L_C$. Here we set $N = 20, \Delta L = 4.0 \times 10^{-6}$ m. To simplify the simulation, we also set the zero modes of thermal noise to be zero because zero modes don't change the length of the filament. We double the side length $L_C$ each time and match the nonlinear simulations with the Odijk theory for each $L_C$.

In Figure 2.7, we plot the nonlinear part of Eq.(2.15), $\Delta L = \langle L \rangle - L_{Hook}$, where $L_{Hook} =$

$L_0 + F_p N_s / \lambda_L$ versus different forces $F_p$, where the analytical solution from Eq.(2.15) is shown in dot-dashed, and three realizations of the discrete stochastic immersed boundary method with different spatial scales $L_d$ are shown in symbols. The side length of the domain $L_C$ increases from $0.5 \times 10^{-4}$ (see Figure 2.7 [a]) to $8 \times 10^{-4}$ (see Figure 2.7 [e]). In each plot, the realization with blue start achieves the best agreement with Odijk model (dot-dashed).
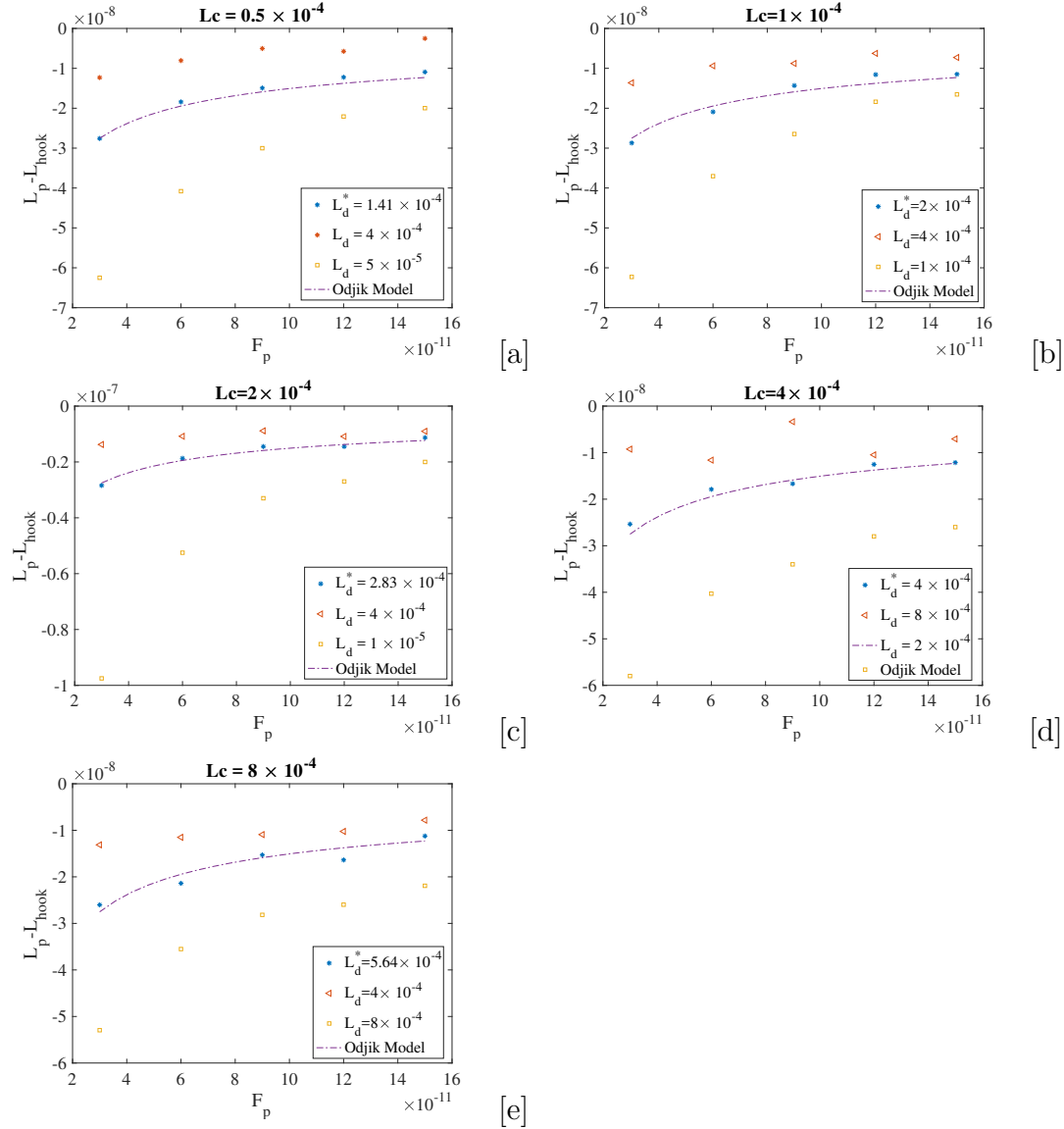


Figure 2.7: The equilibrium length of a fluctuating filament under tension in domains with different sizes.

In Figure 2.8, a linear fit is performed between $L_d^{*2}$ and $L_C$, where $L_d^*$ is the length scale that

19

matches Odijk model best for a given $L_C$. As a result,

$$L_d^* \sim \sqrt{L_C} \qquad (2.25)$$
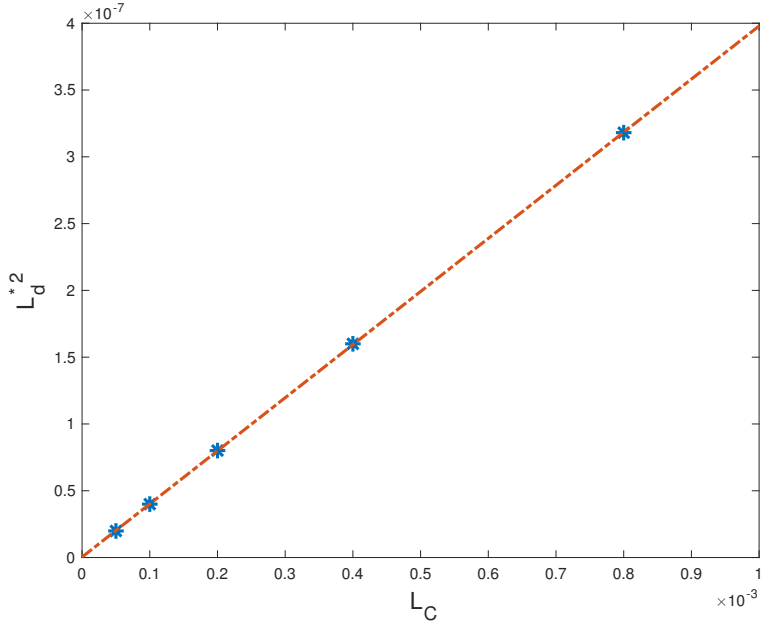


Figure 2.8: A linear fit between $L_d^{*2}$ and $L_C$.

## Justification of the scaling relationship $L_d^* \sim \sqrt{L_C}$

As we see in Figure 2.7 and 2.8, by matching the nonlinear results of the stochastic immersed boundary method with the Odijk model, we find a linear relationship between $L_d^{*2}$ and $L_C$. Here we justify this relationship by analyzing the stochastic Stokes Equations (2.1)-(2.2) via a time scale.

Let $R = \sqrt{A/\pi}$ be the effective vesicle radius (A is the total area of the vesicle), and L be the total arclength. A nondimensional shape parameter is defined as $\Delta = \frac{L}{R} - 2\pi$, which is

20

known as the excess arclength. In addition, an important time-scale

$$\tau_{thm} = \sqrt{m_0 L_C^2 / k_B T} = \sqrt{\rho L_C^5 / k_B T}, \tag{2.26}$$

gives the time duration for a fluid particle to move the distance $L_C$ when it has kinetic energy $k_B T$, where $L_C$ is the side length of the square domain D, $\rho$ is the fluid density, $\mu$ is the fluid dynamic viscosity, $\kappa$ is the bending stiffness, $k_B T$ is the thermal energy, $\sigma$ is the surface tension.

We nondimensionalize time by $t' = t/\tau_{thm}$ and space by $\mathbf{x}' = \mathbf{x}/R$, $\mathbf{X}' = \mathbf{X}/R$. Then the nondimensional velocity is $\mathbf{u}' = \mathbf{u}/\bar{U} = \left(\frac{\tau_{thm}}{a}\right)\mathbf{u}$, and a modified nondimensional pressure is $p' = \frac{\tau_{thm}}{\mu}\left(p - \Lambda\left(k_B T\right)\right)$ which incorporates the drift term. The nondimensional stochastic, non-steady Stokes equations can be written as:

$$\text{Re}\frac{\partial u'}{\partial t'} = \nabla'^2 u' - \frac{R}{a}\nabla' p' + \chi^{-1}\Lambda'(F'_{X'}) + \chi^{-\frac{1}{2}}Ku_B C^{\frac{1}{2}}\nabla' \cdot W'. \tag{2.27}$$

where $F'_{X'}$ is the nondimensional force density, $W'$ is the nondimensional white noise tensor, Reynolds number $\text{Re} = \frac{\rho R^2}{\tau_{thm}\mu}$, the nondimensional strain $\chi = \frac{R^2 L_C \mu}{\kappa \tau_{thm}}$, a bending Kubo number $Ku_B = \sqrt{k_B T/\kappa}$, which measures the strength of thermal fluctuations relative to bending forces, and a confinement number $C = \frac{R^2}{L_C L_d}$. Note that the confinement number $C$ doesn't appear in the three-dimensional formula and thus characterizes the fundamental difference between the two- and three-dimensional models of fluctuations.

Consider the coefficient of $\nabla' \cdot W'$ :

$$\chi^{-\frac{1}{2}}Ku_B C^{\frac{1}{2}} = Ku_B \cdot \left(\frac{R^2 L_C \mu}{\kappa \tau_{thm}}\right)^{-\frac{1}{2}}\left(\frac{R^2}{L_C L_d}\right)^{\frac{1}{2}} = Ku_B \cdot \left(\frac{\kappa \tau_{thm}}{\mu L_C^2 L_d}\right)^{\frac{1}{2}}, \tag{2.28}$$

21

together with $\tau_{thm} = \sqrt{\rho L_C^5 / k_B T}$,

$$\chi^{-\frac{1}{2}} K u_B C^{\frac{1}{2}} = K u_B \cdot \left( \frac{\kappa \sqrt{\rho L_C^5 / k_B T}}{\mu L_C^2 L_d} \right)^{\frac{1}{2}} = C_0 \left( \frac{L_C}{L_d^2} \right)^{\frac{1}{4}} \tag{2.29}$$

where $C_0 = K u_B \cdot \left( \frac{\kappa^2 \rho}{\mu^2 k_B T} \right)$ is a constant only depending on physical properties. Thus we have $\left( \frac{L_C}{L_d^2} \right)^{\frac{1}{4}}$ is a constant, i.e., $L_C \sim L_d^2$, which in line with the numerical result (See Eq.(2.25) and Figure 2.8).

# Chapter 3

# Wrinkling Dynamics of Fluctuating Vesicles With Impermeable Membranes

In this chapter, we apply the stochastic immersed boundary method with the suitable spatial scale $L_d$ to compute the wrinkling dynamics of a fluctuating vesicle in a periodically reversed flow. The whole point of periodically reversing the flow is to try to stabilize time-dependent wrinkles. We observe a three stage process of the dynamics of vesicles and justify it via a linear theory.

There are several necessary assumptions of the vesicle membrane in our analysis. First, we assume that the vesicle size is much larger than the membrane thickness, which enables one to treat the initial shape as an ellipse immersed in a two-dimensional fluid. Second, we assume that the membrane is inextensible. Third, we assume that the membrane is impermeable to the surrounding liquids on the time scale of the experiment.

## 3.1 Nonlinear Dynamics of a Vesicle in the Quiescent Fluid

We study the fully nonlinear dynamics of two-dimensional vesicles in a viscous fluid at finite temperature in a time-dependent extensional flow by simulating the dynamics to equilibrium of a vesicle in a quiescent fluid to validate our model. If the energy of a vesicle doesn't reach its minimum, the bending force makes the membrane move until the vesicle reaches its equilibrium state. In our simulations, we initialize the vesicles as ellipses with aspect ratio $a/b$. We utilize the stochastic immersed boundary method to solve the equation system (2.1)-(2.2) in a square domain. The detailed numerical scheme is given in Section 2.2.2, Appendix A.2, and [38].

The results of the simulations with different initial shapes are shown in Figure 3.1. The initial shape is an ellipse with major axis $a = 5 \times 10^{-5}$m, and different excess arclength $\Delta$. We set the bending rigidity is $\kappa = 10^{-19}J$ in the simulations. Dynamics of the vesicles with excess arclength $\Delta = 3.1128$ are shown in Figure 3.1[a] and the equilibrium shapes for different $\Delta$ are shown in Figure 3.1[b] (top: deterministic, bottom: stochastic). Here $\Delta$ is the excess arclength defined by

$$\Delta = \frac{L}{R} - 2\pi \tag{3.1}$$

where $L$ is the total arclength of the vesicle, $R = \sqrt{A/2\pi}$ is the effective radius, $A$ is the area of the vesicle.

It can be shown that for an excess arclength of 0, the shape minimizing the Helfrich energy is a circle (see Figure 3.1[b]). Then increasing $\Delta$ leads to a biconcave equilibrium shape, which is also a characteristic of red blood cells (Figure 3.1[b]). The deterministic equilibrium shapes are shown in the top row, which are symmetric with respect to both x-axis and y-axis, while

[a]



[b]
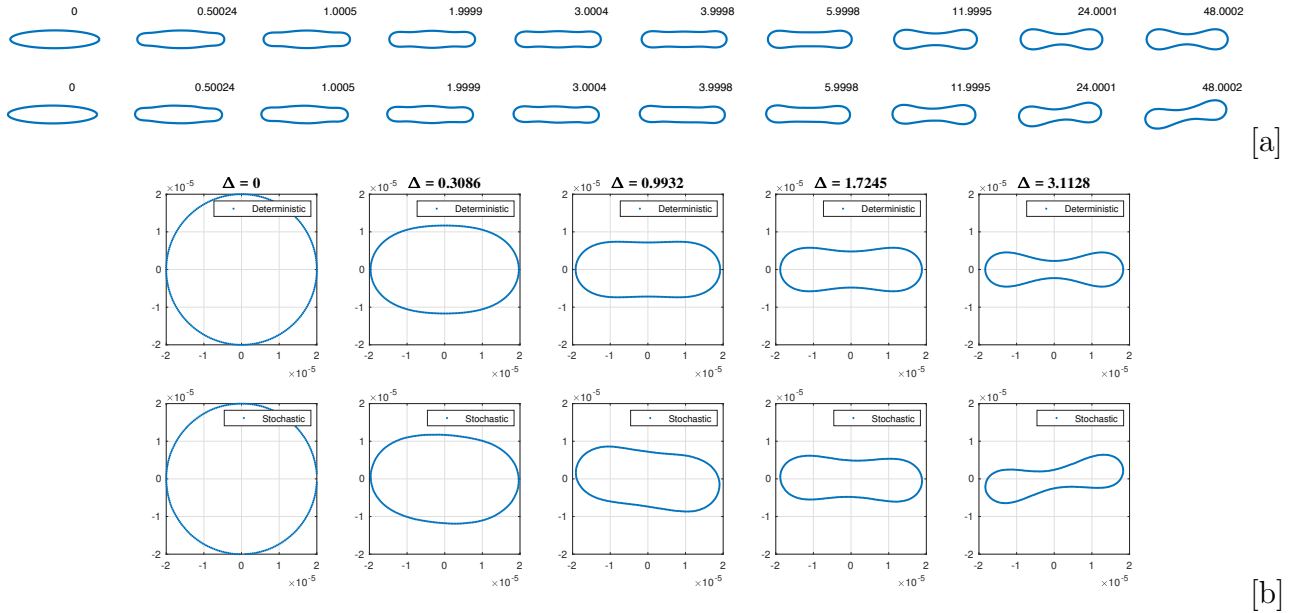
Figure 3.1: [a]Dynamics to equilibrium of a vesicle with excess arclength $\Delta = 3.1128$. [b]Equilibrium shapes for vesicles with different excess arclength $\Delta$, as labeled. Deterministic results are shown in the top row, and stochastic results are shown in the bottom row.

the equilibrium shapes in stochastic realizations are still biconcave but not aligned on x-axis anymore. The inexact symmetric shapes are due to thermal fluctuations. More dynamics of vesicles with different excess arclength are shown in Appendix A.3.

## 3.2 Wrinkling Dynamics in a Time-Dependent Extensional Flow: A Single Reversal of Flow Direction

Here we investigate the wrinkling dynamics of a vesicle that occurs at sufficiently high strain rates in steady linear flows observed in experiments[27, 35] (see Figure 3.2). In the experiments, a vesicle is immersed in a viscous fluid with an applied extensional flow. After the vesicle relaxes into an equilibrium shape, the direction of the flow is suddenly reversed. Compressive forces on the vesicle membrane activates small-scale interface perturbations, referred to wrinkles, which eventually decay away as the vesicle reaches a new equilibrium.

Here we simulate this transient instability numerically using stochastic immersed boundary method, following [38].
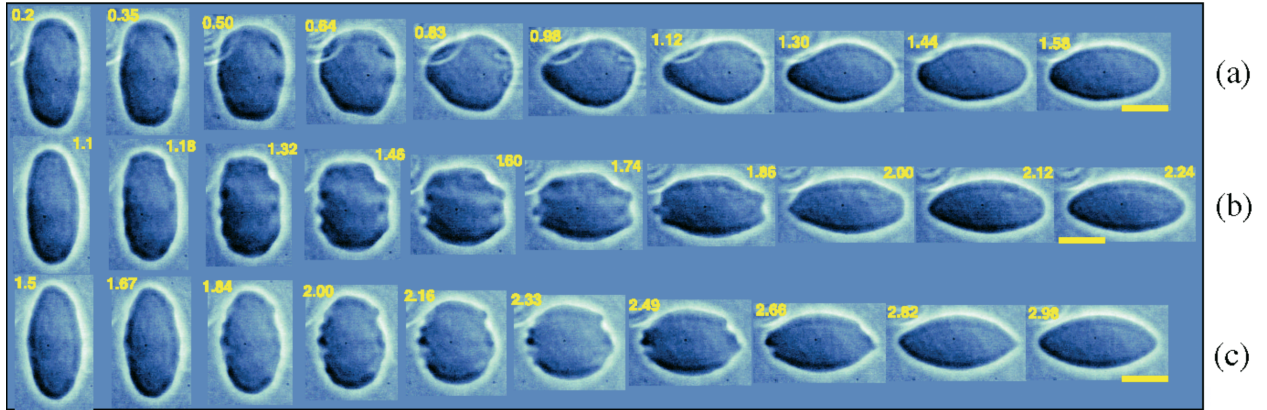


Figure 3.2: Wrinkling instability. Snapshots of vesicle dynamics in time-dependent elongation flow at [a]$\chi = 8.1$, [b]$\chi = 81$ and [c]$\chi = 323.5$, where the dimensionless strain $\chi = S\eta_{out}R^3/\kappa$.

### 3.2.1    Nonlinear Dynamics of a Quasi-Circle Vesicle

We first investigate the wrinkling dynamics of a nearly circular vesicle. The initial shape of the vesicle is an ellipse with aspect ratio $a : b = 0.8$, with small excess arclength $\Delta = \frac{L}{R} - 2\pi = 0.0587$, where the area $A = 1.0053 \times 10^{-9}m^2$, and the arclength $L = 1.1345 \times 10^{-4}m$. We set the extensional flow strength $S = 4$, the bending stiffness $\kappa = 10^{-19}J$. Because water is the primary component of the inner and outer fluids[27], we use the viscosity $\eta = 10^{-3}kg/(sm)$ and density $\rho = 10^3 kg/m^3$ of water at room temperature $T = 293K$. The results are presented in Figure 3.3.

Following the experiments, the flow is reversed at the nondimensional time $t' = 1.0$, defined as $t' = St$. Figure 3.3[a] and [b] show the vesicle morphologies for the deterministic and stochastic immersed boundary computations at the labeled time, respectively. The deterministic vesicles (see Figure 3.3[a]) are highly symmetric and contain only even modes, because the initial shape is symmetric. In contrast, the wrinkling morphologies in stochastic

26
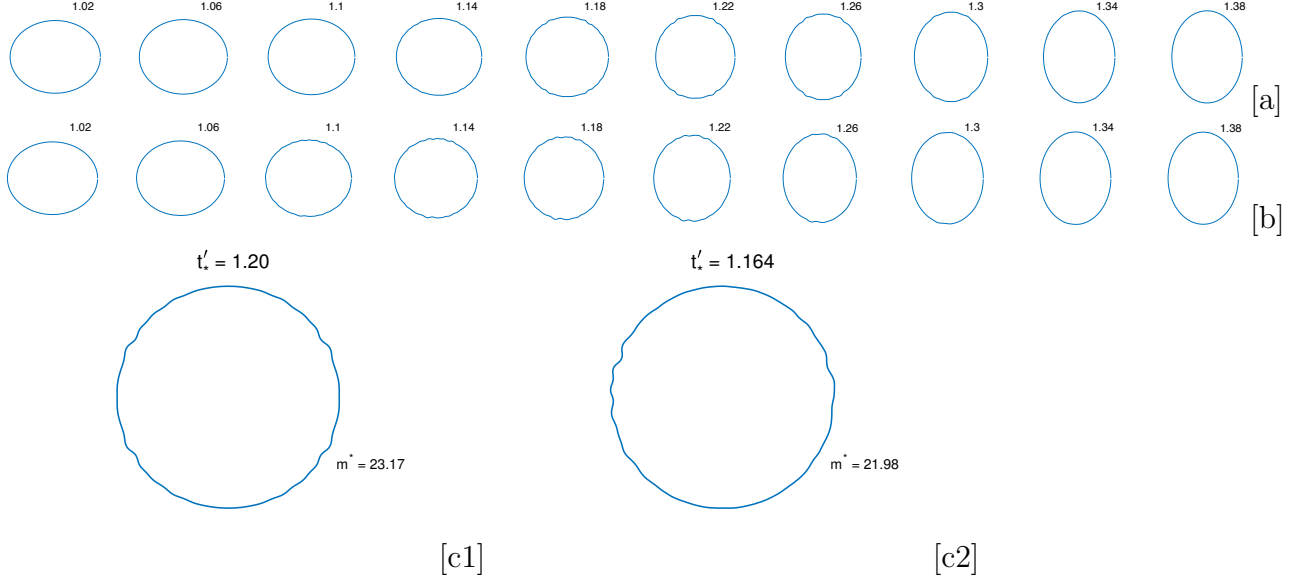
Figure 3.3: Nonlinear wrinkling dynamics of a quasi-qircular vesicle. [a] Deterministic dynamics. [b] Stochastic dynamics. [c] Vesicle morphologies at the time $t'$ with the corresponding dominant mode $m^*$ (left: deterministic; right: stochastic). The numbers in [a][b] are the nondimensional times $t'$ at which the vesicle morphologies are shown.

simulations (see Figure 3.3[b]) are asymmetrical and capture the high-order odd modes. The most dominant mode $m^*$ is defined as an average of the instantaneous Fourier spectra of the vesicle shape, computed by [52]

$$m^* = \left( \sum_{m=2}^{N_0} m |p_m|(t')^2 \right) \Big/ \left( \sum_{m=2}^{N_0} |p_m|(t')^2 \right), \tag{3.2}$$

where $\{p_m\}$ is the Fourier expansion of the membrane (see detail in Section 3.2.2), $N_0$ is the largest nontrivial mode with $|p_{N_0}| > 10^{-5}$, $t'_*$ is the (nondimensional) time at which $|p_2|$ reaches its minimum. The vesicle morphologies at the $t'$ are shown in Figure 3.3[c]. Note that the wrinkling processes are faster in stochastic case $t'_{*,sto} < t'_{*,det}$.

## 3.2.2 Quasi-circular Approximation

In this section, we present a theoretical analysis of a nearly circular vesicle, and apply the perturbation theory to analyze the wrinkling dynamics of a two-dimensional in a time-dependent flow e.g., [19, 52, 35, 39, 38].

**Model of a 2D Vesicle**

Consider a two-dimensional vesicle membrane separating two viscous fluids. We define the dimensionless viscosity ratio as

$$\lambda = \frac{\eta_1}{\eta_2}, \tag{3.3}$$

where $\eta_1$ and $\eta_2$ are the viscosities of the fluids inside and outside the vesicle, respectively. Because of conservation of the total number of the lipids and the impermeability of the membrane, the membrane is inextensible and the area of the vesicles is conserved. Actually, this is not completely true, but is nearly true and often is a good approxmation [19, 52].

The shape of a two-dimensional vesicle is characterized by the enclosed area $A$ and the total arclength $L$. The excess arclength, is a shape parameter, defined in Eq.(3.1).

By Eq.(2.8) - (2.10), the free energy of the system is

$$E = \int_{S(t)} \left[ \frac{1}{2} \kappa H^2 + \sigma \right] ds \tag{3.4}$$

where $S(t)$ be the interface, $\kappa$ is the bending rigidity of the membrane, $H$ is the local curvature, and $\sigma$ is the vesicle surface tension, which is the Lagrange multiplier corresponding

to the arclength conservation of the vesicle. The force density on the membrane is

$$\mathbf{F} = -\frac{\delta E}{\delta \mathbf{X}} = \left( \kappa H_{ss} + \frac{\kappa}{2} H^3 - H\sigma \right) \mathbf{n} + \sigma_s \mathbf{t} \tag{3.5}$$

where $\mathbf{X}(s,t)$ is the shape of the vesicle, $\mathbf{t}$ is the tangent vector and $\mathbf{n}$ is the outward normal vector.

Compared to its diameter, vesicle is relatively thin. We assume the membrane has zero thickness. Thus the velocity is continuous across the membrane

$$[\mathbf{u}]_S = (\mathbf{u}|_{S,in} - \mathbf{u}|_{S,out}) = 0, \tag{3.6}$$

and the change of the tensor equals the interfacial force density induced by the membrane configuration at $S$

$$[\mathbf{T_n}]_S = \mathbf{F}, \tag{3.7}$$

where the stress tensor $\mathbf{T} = -\hat{p}\mathbf{I} + 2\mathbf{D}$, $\hat{p}$ is the pressure and $\mathbf{D}$ is the velocity gradient.

The total velocity filed $\mathbf{u}$ consists of two parts: an applied external velocity $\mathbf{u}^\infty$ and an induced velocity due to the membrane $\mathbf{u}^{\mathrm{ind}}$.

$$\mathbf{u} = \mathbf{u}^\infty + \mathbf{u}^{\mathrm{ind}}. \tag{3.8}$$

Thus the equation of motion for the interface is

$$\partial_t \mathbf{X} = \mathbf{u}^\infty(\mathbf{X}, t) + \mathbf{u}^{ind}(\mathbf{X}, t). \tag{3.9}$$

**Linear Theory**

Let the vesicle membrane be parametrized by $\mathbf{X}(\phi, t) : r = R(1 + p)$, where $p$ is a small perturbation function and expanded in Fourier harmonics[19, 39, 38]

$$p(\phi, t) = \sum_{-\infty}^{\infty} \frac{p_m(t) \exp(im\phi)}{\sqrt{2\pi}}, \tag{3.10}$$

where $m$ is the perturbation mode and $p_m(t) \ll 1$ is the perturbation amplitude of mode $m$. In the following analysis, we neglect all higher order terms of $p_m$ and only reserve up to the quadratic order terms.

The area of a vesicle can be calculated as,

$$A = \int dA = \int_0^{2\pi} r^2 d\phi = \frac{R^2}{2} \int_0^{2\pi} \left( 1 + \sum p_m \frac{\exp(im\phi)}{\sqrt{2\pi}} \right)^2 d\phi,$$

$$= \pi R^2 \left( 1 + \frac{2p_0}{\sqrt{2\pi}} + \frac{1}{2\pi} \sum_{m \neq 0} |p_m|^2 \right) \tag{3.11}$$

Area conservation thus applies,

$$\frac{p_0}{\sqrt{2\pi}} + \frac{1}{4\pi} \sum_{m \neq 0} |p_m|^2 = 0. \tag{3.12}$$

The arclength of a vesicle can be calculated as,

$$L = \int dl = \int_0^{2\pi} \sqrt{r^2 + r_\phi^2} d\phi,$$

$$= 2\pi R \left( 1 + \frac{p_0}{\sqrt{2\pi}} + \frac{1}{4\pi} \sum_{m \neq 0} m^2 |p_m|^2 \right) + O(|p_m|^3). \tag{3.13}$$

Using Eq.(3.12), we have

$$L = 2\pi R \left( 1 + \frac{1}{4\pi} \sum_{m \neq 0} (m^2 - 1)|p_m|^2 \right) + O(|p_m|^3). \tag{3.14}$$

So the excess arclength is given by

$$\Delta = \frac{1}{4\pi} \sum_{m \neq 0} (m^2 - 1)|p_m|^2,$$ (3.15)

which is a constant.

Substituting the Fourier expansion into the curvature formula gives

$$
\begin{aligned}
H &= \frac{r^2 + 2r'^2 + rr''}{(r^2 + r'^2)^{3/2}} = \frac{1}{R}(1 - p - p'') \\
&= \frac{1}{R}\left(1 - \frac{p_0}{\sqrt{2\pi}} + \sum_{m \neq 0}(m^2 - 1)p_m \frac{\exp(im\phi)}{\sqrt{2\pi}}\right).
\end{aligned}
$$ (3.16)

Using this in Eq.(3.5), we expand the normal and tangential forces $\mathbf{F} = \{F_r, F_\phi\}$ as

$$F_r = \frac{\kappa}{R^3}\left(\sum_{m \neq 0}\left((m^2 - 1)(m^2 - \frac{3}{2} + \sigma_0)p_m + \sigma_m\right)\frac{\exp(im\phi)}{\sqrt{2\pi}}\right),$$ (3.17)

$$F_\phi = \frac{\kappa}{R^3}\sum_{m \neq 0} m\sigma_m \frac{\exp(im\phi)}{2\pi}.$$ (3.18)

In polar coordinates, the interior and exterior pressure and velocity fields in Stokes flow

[19, 57] are

$$\hat{p}^1 = \sum_{m=1}^{\infty} \xi_m^1 \, (r/R)^m \cos m\phi, \tag{3.19}$$

$$\hat{p}r = \sum_{m=1}^{\infty} \xi_m^2 \, (r/R)^{-m} \cos m\phi, \tag{3.20}$$

$$v_r^1 = \frac{R}{\eta_1} \sum_{m=1}^{\infty} \left[ \xi_m^1 \frac{m}{4(1+m)} \, (r/R)^{m+1} + \xi_m^1 \, (r/R)^{m-1} \right] \cos m\phi, \tag{3.21}$$

$$v_r^2 = \frac{R}{\eta_2} \sum_{m=1}^{\infty} \left[ -\xi_m^2 \frac{m}{4(1-m)} \, (r/R)^{-m+1} - \xi_m^2 \, (r/R)^{-m-1} \right] \cos m\phi, \tag{3.22}$$

$$v_\phi^1 = \frac{R}{\eta_1} \sum_{m=1}^{\infty} \left[ -\xi_m^1 \frac{2+m}{4(1+m)} \, (r/R)^{m+1} - \xi_m^1 \, (r/R)^{m-1} \right] \sin m\phi, \tag{3.23}$$

$$v_\phi^2 = \frac{R}{\eta_2} \sum_{m=1}^{\infty} \left[ -\xi_m^1 \frac{2-m}{4(1-m)} \, (r/R)^{-m+1} - \xi_m^2 \, (r/R)^{-m-1} \right] \sin m\phi. \tag{3.24}$$

The coefficients $\{\xi_m^1, \xi_m^2, \zeta_m^1, \zeta_m^2\}$ are determined by the boundary conditions Eq.(3.6) and (3.7). The velocity is continuous across the membrane and the change of the tensor equals the interfacial force density induced by the membrane configuration at $S$:

$$\mathbf{u}^1 - \mathbf{u}^2 = 0,$$

$$[\mathbf{T}^1 - \mathbf{T}^2] \cdot \mathbf{n} = \mathbf{F},$$

where the stress tensor $\mathbf{T} = -\hat{p}\mathbf{I} + 2\mathbf{D}$, $\hat{p}$ is the pressure and the symmetric part of the velocity gradient $\mathbf{D}$ is

$$\mathbf{D} = \begin{bmatrix} \frac{\partial v_r^i}{\partial r} & \frac{1}{2}\left( r\frac{\partial}{\partial r}\left(\frac{v_\phi^i}{r}\right) + \frac{1}{r}\frac{\partial v_r^i}{\partial \phi} \right) \\ \frac{1}{2}\left( r\frac{\partial}{\partial r}\left(\frac{v_\phi^i}{r}\right) + \frac{1}{r}\frac{\partial v_r^i}{\partial \phi} \right) & \frac{1}{r}\frac{\partial v_\phi^i}{\partial \phi} + \frac{v_r^i}{r} \end{bmatrix}, \quad i = 1, 2. \tag{3.25}$$

Solving above equations with boundary conditions Eq.(3.6) and Eq.(3.7), we find the induced

velocity at the vesicle membrane along the normal direction is

$$v_m^{ind} = -\frac{\kappa}{R^3 \eta_2} \frac{|m|(m^2 - \frac{3}{2} + \sigma_0)}{2(1+\lambda)} p_m, \tag{3.26}$$

where $v_m^{ind}$ is the $m$-th Fourier mode of the velocity induced velocity $\mathbf{u}^{ind}$.

By plugging in the expansion into Eq.(3.9), we have

$$\tau \dot{p}_m = S(t)(\delta_{m,2} + \delta_{m,-2}) - (A_m \sigma_0 + \Gamma_m) p_m, \tag{3.27}$$

where $S(t) = S\text{sign(t)}$ indicates that the direction of the flow is reversed at $t = 0$, and $S$ is the strength of the applied elongational flow, $\tau = \frac{R^3 \eta_2}{\kappa}$ is a characteristic time scale associated with the bending properties of the membrane, $\delta_{i,j}$ is the Kronecker delta, $A_m = \frac{|m|}{2(1+\lambda)}$, $\Gamma_m = \frac{|m|(m^2 - \frac{3}{2})}{2(1+\lambda)}$.

Taking the time derivation of Eq.(3.15) and combining the result with Eq.(3.27), we obtain

$$\sigma = \frac{6S(t)\text{Re}(p_2) - \bar{\Gamma}}{\bar{A}}, \tag{3.28}$$

where $\bar{\Gamma} = \sum_{m \neq 0} (m^2 - 1)\Gamma_m |p_m|^2$, and $\bar{A} = \sum_{m \neq 0} (m^2 - 1)A_m |p_m|^2$.

**Stochastic Noise**

Let $\xi_m(t)$ denote for the $m$-th Fourier mode of the stochastic force density on the membrane. Then the equation of motion Eq.(3.27) becomes a system of stochastic differential equations

$$\dot{p}_m = S(t)(\delta_{m,2} + \delta_{m,-2}) - \frac{\kappa}{\eta_2 R^3} \beta_m E_m p_m + \xi_m(t), \quad \text{for } m \neq 0 \tag{3.29}$$

where the elastic coefficient $E_m = (m^2 - 1)(m^2 - \frac{3}{2} + \sigma)$ and the mobility coefficient $\beta_m = \frac{|m|}{2(m^2-1)(1+\lambda)}$.

We assume the stochastic fluctuation $\xi_m(t)$ is a scaled complex valued white noise, i.e.

$$\xi_{\pm m}(t) = \frac{1}{\sqrt{2}} \Xi_m \left( \frac{dB_{m,1}(t)}{dt} \pm i \frac{dB_{m,2}(t)}{dt} \right), \quad \text{for } m = 1, 2, 3, ... \tag{3.30}$$

where $B_{m,1}(t), B_{m,2}(t)$ are independent standard Brownian motions, and $\Xi_m = \sqrt{\frac{2\beta_m k_b T}{\eta_2 R^2}}$ are coefficients depending on $m$.

Taking the time derivative of Equation Eq. (3.15), and using Eq. (3.29) gives

$$\sigma = \frac{6S(t)Re(p_2) - \bar{\Gamma} + \bar{\xi}}{\bar{A}} \tag{3.31}$$

where

$$\bar{\xi} = \sum_{m \neq 0} (m^2 - 1) \frac{p_m^* \Xi_m}{\sqrt{2}} \frac{dB_m(t)}{dt}. \tag{3.32}$$

**Numerical Results**

First, we test the performance of our algorithm. We set the initial shape of the vesicle to be an ellipse with aspect ratio $a : b = 1 : 0.8$, the applied flow rate $S = 4$ and the bending stiffness $\kappa = 10^{-19} J$. We run the algorithms with time step $\Delta t = 10^{-5} s$, $\Delta t/2$, $\Delta t/4$ and $\Delta t/8$ and check the convergence of time using the change in excess arclength $\Delta$ according to

$$r_C = \frac{\log\left(|Err(\Delta t)|/|Err(\Delta t/2)|\right)}{\log 2} \tag{3.33}$$

where the error defined as $Err(\Delta t) = (\max(\Delta_{\Delta t}) - \min(\Delta_{\Delta t}))/\max(\Delta_{\Delta t})$. The results in

Table 3.1 show that our algorithm converges.

| Time Step | Deterministic Euler | | Deterministic RK2 | | Stochastic RK2 | |
|---|---|---|---|---|---|---|
| | $Err$ | $r_C$ | Err | $r_C$ | Err | $r_C$ |
| h | 6.145e-4 | $\sim$ | 1.532e-8 | $\sim$ | 4.249e-7 | $\sim$ |
| h/2 | 3.073e-4 | 0.9999 | 3.83e-9 | 1.9999 | 1.0561e-07 | 2.0058 |
| h/4 | 1.537e-4 | 0.9998 | 9.6e-10 | 2.000 | 2.6318e-08 | 2.0032 |
| h/8 | 7.68e-5 | 0.9996 | 2.4e-10 | 1.9999 | 6.5677e-09 | 2.0018 |

Table 3.1: Test of Convergence in Time.

Now we solve the SDEs (3.29) for $p_m$ numerically and compare the solution with $p_m$ computed from SIBM. Here we set the parameters to be the same as in the nonlinear simulations. The surface tensions are shown in Figure 3.4[a], which indicate three stages of the wrinkling process: initiation, development, and decay. In the initiation stage, because of the negative surface tension, the interface perturbations start to form. In the development stage, the surface tension is increasing but still negative. In the decay stage, the surface tension is non-negative and wrinkles are smoothed out. The deterministic result is in blue, and the stochastic result is in red. They behave similarly but with variability from thermal fluctuations in the stochastic case.

Figure 3.4[b] presents the evolution of the second mode $p_2$ and the most dominant mode $m^* = 22$ during the wrinkling dynamics (left: linear, right: nonlinear). Basically linear theory captures the decay of $|p_2|$ (blue line) and at the same time the growth of $|p_{22}|$ (red line), while because of nonlinear interactions, the times that $|p_2|$ (and $|p_{22}|$) reach their minimum (maximum) in the linear and nonlinear simulations are not exactly the same.
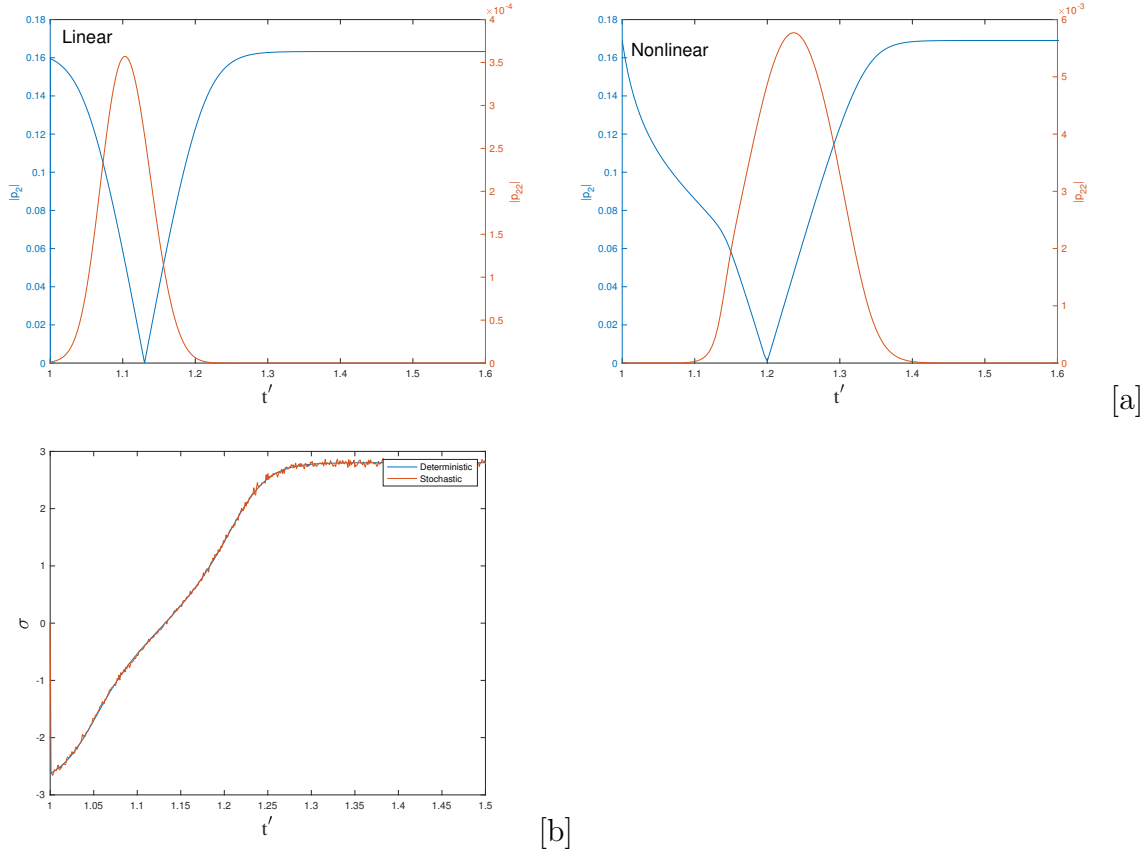
Figure 3.4: Dynamics of a quasi-circular vesicle subjected to an one reversal of an applied extensional flow at time $t' = 1$. [a] Magnitudes of $|p_2|$ and $|p_{22}|$ in linear (left) and nonlinear (right) simulations. [b] Surface tension computed from linear theory.

### 3.2.3 Nonlinear Dynamics of an Elongated Vesicle

Now we investigate the transient wrinkling numerically and compare the results with those from the experiments. In the experiments, a giant vesicle is released in an extensional flow. After it relaxes into an equilibrium shape, the direction of the flow is suddenly reversed. A transient wrinkling dynamics is observed on the membrane. The wrinkles are smoothed out when the vesicle reaches another equilibrium state. We match the long-axis of an elliptical fit to the 2D cross-section of the experimental vesicle. The initial vesicle is an ellipse with major and minor axes $a = 2 \times 10^{-5}m$, $b = 0.8 \times 10^{-5}m$, i.e. aspect ratio $a : b = 1 : 0.4$ and excess arclength $\Delta = 0.994$. As in the experiments, the flow is reversed at the nondimensional time $t' = 1.0$.
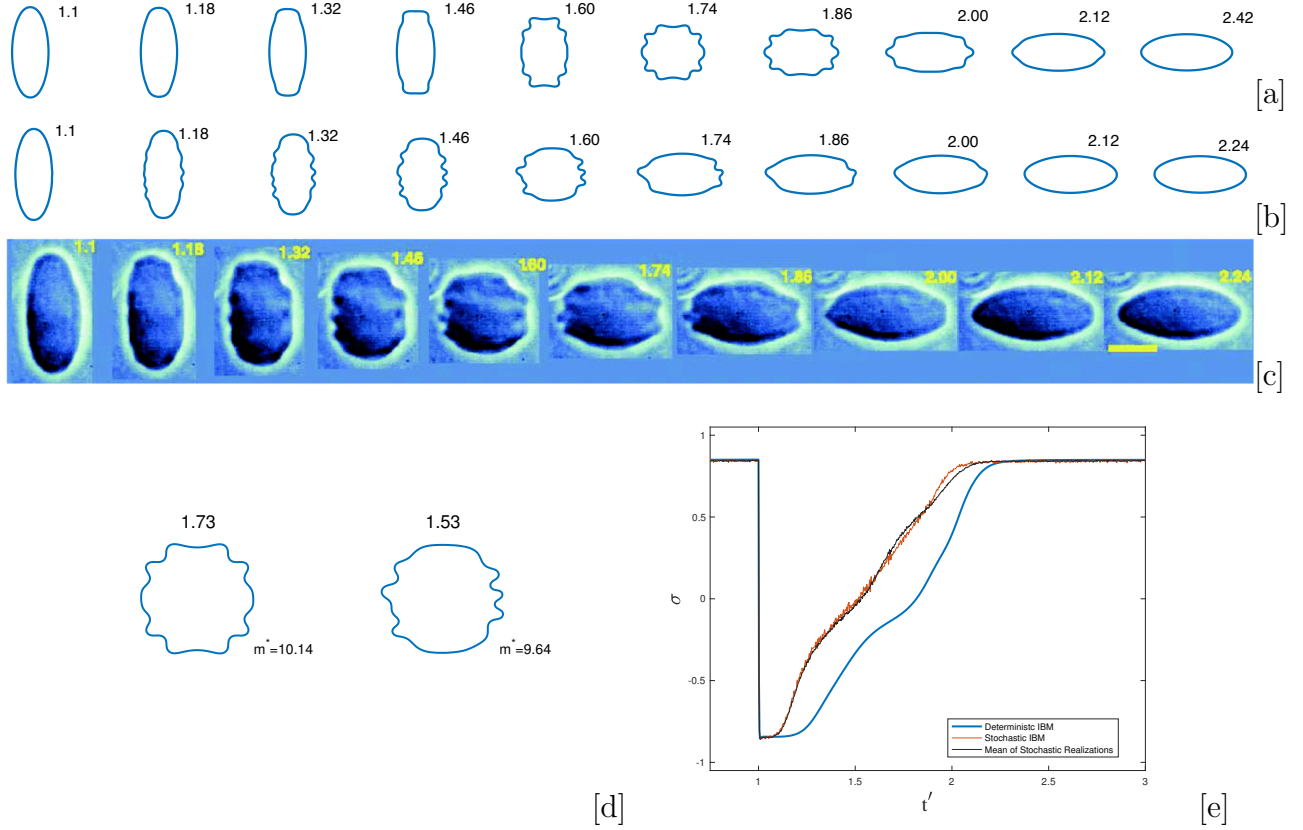
Figure 3.5: Wrinkling dynamics of an elongated vesicle. [a] Deterministic dynamics. [b] Stochastic dynamics. [c] Experimental results. [d] Surface tension for the deterministic (blue), stochastic (red) as a function of time. [e] Vesicle morphologies at the time $t'$ (as labeled) and the corresponding dominant mode $m^*$ (left: deterministic, right: stochastic).

Figures 3.5[a] and [b] show the vesicle morphologies for the deterministic and stochastic immersed boundary computations, respectively. In the deterministic wrinkling process, the shape of the vesicle is symmetric with respect to both the x-axis and y-axis (even mode), while in the fluctuating wrinkling process, the shape of the vesicle is no longer symmetric, and high-order odd modes are excited. Figure 3.5[c] shows the corresponding experimental results [27]. As the flow reversed, the surface tension suddenly becomes negative and generates the wrinkling. In Figure 3.5[e], there are three stages in the wrinkling dynamics, which was seen earlier in the perturbation theory (see Figure 3.4[a]). The first stage occurs immediately after the flow is suddenly reversed and the surface tension becomes negative as the wrinkles start to form. In the second stage, the surface tension remains negative and slowly increases while

the amplitudes of wrinkles grow. In the third stage, the surface tension is non-negative and all wrinkles are smoothed out as the vesicle aligns with the new extensional flow direction. The dominant mode $m^*$ (defined in Eq.(3.2)) and corresponding vesicle morphologies are shown in Figure 3.5[d]. In the deterministic dynamics, $t'_* \approx 1.73$, the dominant mode is $m^* \approx 10.14$. In the stochastic case, $t'_* \approx 1.53$ is smaller and $m^* \approx 9.64$.

## 3.3 Wrinkling Dynamics in a Time-Dependent Extensional Flow: Periodical Reversals of Flow Direction

### 3.3.1 Nonlinear Wrinkling Dynamics of a Quasi-Circle Vesicle

From previous analyses[57, 38, 39] and those shown in the previous section, we know that the wrinkling of the vesicle is caused by the suddenly changed negative surface tension and is transient. When the vesicle aligns with the new extensional flow direction, the wrinkles are smoothed out. We next ask whether we can prevent the decay of the wrinkles on the vesicle membrane by periodically reversing the extensional flow.

Firstly, we set the rule to reverse the direction of the flow. Because at the stationary state, most of the excess arclength is stored in the second Fourier mode $p_2$ [57], to excite wrinkles, we want $p_2$ to be small. Therefore, we use $|p_2|$ to set up a threshold to reverse the flow: When $|p_2|$ is greater than some constant $C_h$, the direction of the flow is reversed.

Secondly, we study the wrinkling dynamics of a nearly circular vesicle. The initial shape of the vesicle is an ellipse with aspect ratio $a : b = 0.8$ and the excess arclength $\Delta = 0.0587$. In the simulations, we set the extensional flow strength $S = 4$, the bending stiffness $\kappa = 10^{-19}J$ and the threshold $C_h = 100$.

We begin by allowing the vesicle to reach its equilibrium configuration before we reverse the flow field. Once this occurs, we reverse the flow direction. The surface tension becomes negative and $|p_2|$ begins to decline. After a short time, the negative surface tension activates the wrinkles. When $|p_2|$ reaches its minimum and starts to increase, the wrinkles begin to be smoothed out. We keep track of $|p_2|$ and reverse the direction of the flow as $|p_2|$ reaches the threshold $C_h$. We then repeat reversing the flow and investigate the entirety dynamics of the vesicles. As expected, the vesicles undergo a series of complex morphological transitions where the complexity of the shapes depend on the strength of the applied flow. We investigate both deterministic and stochastic dynamics. A three-stage process of the vesicle dynamics is observed in our numerical simulations.

**Deterministic Dynamics**

In the first few time units (seconds), because of the sudden change of flow direction, the surface tension becomes negative immediately and excites high-order Fourier modes. Once $|p_2|$ meets its minimum and starts to increase, the high-order modes start to decrease. Before the wrinkles disappear, $|p_2|$ reaches the threshold $C_h$ and the flow is reversed again, which re-generates the wrinkles. Figure 3.6 shows the vesicle morphologies of the first stage of the dynamics using the deterministic model. Figures 3.6[b] and [c] show the evolution of low Fourier modes and the surface tension $\sigma$ versus time, respectively. Here $\sigma$ is the average value of the local surface tension along with the vesicle. Induced by flow reversals, the surface tension and Fourier modes are oscillating. Note that only even modes are nontrivial in the deterministic case. The magnitude of the $4^{\text{th}}$ mode $|p_4|$ is small in this stage and starts to grow at the end of the stage. The corresponding morphologies of the vesicle are shown in Figure 3.6[a](red stars: shapes in the top row; green triangles: shapes in the bottom row). The morphologies at the same column are chosen at two consecutive reverses.

During the next stage of the dynamics, shown in Figure 3.7, the $4^{\text{th}}$ mode further increases

Figure 3.6: Deterministic wrinkling dynamics of a quasi-circular vesicle. Stage 1: [a]Shapes of the vesicle at the labeled time. [b] Fourier spectra. [c] Surface tension.

and eventually saturates in a dominant 4-fold symmetric vesicle shape, which oscillates with the long axis changing from being horizontal to vertically aligned depending on the direction of the flow. Later, the $4^{\text{th}}$ Fourier mode increases and becomes dominant. The values of the peaks and dips of $|p_4|$ keep nearly stable. The dynamics of the vesicle at selected times at which the direction of the flow is reversed are shown in Figure 3.7[a]. We compare the morphologies of the vesicle at the beginning ($t \approx 13$, blue) and the end ($t \approx 29$, red) in this stage (see Figure 3.7[d]). These shapes are nearly overlapped, which means the vesicle shape is controlled quite well during the stage of the dynamics, which lasts about 20s.

During the next stage of the dynamics, shown in Figure 3.8, the magnitude of 2-mode $|p_2|$ starts to increase. As $p_2$ starts to increase, the dynamics transitions to the third stage (see Figure 3.8). The diagonal of the vesicle at $t \approx 73$ is slightly rotated compared with it at $t \approx 34$. This is induced by the growth of $p_2$ (Figure 3.8[d]). As this process continues, the other modes decrease and the $p_2$ dominates the shape of the vesicle (Figure 3.9). The final shape is ellipse-like with an inclination angle around $45°$.

Figure 3.7: Deterministic wrinkling dynamics of a quasi-circular vesicle. Stage 2: [a]Shapes of the vesicle at the labeled time, [b]Fourier spectra. [c]Surface tension. [d] Comparison of shapes.

We summarize the deterministic dynamics in Figure 3.10, which shows the evolution of the low Fourier modes $p_2, p_3, p_4$ and the surface tension $\sigma$ versus time, respectively. The behavior of the Fourier modes $|p_m|$ indicates this three-stage process. In the first stage, high-order wrinkles are activated by the changed surface tension. In the second stage, the vesicle is dominated by $p_4$. In the last stage, $p_2$ increases and the wrinkles are smoothed out.

Figure 3.8: Deterministic wrinkling dynamics of a quasi-circular vesicle. Stage 3: [a] Shapes of the vesicle at the labeled time. [b] Fourier spectra. [c] Surface tension. [d] Comparison of shapes.

## A Stochastic Dynamics

Next, we incorporate thermal fluctuations and observe an analogous 3 stage dynamical process (Figures 3.11 - 3.13). In contrast to the deterministic simulation, thermal fluctuations create both odd and even modes, which break the vesicle symmetry.

During the first few time units, high-odd modes are excited (see Figure 3.11[b]), but then decay away and the vesicle shape becomes more dominated by the low modes. For example, at $t = 1.2059s$, the dominant mode is $m^* = 7.7953$, and it decreases to $m^* = 2.9284$ at $t = 40.2050s$.

As seen in Figure 3.12[a] and quantified in 3.12[b], the high-order wrinkling disappears and the shapes of the vesicle become dominated by the third mode (see Figure 3.12). Although
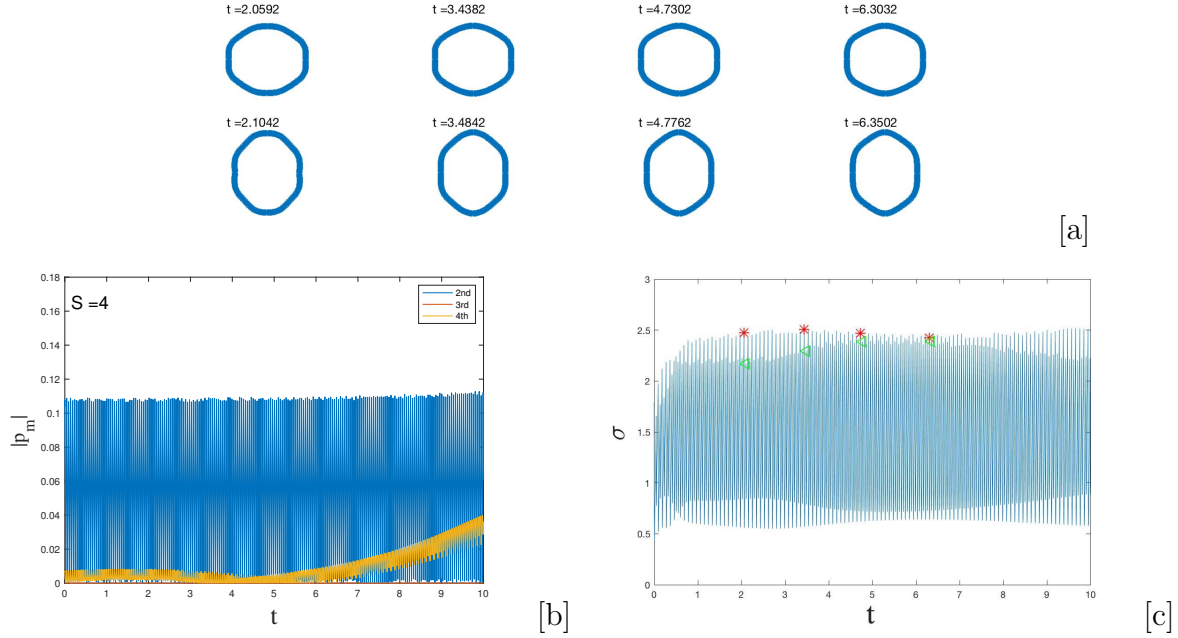
Figure 3.9: Deterministic wrinkling dynamics of a quasi-circular vesicle. Stage 3 (continue): [a] Shapes of the vesicle at the labeled time. [b] Fourier spectra. [c] Surface tension.

the 4th mode also grows at early times, this mode decays after reaching a maximum at $t = 5$ s. This is a contrast to the deterministic case where the $4^{\text{th}}$ mode dominates at the early times.

During the next stage of the evolution, the shapes of the vesicle become relatively stable over about 45s (from $t = 40$ s to $t = 86$ s). Here we compare the shapes at $t \approx 41$ and $t \approx 86$ in Figure 3.12[d]. The shapes are almost overlaid and the corresponding Fourier spectra $p_m$ are nearly equal for $m$ with $|p_m| > 5 \times 10^{-4}$.

In the third stage of the dynamics, all the other modes start to decay and $p_2$ becomes dominant again (Figure 3.13). In Figure 3.13[d] left, the vesicle shape at $t = 117$ is slightly rotated comparing with the shape at $t = 86$. The final vesicle is elliptical and oriented at approximate 45°.
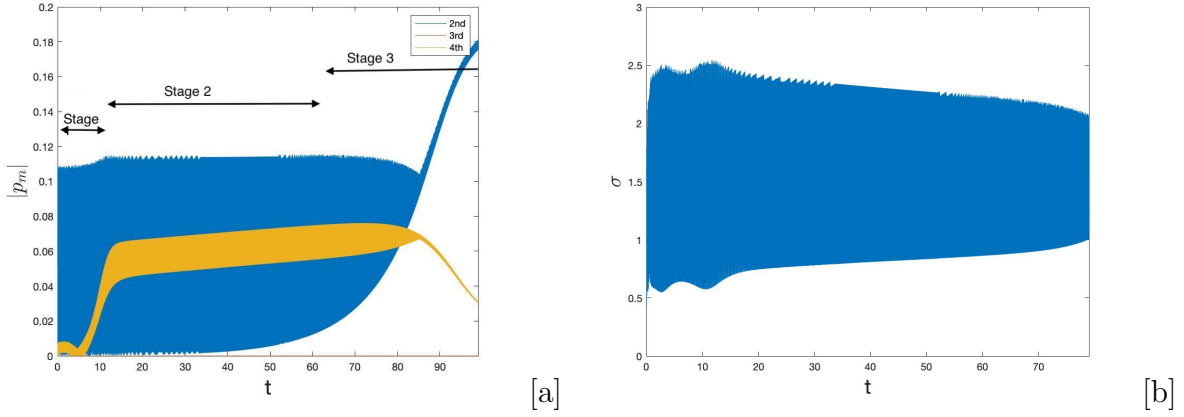
Figure 3.10: Deterministic wrinkling dynamics of a quasi-circular vesicle. [a]Fourier spectra. [b] Surface tension.

The evolution of the low Fourier modes and surface tension versus time are summarized in Figure 3.14. As in the deterministic case, shown in Figure 3.10, there are 3 stages to the vesicle kinetics. However, in the stochastic one, the $3^{rd}$ mode dominates the stage of the evolution and this stage lasts longer than the $2^{nd}$ stage in the deterministic case, where the $4^{th}$ mode dominates. Comparing with Figure 3.10, $p_3$ acts an important role during the entire process. It dominates the shapes of the vesicle in the second stage.

## 3.3.2 Linear Theory

To understand the dynamical process and mode selection mechanisms, we simulate the linear (perturbation) system and compare the results with the fully nonlinear simulations. We continue using the setting in Section 3.2.2 and Equation system (3.27). The amplitudes of the Fourier modes $|p_2|, |p_3|, |p_4|$ are shown in Figure 3.15 (Left: linear, Right: nonlinear). The evolution of these modes indicates the three stages of the deterministic wrinkling dynamics. In the first stage, the $4^{th}$ mode increases dramatically. In the second stage, the $4^{th}$ mode is oscillating in a stable range. And in the third stage, the $2^{nd}$ mode increases and all the other modes decay.
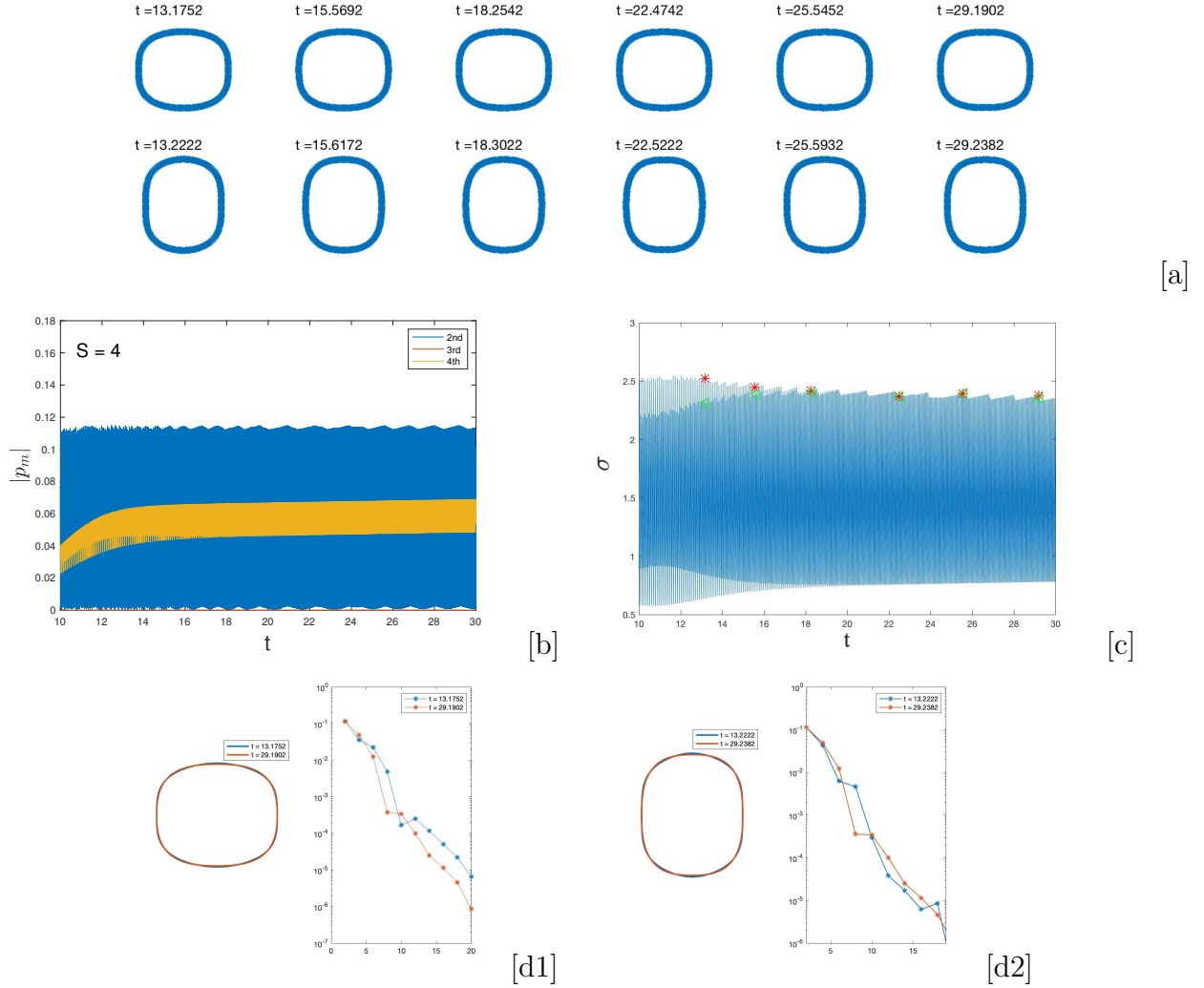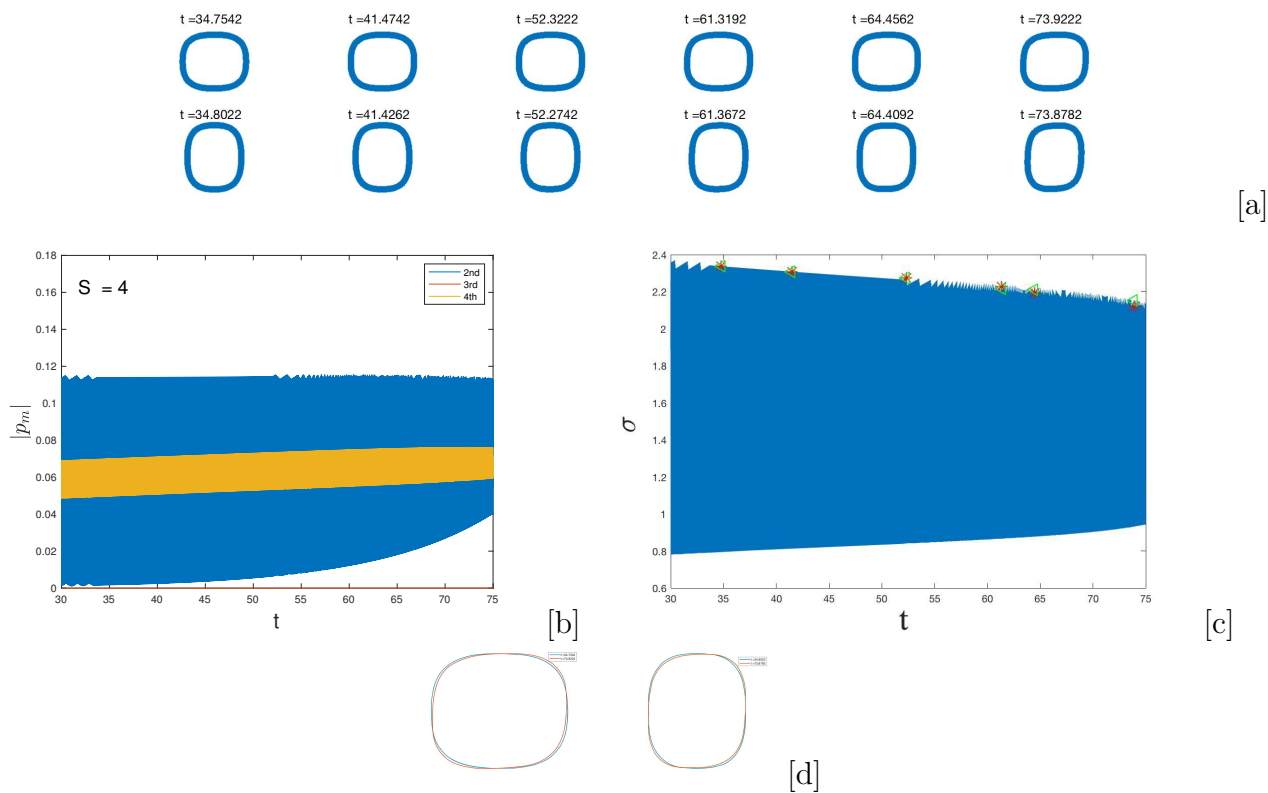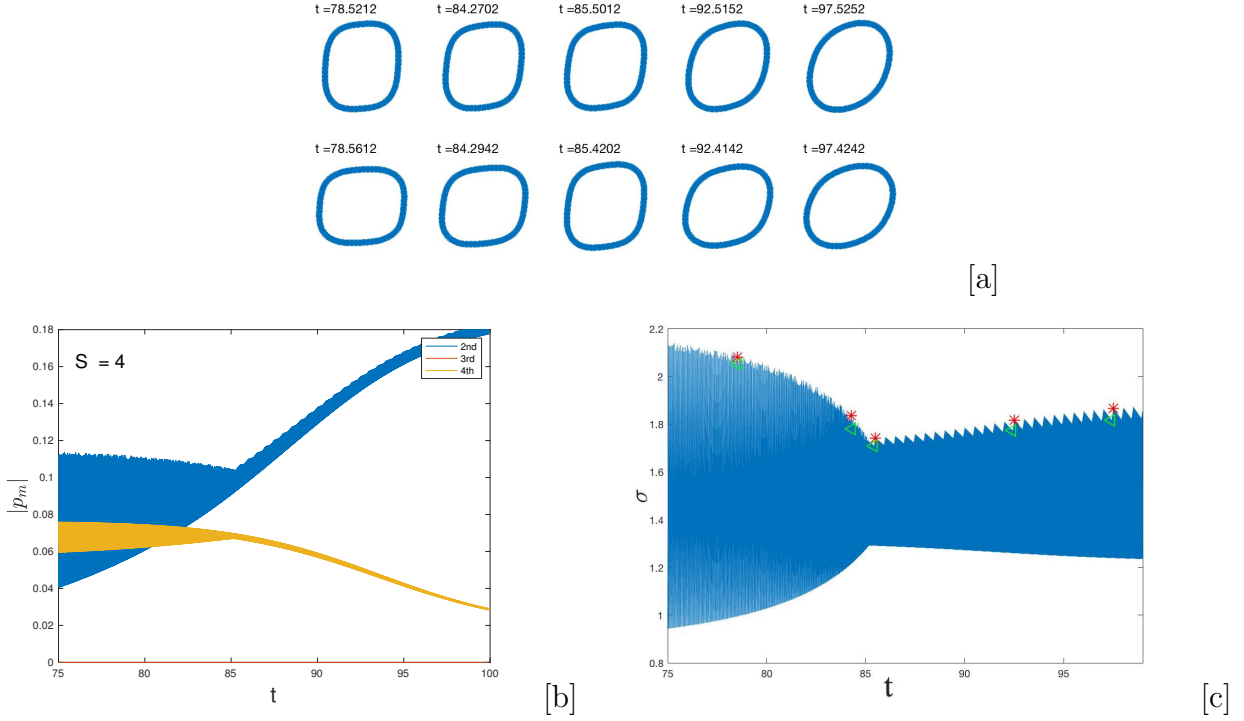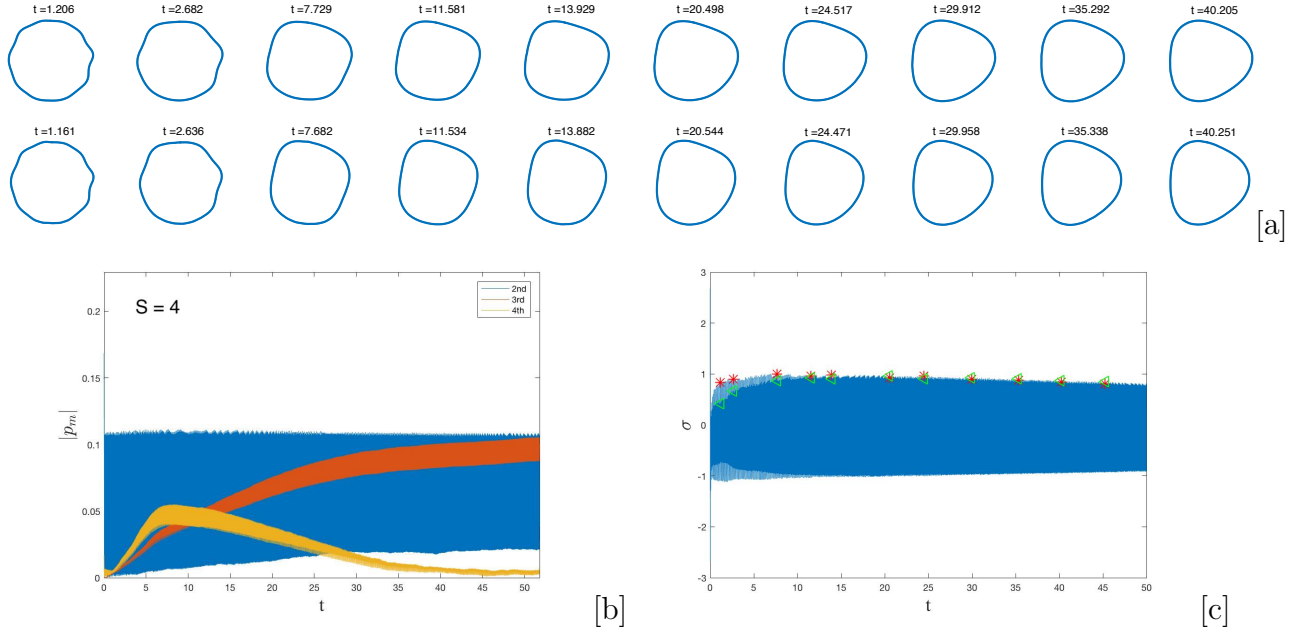
Figure 3.11: Stochastic wrinkling dynamics of a quasi-circular vesicle. Stage 1: [a] Shapes of the vesicle at the labeled time.[b]Fourier spectra. [c]Surface tension.

### 3.3.3 Nonlinear Dynamics of An Elongated Vesicle

**Deterministic Dynamics**

Next, we study the nonlinear dynamics of an elongated vesicle in a periodically reversed applied extensional flow. The initial shape of the vesicle is an ellipse with aspect ratio $a : b = 1 : 0.4$, i.e. the shape parameter $\Delta = 0.994$. In the simulations, we set the extensional flow strength $S = 4$, the bending stiffness $\kappa = 10^{-19}J$ and threshold $C_h = 100$. Similar to the quasi-circular vesicles, we observe a three-stage dynamical process of the vesicle.

Figures 3.16 - 3.18 illustrate the dynamics using the deterministic model. In the first stage, high-order wrinkles (small scale) are excited by the negative surface tension induced by the flow reversal (see Figure 3.16). Compare with Figure 3.6[a], the morphologies of the vesicle in Figure 3.16[a] are corresponding to the time labeled in Figure 3.16[b] (top row: red stars, bottom row: green triangle).

45

Because $\Delta$ is larger, the wrinkles are more obvious than those on quasi-circular vesicles. Similar to the quasi-circular case, only even modes are present in the deterministic dynamics. After a few flow reversals, high-order wrinkles decay and $p_4$ increases quickly and stabilizes, as seen in Figure 3.17, which shows that the vesicle oscillates between 2 four-fold symmetric shapes as the flow periodically reverses. In the third stage of the dynamics, the magnitude of the 2$^{\text{nd}}$ mode $|p_2|$ increases while other modes decay. This is shown in Figure 3.18 and the vesicle tends to an ellipse-like shape oriented at 45°.

The full dynamics of low Fourier modes $|p_m|$, with $m \leq 4$ and the evolution of $\sigma$ versus time are summarized in Figure 3.19.

**A Stochastic Realization**

We now consider the influence of thermal fluctuations. A stochastic realization is shown in Figures 3.20 - 3.22. The wrinkles are activated in the first few flow reversals (see the morphologies in Figure 3.20[a]). As $p_3$ and $p_4$ rise, the shapes turn to be controlled by the $4^{\text{th}}$ mode which are shown in Figure 3.20[a] and [b] at $t > 3$. Next, $p_4$ begins to decline, $p_3$ grows and the vesicle acquires a roughly 3-fold symmetric shape, as shown in Figure 3.21. At the end of this stage, the $3^{\text{rd}}$ mode dominates the shapes of the vesicle. We can recognize the reduction of the 4th mode and the addition of the $3^{\text{rd}}$ mode in Figure 3.20[a]. At $t = 5.061s$, we notice four clear angles while the left top angle smoothes out at $t = 8.9325s$. During the last stage of the dynamics, The magnitude of the $2^{\text{nd}}$ mode $|p_2|$ increases rapidly and leads to a biconcave shape. The dynamics of the vesicle morphologies, mode magnitudes, and surface tension are shown in Figure 3.22. The vesicle morphologies on Fourier spectra at $t \approx 42s$ and $t \approx 47s$ are compared in Figure 3.22[d]. Because the shapes are nearly overlaid and the Fourier spectra are quite comparable, we believe that these are the final stable shapes.

Here the evolution of magnitudes of the low modes $|p_m|$ and surface tension for the entire process are presented in Figure 3.23. Compared to the deterministic case (and the quasi-steady case), the $2^{\text{nd}}$ stage is much shorter.

We also plot the evolution of $m^*$ versus time in Figure 3.24. The morphologies of the vesicle on the plot correspond to the labeled points (red squares). We observe a rapid decay in the first 3 s, the dominate mode $m^*$ drops from 5.5 ($t = 0.3850$ s) to 3.6 ($t = 3.3835$ s). Then the shapes keep relatively stable for a few seconds around $m^* \approx 3.5$. Then $m^*$ decays to 2.1 and stabilizes as the vesicle reaches a final biconcave shape, oriented at $-45°$.

## Inclination Angle

From the above sections, we find out that in the last stage of the dynamics, $p_2$ dominates the shape of the vesicle and the orientation the vesicle changes. The shape and orientation of the vesicles can be quantified by a shape parameter and inclination angle based on the gyration tensor $G$ of the vesicle membrane[41]:

$$G = \frac{1}{N} \begin{bmatrix} \sum_{i=1}^{N} (x_i - x_{cm})^2 & \sum_{i=1}^{N} (x_i - x_{cm})(y_i - y_{cm}) \\ \sum_{i=1}^{N} (x_i - x_{cm})(y_i - y_{cm}) & \sum_{i=1}^{N} (y_i - y_{cm})^2. \end{bmatrix} \tag{3.34}$$

Let $\Lambda_{max}$ and $\Lambda_{min}$ be the two eigenvalues of $G$, and $\hat{\mathbf{e}}_{max}$ be $\hat{\mathbf{e}}_{min}$ are the corresponding eigenvectors. The inclination angle is defined by

$$\theta = \angle(\hat{x}, \hat{\mathbf{e}}_{max}) \tag{3.35}$$

where $\hat{x}$ is the unit vector in the positive $x$-direction.

We utilize the inclination angle to characterize the final shapes of the vesicles. When $t > 60$ s, $p_2$ dominates the shape of the vesicle and $\theta \approx 45°$ as seen in Figure 3.25[a] and [b]. The final shapes are oscillating between $38°$ and $51°$. In Figure 3.25[c], we contrast the shapes and corresponding Fourier modes of the vesicle shapes at $t = 108.3s$ and $t = 144.5s$, which almost overlap. By performing realizations of the stochastic model, we estimate the distribution of the angle $\theta$. This is shown in 3.25[d], and it follows a normal distribution with $\bar{\theta} = 44.99°$. Finial shapes and corresponding Fourier modes in different stochastic realizations are compared in Figure 3.25[e]. All the morphologies are nearly overlapped, thus we can conclude that this finial shape is robust.

Summarizing, in this chapter, we investigated the dynamics of vesicles in quiescent and time-varying flow. When periodical reversals of extensional flows are performed, the vesicle

dynamics are turned to follow a 3-stage dynamical process. In the first stage, high-order wrinkles are activated by the negative surface tension and decay rapidly. Next, the periodic reversals create non-trivial vesicle shapes whereas in the 2$^{\text{nd}}$ stage, the shapes are 4-fold symmetric using deterministic model, and 3-fold using stochastic model. This is due to mode interaction and denominated by the perturbation theory. So, we can 'control' shapes to a certain extent. Next, we study the dependence of the wrinkling dynamics and shape control as a function of the extensional flow rate $S$ and the threshold $C_h$.
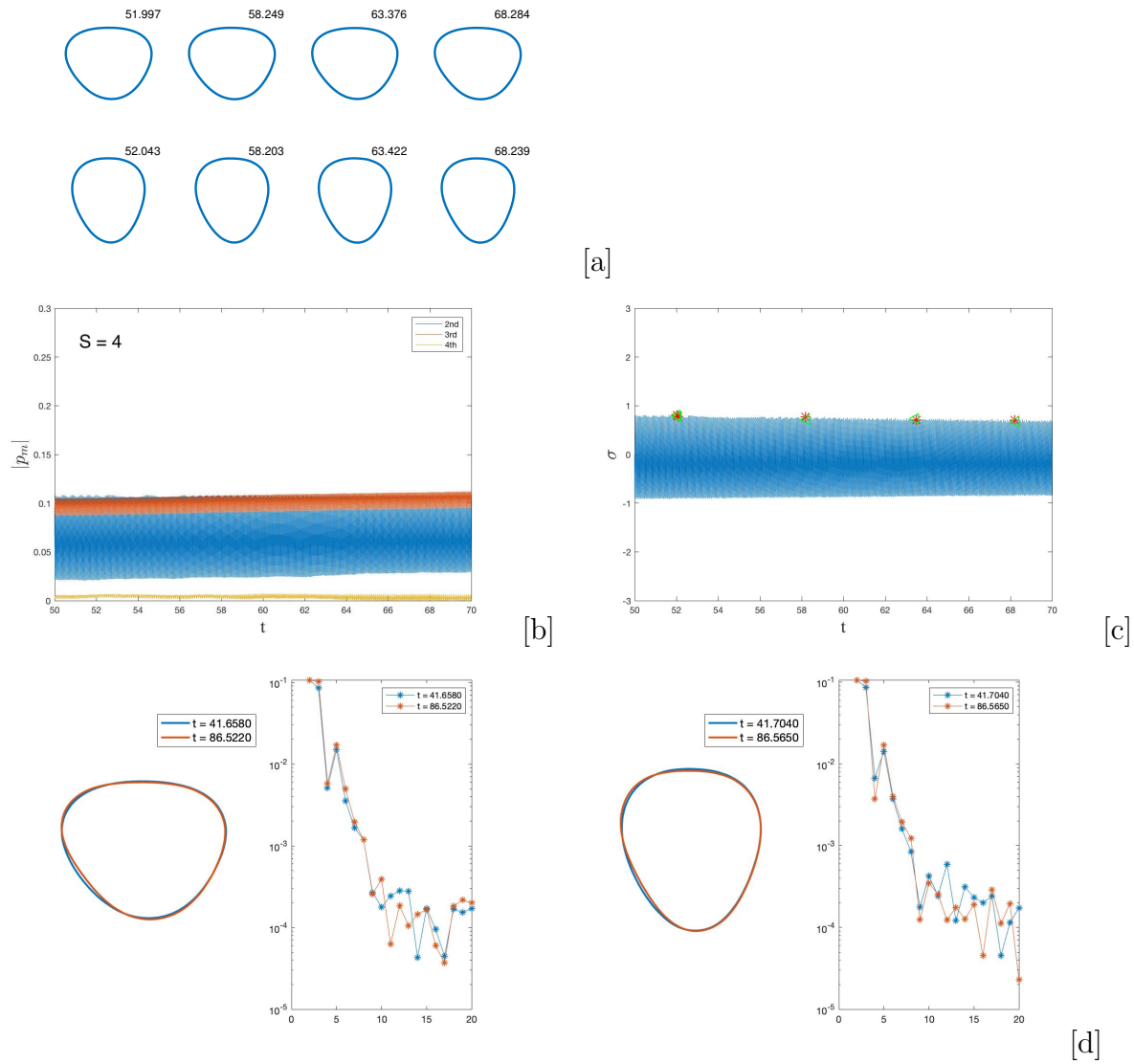
Figure 3.12: Stochastic wrinkling dynamics of a quasi-circular vesicle. Stage 2: [a] Shapes of the vesicle at the labeled time. [b] Fourier spectra. [c] Surface tension. [d] Comparison of shapes.
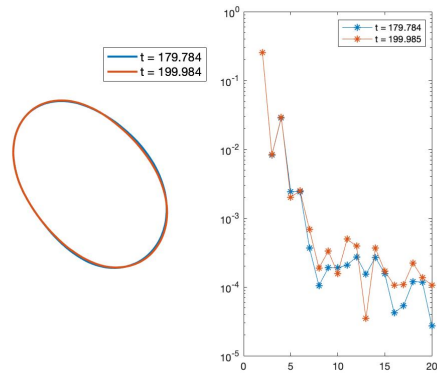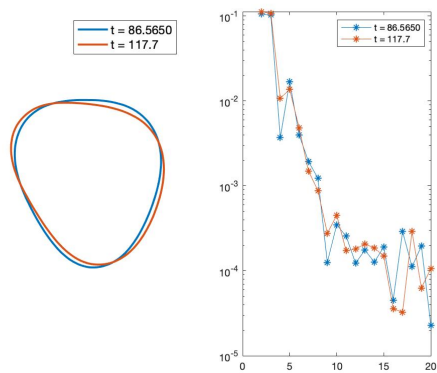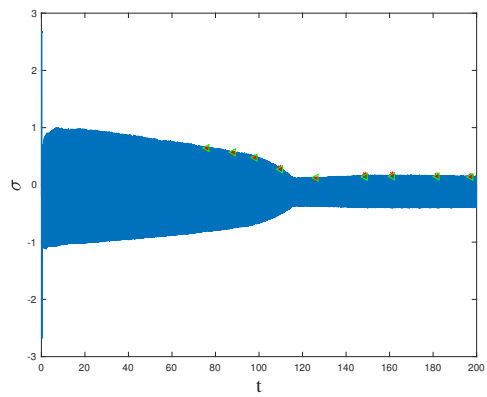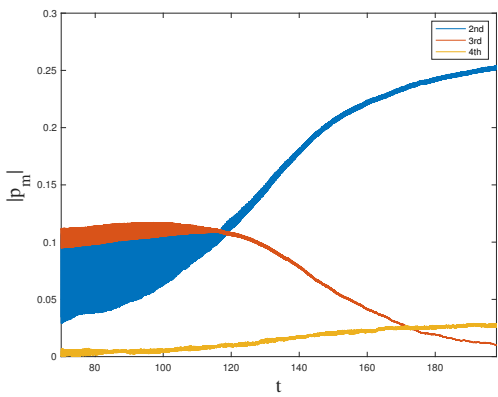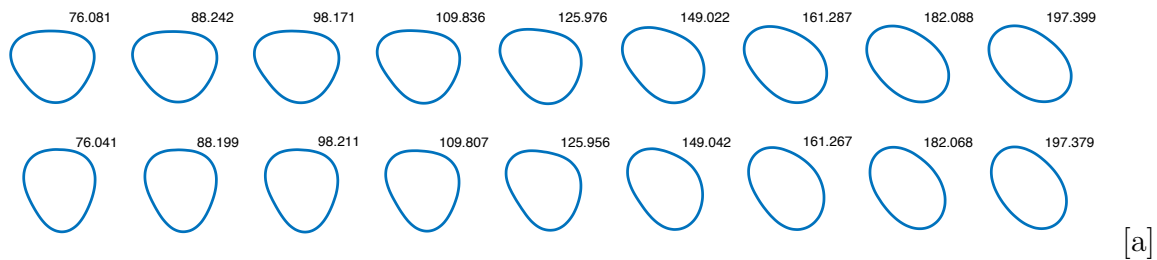
Figure 3.13: Stochastic wrinkling dynamics of a quasi-circular vesicle. Stage 3: [a] Shapes of the vesicle at the labeled time. [b]Fourier spectra. [c]Surface tension. [d]Comparison of shapes.
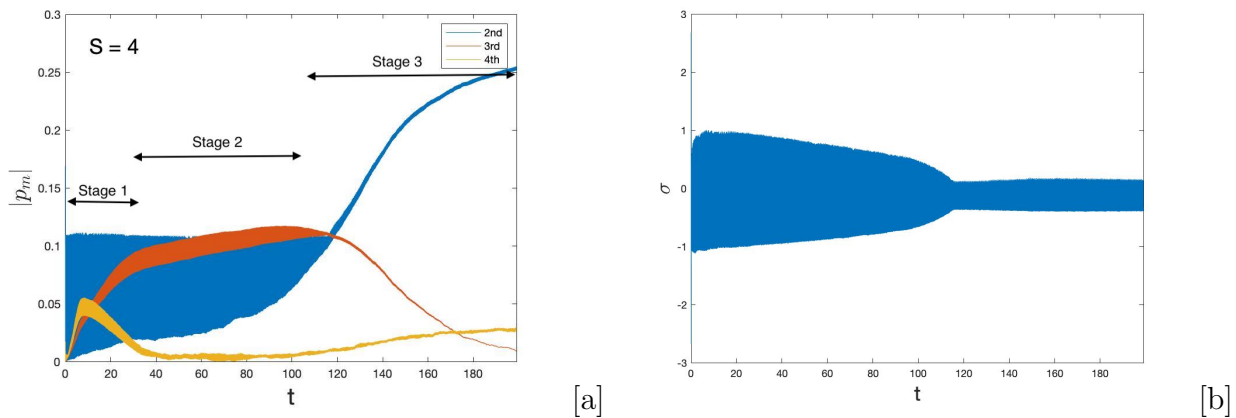
Figure 3.14: Stochastic wrinkling dynamics of a quasi-circular vesicle. [a]Fourier spectra. [b] Surface tension.
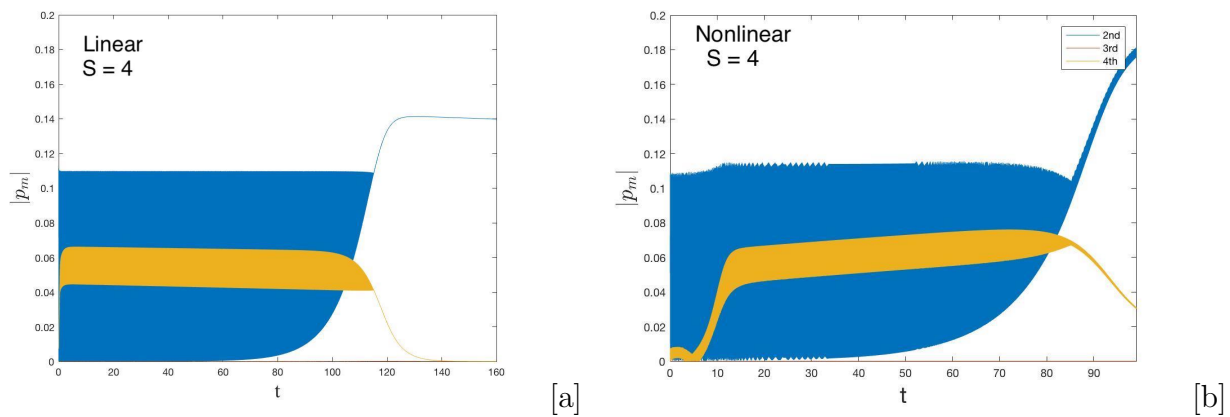


Figure 3.15: Comparison of Fourier spectra. [a] Linear Theory. [b] Nonlinear Simulation.
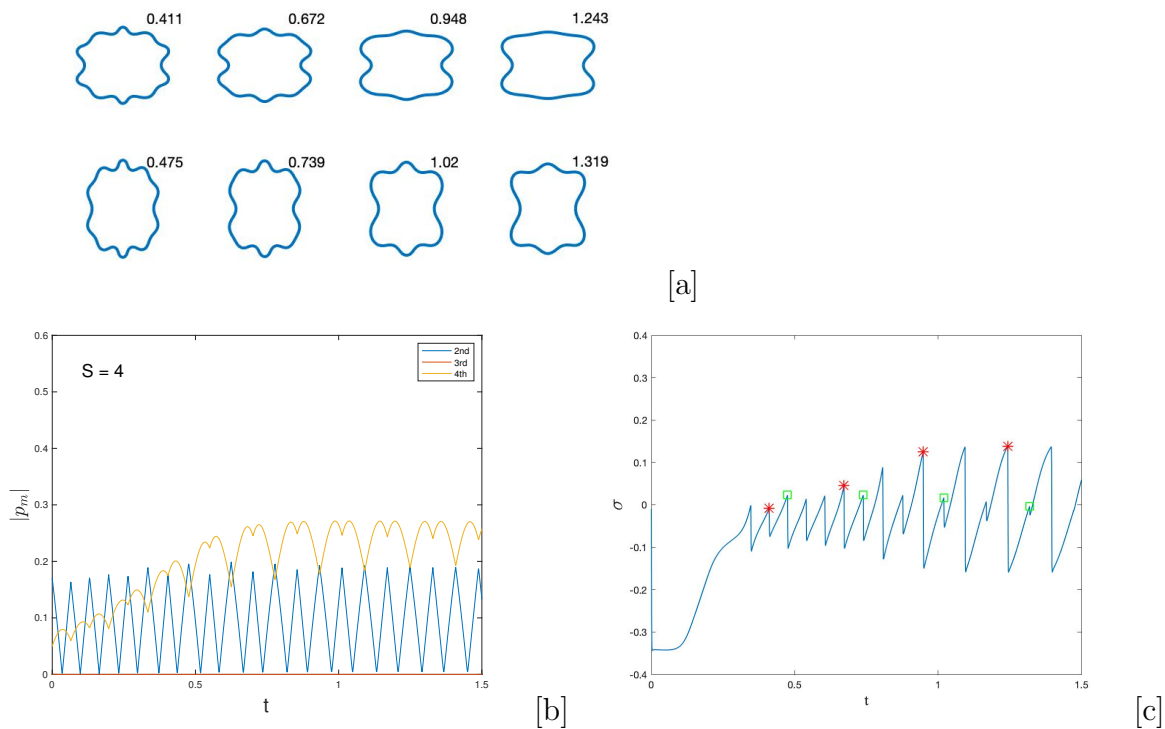
Figure 3.16: Deterministic wrinkling dynamics of an elongated vesicle. Stage 1 [a]Dynamics of the vesicles versus time t. [b] Fourier spectra. [c]Surface tension.
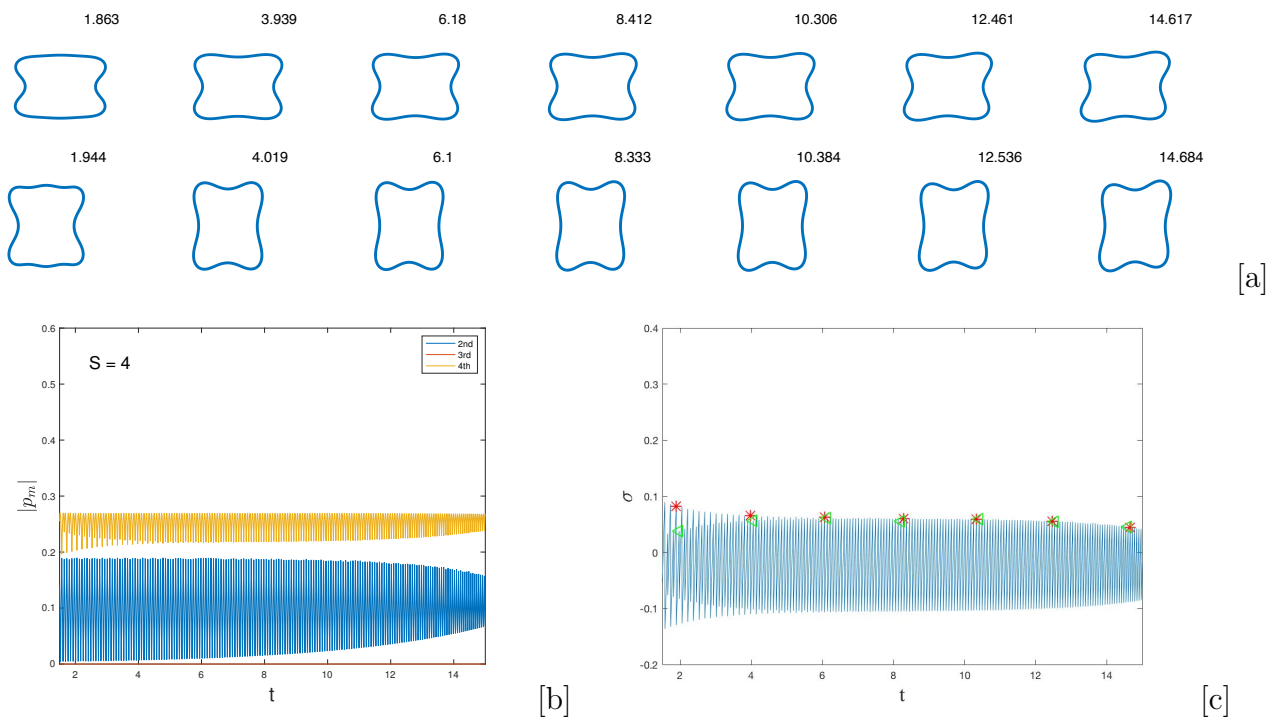


Figure 3.17: Deterministic wrinkling dynamics of an elongated vesicle. Stage 2 [a] Dynamics of the vesicles versus time t. [b] Fourier spectra. [c]Surface tension.

15.411    15.752    16.59    17.9    19.904    23.912    27.92

15.205    15.809    16.635    17.92    19.924    23.932    27.94

[a]

[b]

[c]
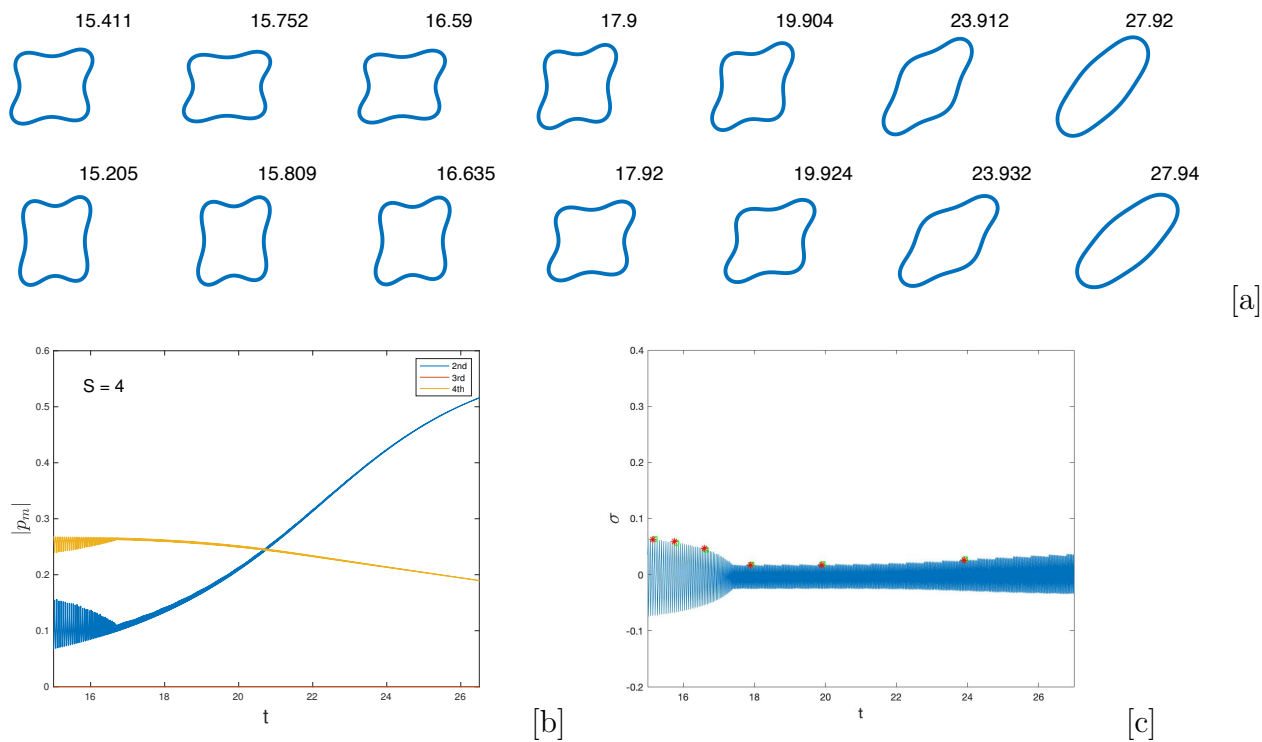
Figure 3.18: Deterministic wrinkling dynamics of an elongated vesicle. Stage 3 [a] Dynamics of the vesicles versus time t. [b] Fourier spectra. [c]Surface tension.

[a]

[b]
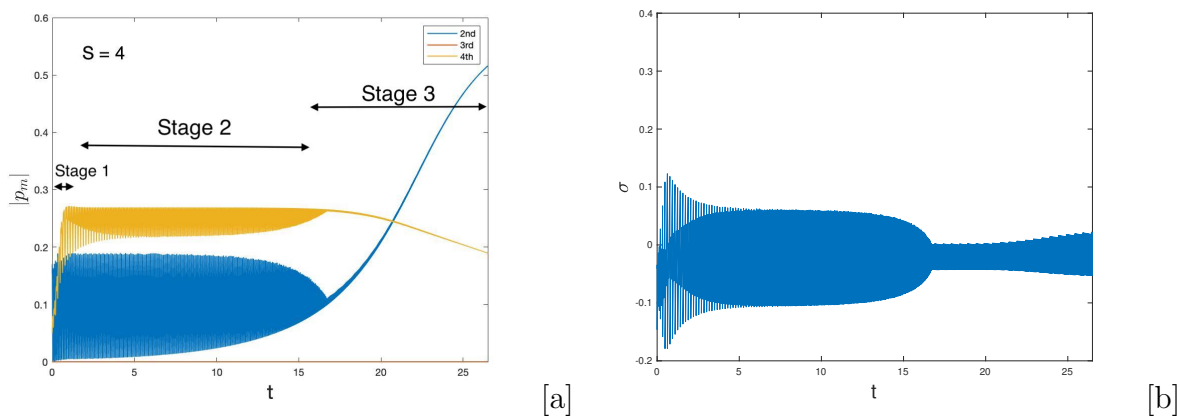
Figure 3.19: Deterministic wrinkling dynamics of an elongated vesicle. [a]Fourier spectra. [b]Surface tension

54
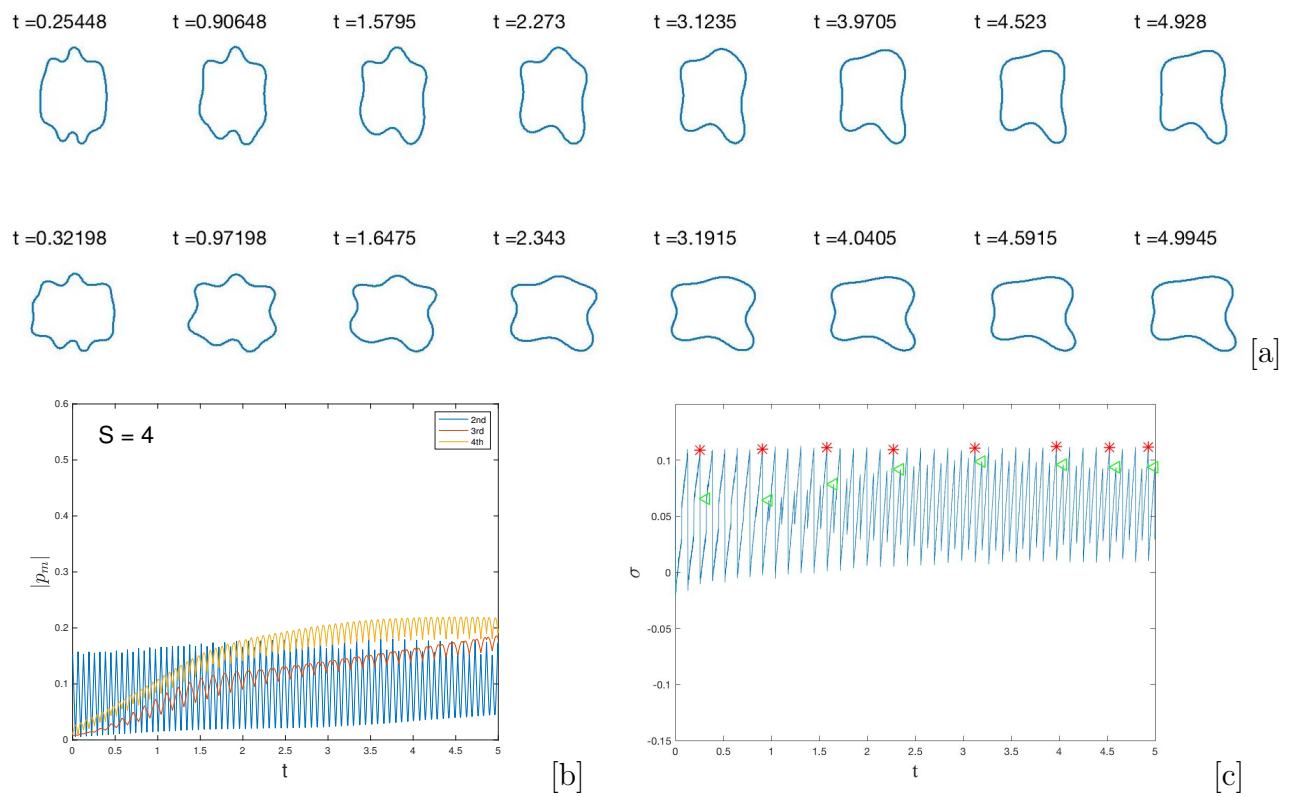
Figure 3.20: Stochastic wrinkling dynamics of an elongated vesicle. Stage 1 [a] Dynamics of the vesicles versus time t. [b] Fourier spectra. [c]Surface tension.
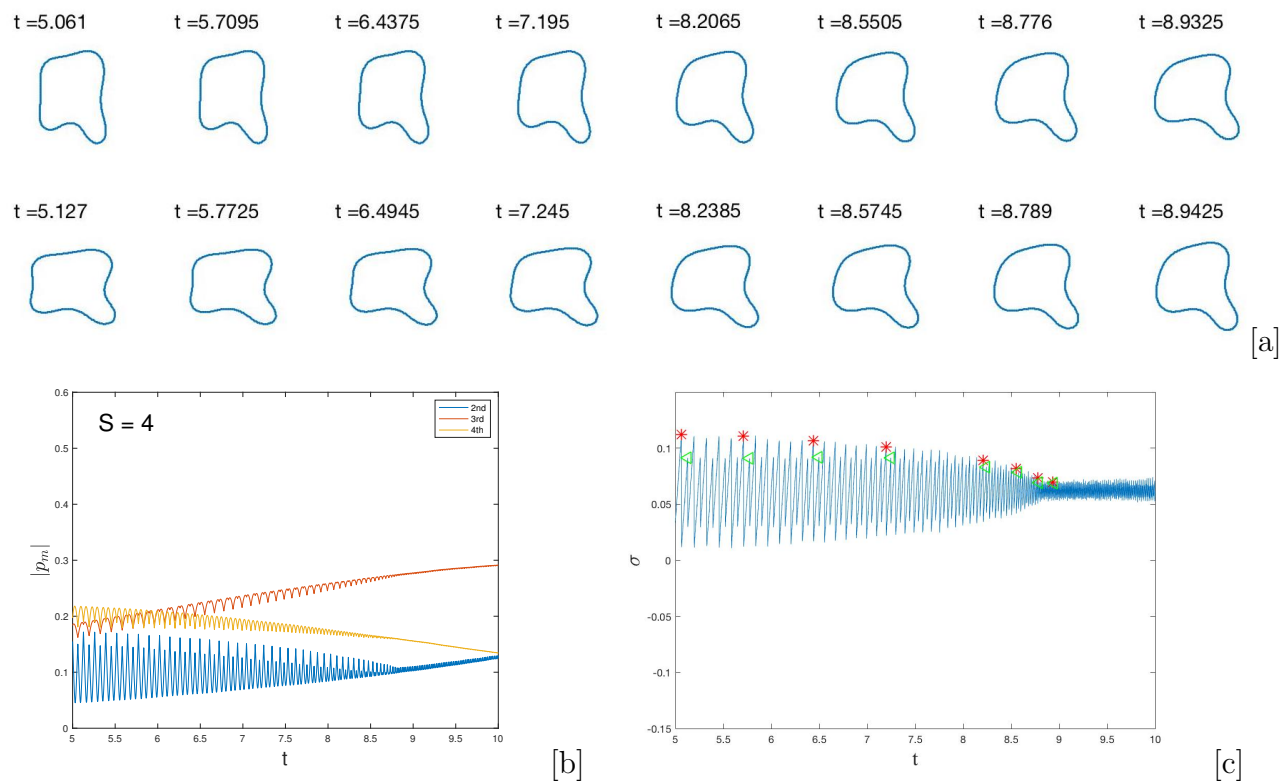
Figure 3.21: Stochastic wrinkling dynamics of an elongated vesicle. Stage 2 [a] Dynamics of the vesicles versus time t. [b] Fourier spectra. [c]Surface tension.
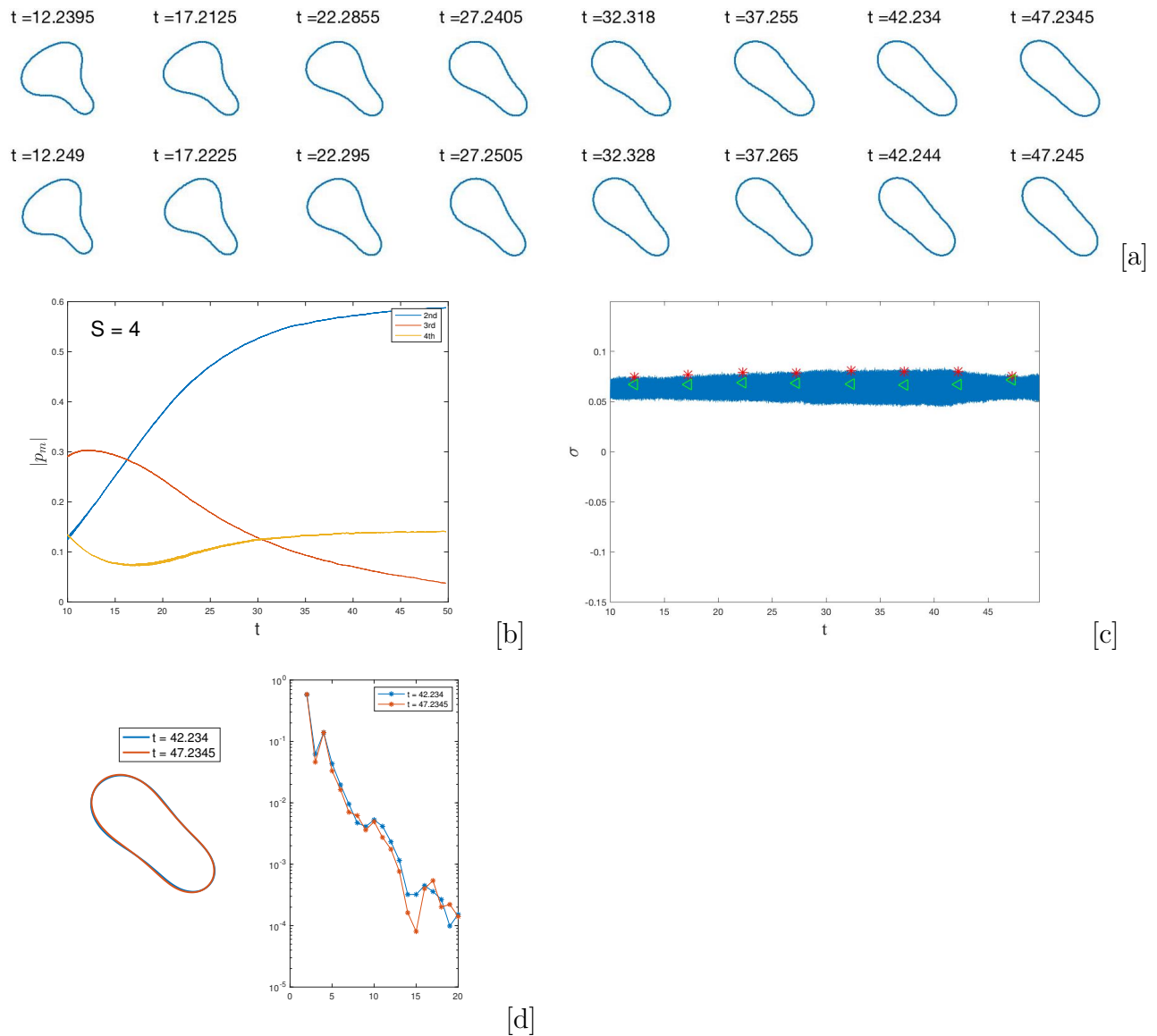
Figure 3.22: Stochastic Wrinkling dynamics of an elongated vesicle. Stage 3 [a] Dynamics of the vesicles versus time t. [b] Fourier spectra. [c]Surface tension. [d] Comparison of finial shapes.
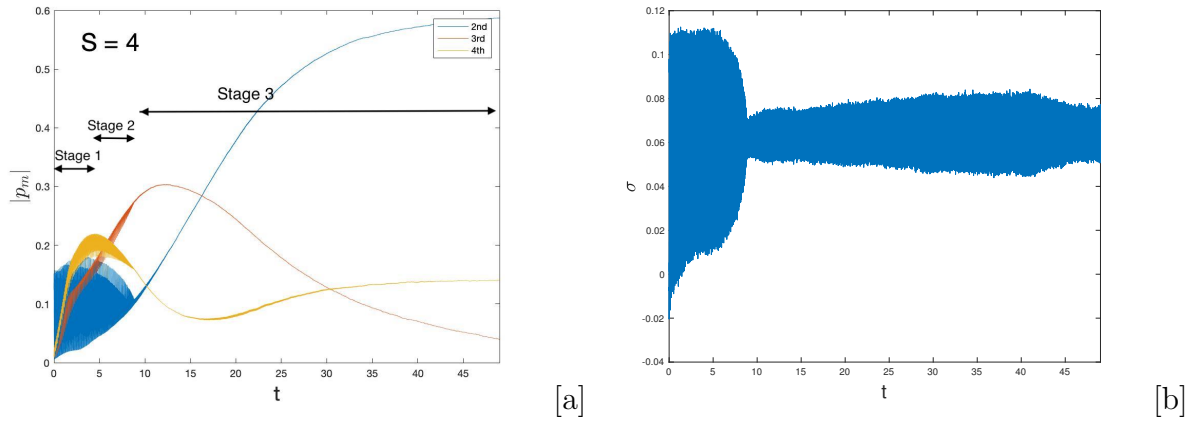
Figure 3.23: Stochastic wrinkling dynamics of an elongated vesicle. [a]Fourier spectra. [b]Surface tension
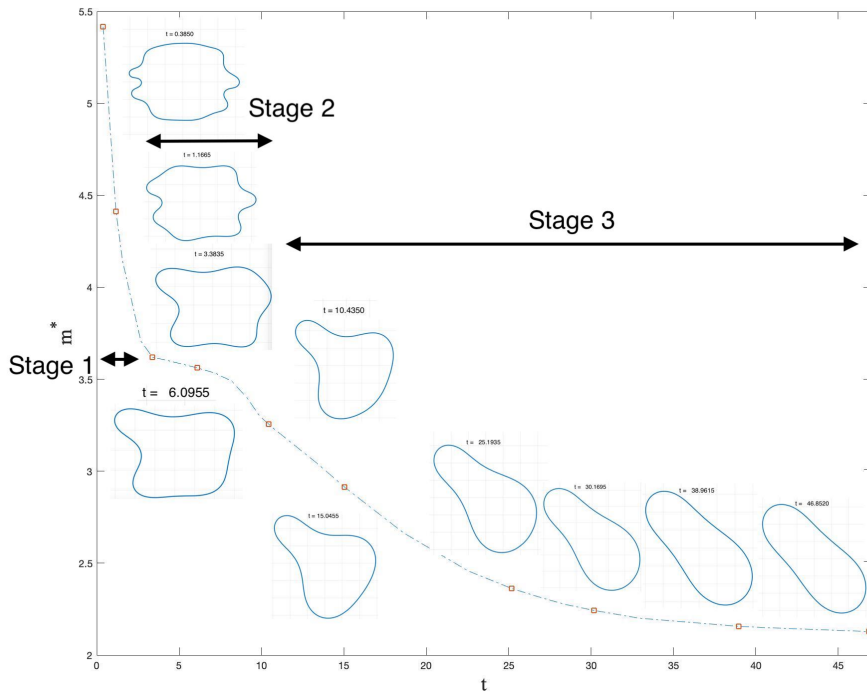


Figure 3.24: The evolution of dominant mode $m^*$ versus time, with vesicle morphologies at labeled time.

58
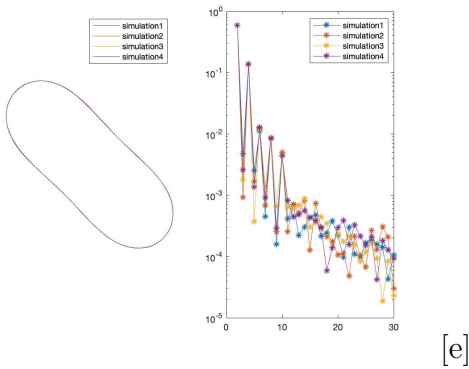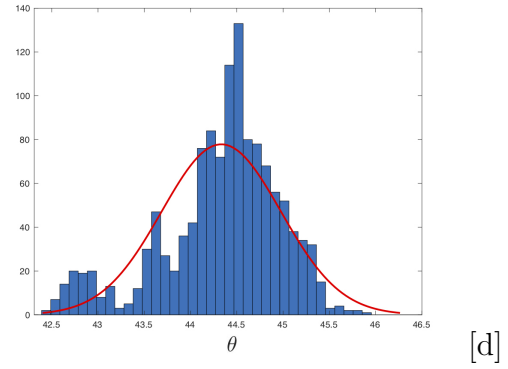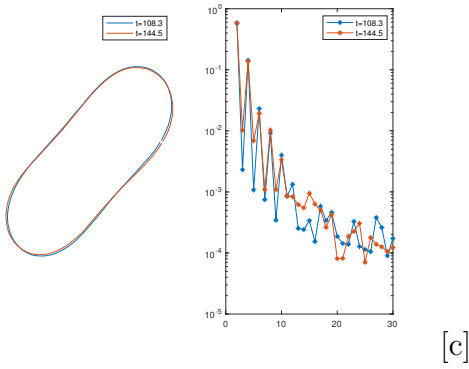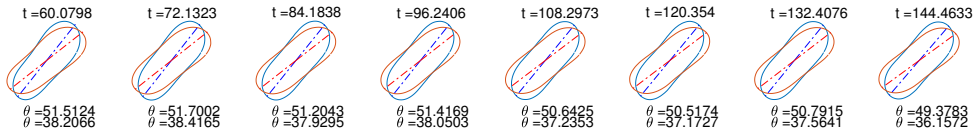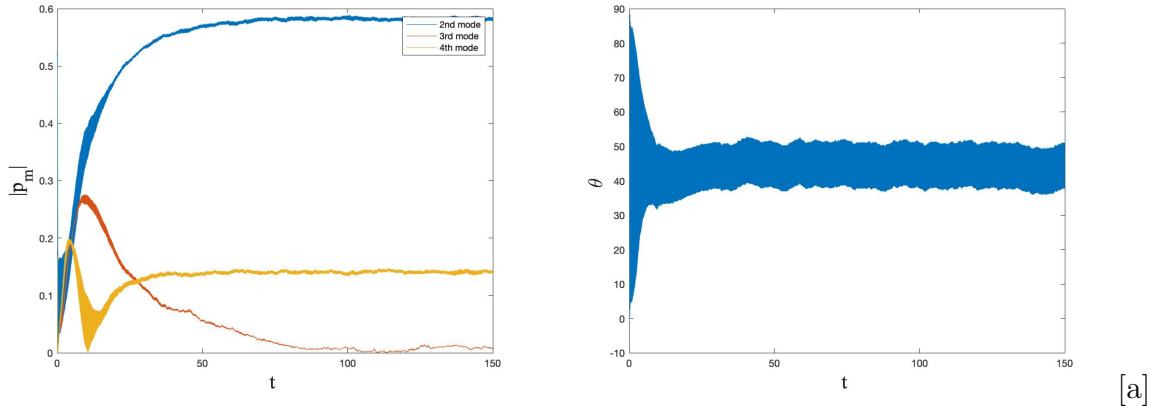
Figure 3.25: Analysis of the inclination angle. [a] Time evolution of Fourier modes and inclination angle. [b] Vesicle shapes at labeled time. [c] Comparison of the final shapes. [d] Inclination angle distribution. [e] Finial shapes in 4 realizations.

59

# Chapter 4

# Parameter Study for Elongated Vesicles

In this chapter, we investigate the dependence of the wrinkling dynamics on the extensional flow rate $S$ and threshold $C_h$. Here we focus on the dynamics of elongated vesicles in periodically reversed extensional flows. In all cases discussed here, the initial shape of a vesicle is an ellipse with major axis $a = 2 \times 10^{-5}$ m and minor axis $b = 0.8 \times 10^{-5}$ m, i.e., aspect ratio $a : b = 1 : 0.4$ and excess arc length $\Delta = 0.994$.

## 4.1 Dependence of Wrinkling on the Extensional Flow Rate

We first investigate the dependence of the wrinkling dynamics of different extensional flow rate S. Here we set the spatial scale $L_d = L_{\mathrm{odj}}$ and the threshold $C_h = 100$. Figures 4.1 - 4.4 show the dynamics of vesicles in viscous fluid with a flow whose direction is reversed when $|p_2|$ reaches the threshold $C_h$ with flow rate $S$ from 4 to 32. In each plot, we display

deterministic simulations in Figures [a][b] and stochastic realizations in Figures [c][d]. In Figure 4.1, the extensional flow rate $S = 4$. The entire dynamics are shown earlier (Figure 3.16 - 3.22). The shapes of the vesicle are shown at the time just before the flow reversal (labeled points in Figure 4.1[a] left column). At the very beginning, high-order wrinkles are excited and quickly dominated by the 4th modes (see Figure 4.1[b] right). In the stochastic case, odd modes are activated and the shapes of the vesicle are no longer symmetric. Figure 4.1[d] (right) shows part of the stochastic dynamics when the morphological evolution of the vesicle is stable. Finger-like protrusions on stochastic vesicles are more pronounced, while, in the deterministic case, the vesicle looks a bit more square-like.

As the flow rate is increased to $S = 8$, even higher-order modes are excited (see Figure 4.2[a] and [c]), which is consistent with the results from [38]. However, as the direction of the flow continues to be reversed, higher-order wrinkles disappear and the 4th mode dominates the shapes of the vesicle, which is similar to the simulation with $S = 4$. Besides the 4th mode, we also observe a small 6th mode on the morphologies in Figure 4.2[b], which is not shown in Figure 4.1[b] for $S = 4$. And there are six obvious protuberances on the membrane in the stochastic simulation (see Figure 4.2[d]).

As we double the flow rate S again (see Figure 4.3), even higher-order wrinkles are excited by the large flow strength. In the deterministic dynamics (Figure 4.3[b]), the 4th mode dominates the shapes of the vesicle with a clear 6th mode. While the shapes in the stochastic realization (see Figure 4.3[d]) are 4-fold asymmetric.

For a larger flow rate $S = 32$, the morphological evolution of the vesicle is stable and controlled by the 4th mode in the deterministic dynamics, while it's controlled by higher-order modes in the stochastic cases.

Here we measure the characterized frequency of the shape of the vesicle at time $t'$ when the $p_2$ mode reaches its minimum during the last period in Figure 4.5. The dominant modes

$m^*$ in the deterministic simulations (dot-dashed) are quite stable as the flow rate increases, while the variation is much larger in the stochastic cases. The wrinkles on the vesicle are mostly characterized by the 4th mode. As the flow strength $S$ increases, the dominant mode $m^*$ grows slightly.

## 4.2    Dependence of Wrinkling on the Threshold

Next, we investigate the dependence of the wrinkling dynamics of different thresholds $C_h$. We set the aspect ratio $a : b = 1 : 0.4$, the flow strength $S = 4$ and $L_d = L_{\text{odj}}$ in the stochastic model. The threshold $C_h$ varies from 20 to 200.

The dynamics of the vesicle with the threshold $C_h = 20$ in deterministic and stochastic simulations are shown in Figure 4.6. In Figure 4.6[b], we observe that the morphological evolution of the vesicle is stable and mostly dominated by 4th mode in the deterministic simulation with $\Delta t' = 0.272$, where $\Delta t'$ is the period defined as the time period between two peaks of surface tension (yellow interval in Figure 4.6[b]). For the stochastic realization, the shapes of the vesicle are mostly dominated by the 5th mode as seen in Figure 4.6[d], and the corresponding period is slightly small $\Delta t' = 0.256$. This is because when thermal fluctuations are included, the odd modes break the symmetry of the vesicle, enable the change on surface tension to occur more rapidly and reduce the time for $p_2$ to reach the threshold.

As $C_h$ is increasing to 50 (see Figure 4.7), the shapes of the vesicle are controlled by 4th mode in both deterministic and stochastic cases. The period $\Delta t' = 0.448$ in the deterministic simulation is significantly larger than it in the stochastic simulation ($\Delta t' = 0.272$).

In Figure 4.8, As $C_h$ grows to 100, $\Delta t'$ increases to 0.64 in deterministic dynamics and 0.496 in stochastic dynamics. If we continue to increase $C_h = 200$ (Figure 4.9), the morphologies of the vesicle are dominated by 4th mode in both deterministic, and the deterministic period

$(\Delta t' = 0.928)$ is still slightly longer than the stochastic one $(\Delta t' = 0.912)$.

To summarize, Figures 4.10 [a] - [d] show the changes of $\Delta t'$ versus time for different threshold $C_h$. In the deterministic cases (blue line), the period converges in time $t'$. However, in the stochastic realizations, the convergence of $\Delta t'$ is not clear. The red boxes show the means of 5 simulations with error bars that indicate the maximum and minimum values for the different realizations. Variability increases over time. Figure 4.10 [e] shows the periods $\Delta t'$ with different $C_h$. Because the thermal fluctuations accelerate the growth and decay of the surface tension, the stochastic periods are always shorter than the deterministic periods.

Finally, we compare the final shape (as time is large enough) with different $C_h$ using stochastic model in Figure 4.11. The final shapes are all biconcave and nearly overlapped.

In this chapter, we analyzed the effects of the extensional flow strength $S$ and the threshold $C_h$ on the dynamics of an elongated vesicle in a periodical reversal flow. As $S$ increases, the dominant modes $m^*$ are stable around 4 in the deterministic simulations, in contrast, the variation for the stochastic realizations are much larger. As $C_h$ increases, the period $\Delta t'$ increases and the deterministic period is always longer than the stochastic period due to thermal fluctuations. By now, we focus on the impermeable vesicles. In the next chapter, we concentrate on some permeable vesicles.
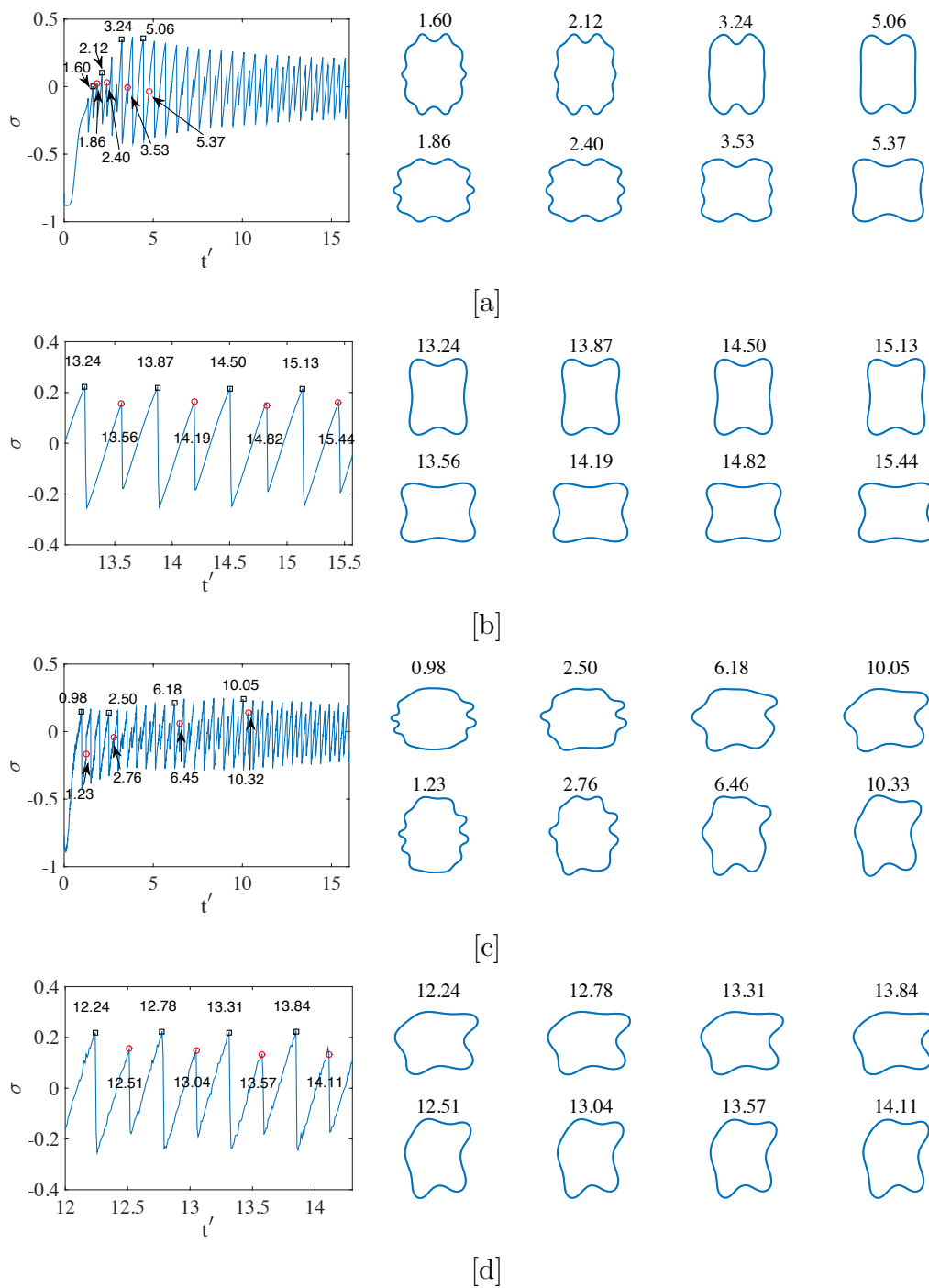
Figure 4.1: $S = 4$. [a] deterministic dynamics, [b] part of the deterministic dynamics where the morphological evolution of the vesicle is stable. [c] stochastic dynamics, [d] part of the stochastic dynamics where the morphological evolution of the vesicle is stable.
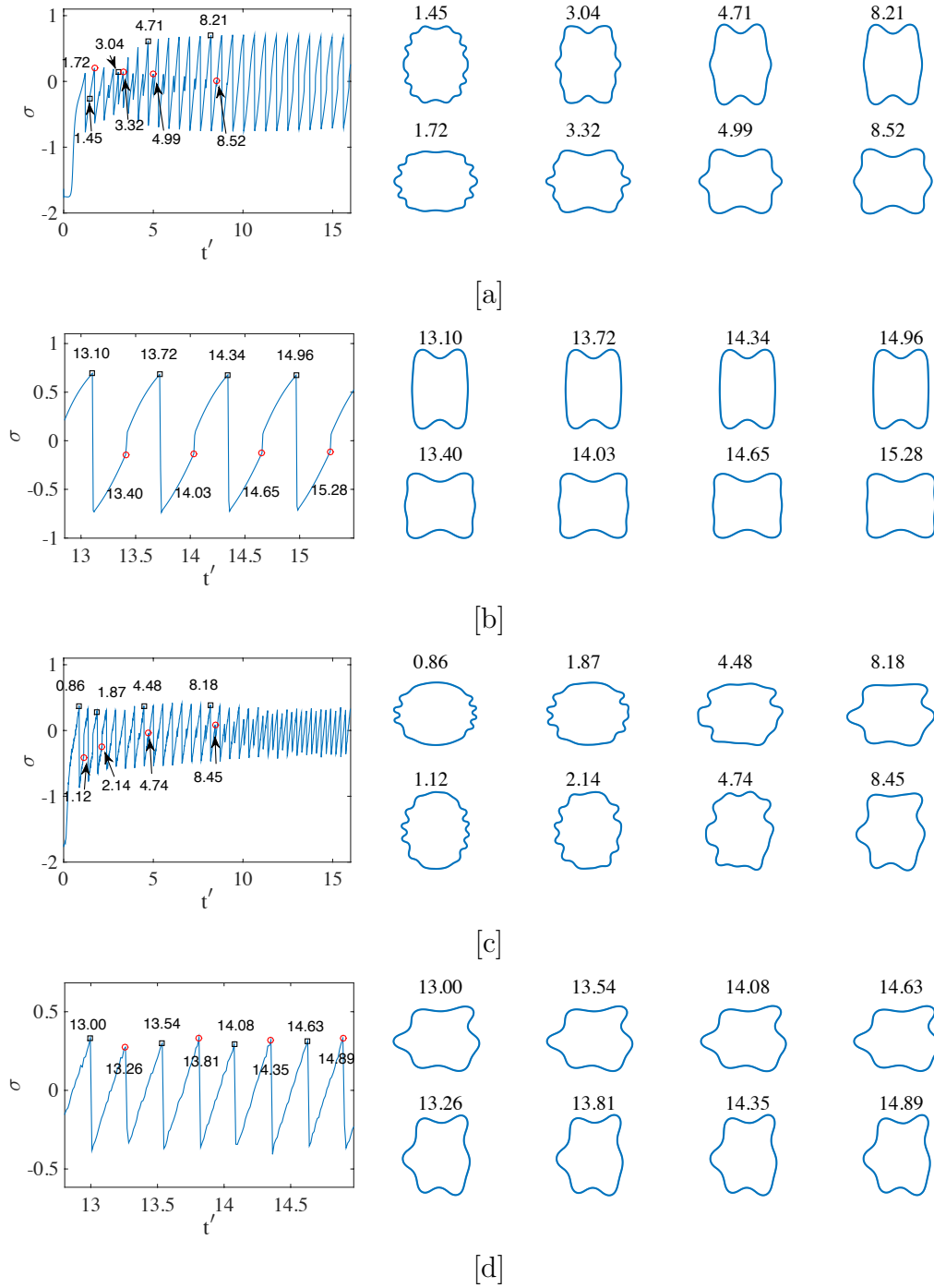
Figure 4.2: $S = 8$. [a] deterministic dynamics, [b] part of the deterministic dynamics where the morphological evolution of the vesicle is stable [c] stochastic dynamics, [d] part of the stochastic dynamics where the morphological evolution of the vesicle is stable.
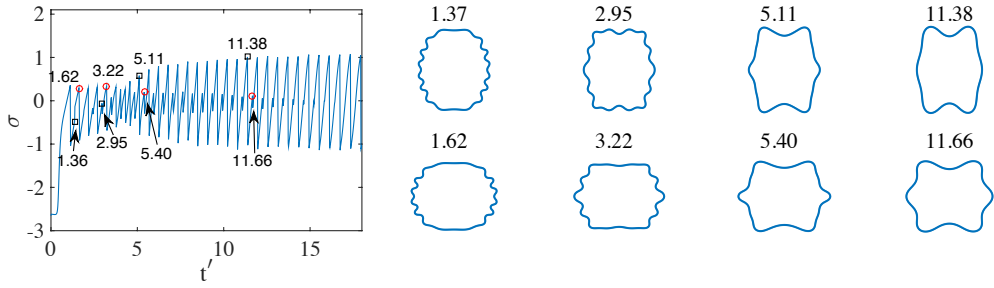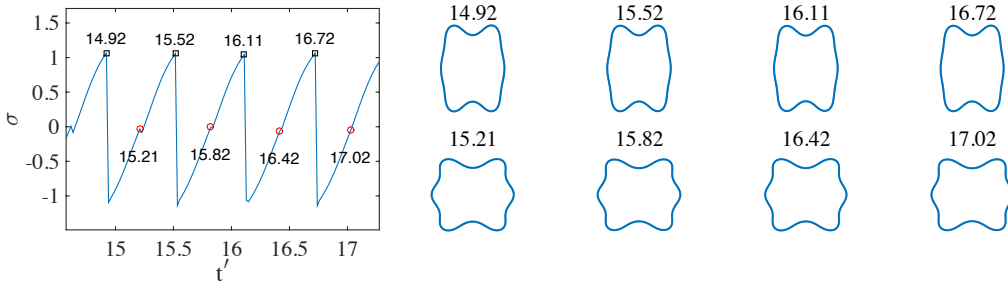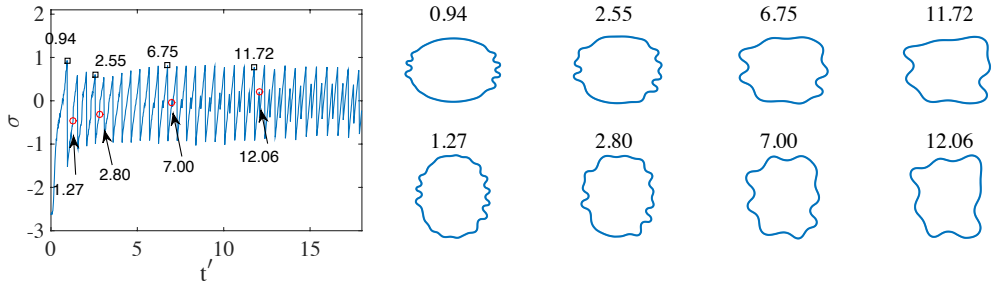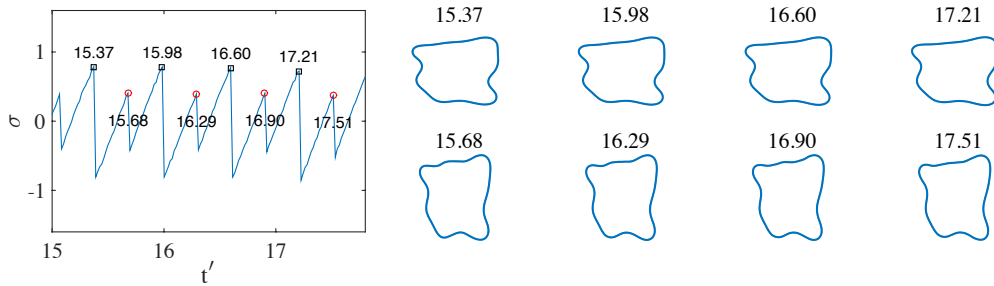
Figure 4.3: $S = 16$ [a] deterministic dynamics, [b] part of the deterministic dynamics where the morphological evolution of the vesicle is stable. [c] stochastic dynamics, [d] part of the stochastic dynamics where the morphological evolution of the vesicle is stable.
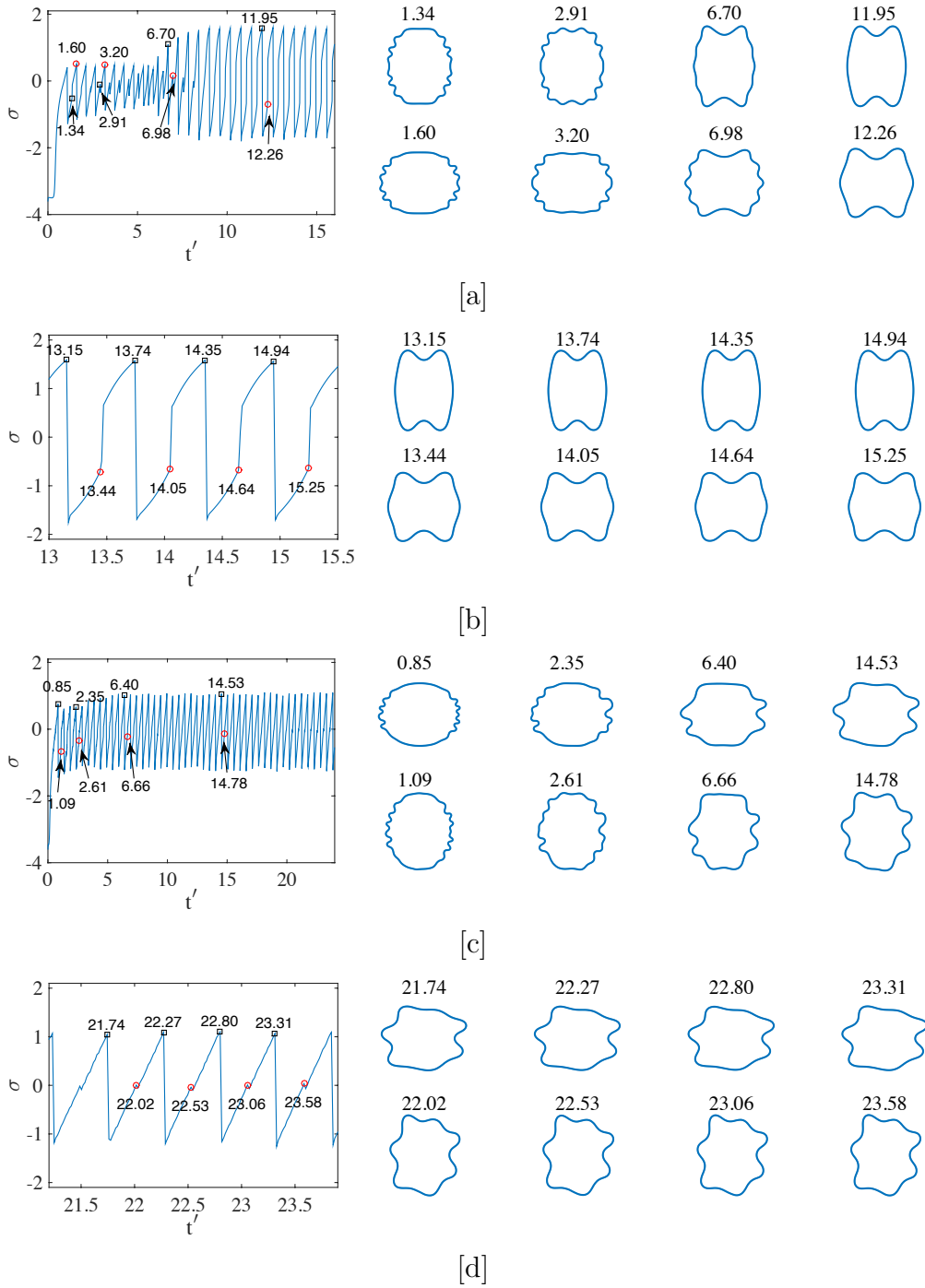
Figure 4.4: $S = 32$. [a] deterministic dynamics, [b] part of the deterministic dynamics where the morphological evolution of the vesicle is stable [c] stochastic dynamics, [d] part of the stochastic dynamics where the morphological evolution of the vesicle is stable.

67
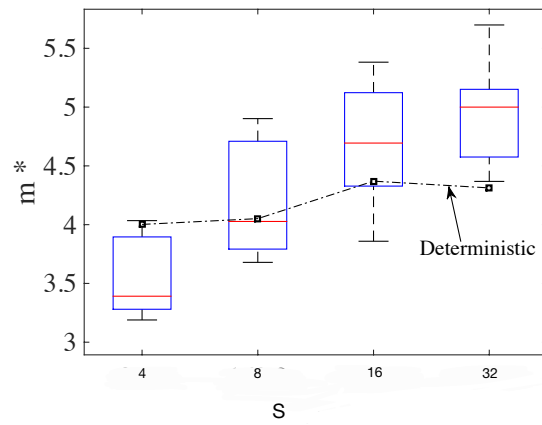
Figure 4.5: The dominant modes $m^*$ of the vesicle versus the flow strength.
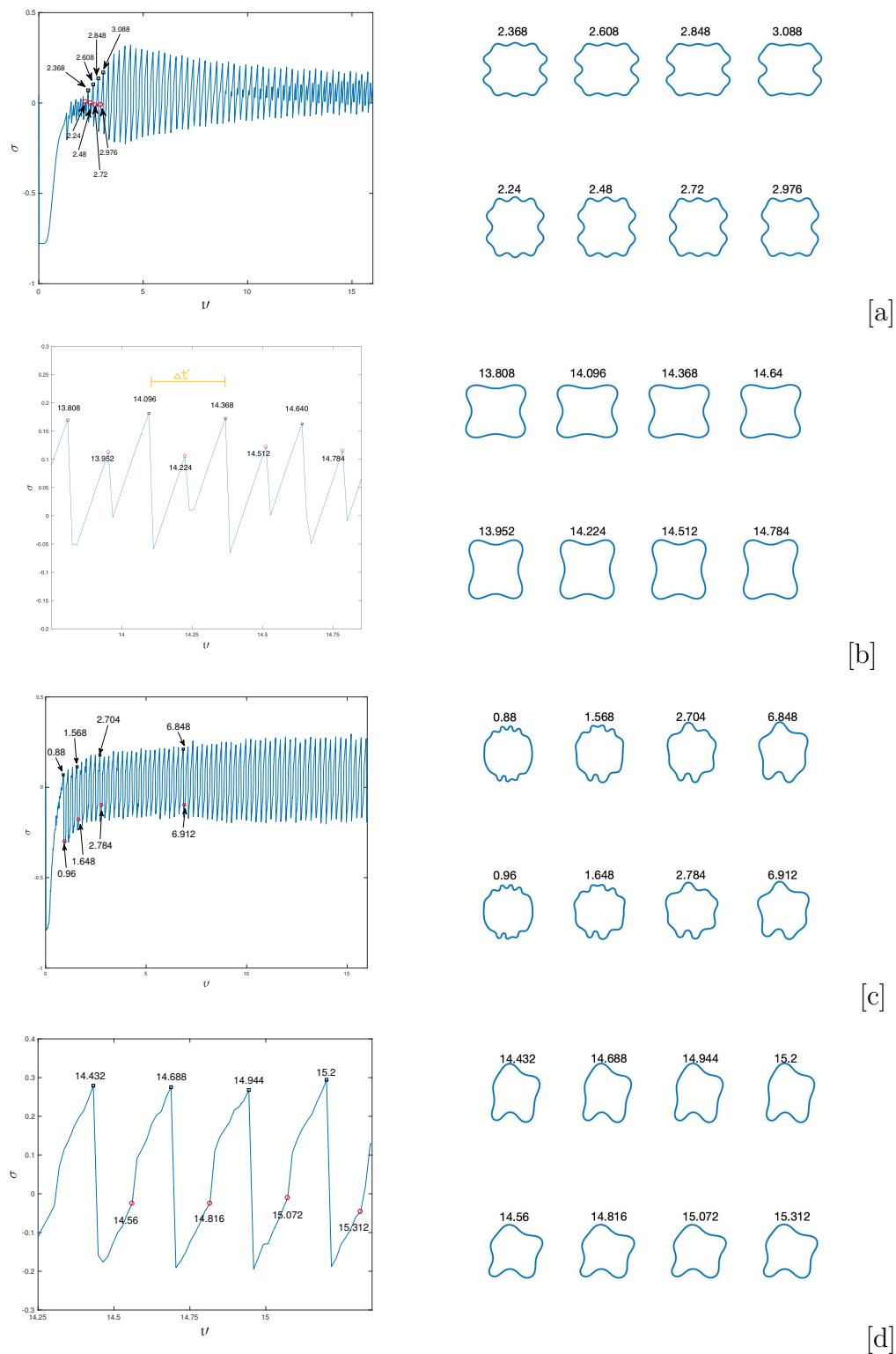
Figure 4.6: $C_h = 20$. [a] deterministic dynamics, [b] part of the deterministic dynamics where the morphological evolution of the vesicle is stable [c] stochastic dynamics, [d] part of the stochastic dynamics where the morphological evolution of the vesicle is stable.
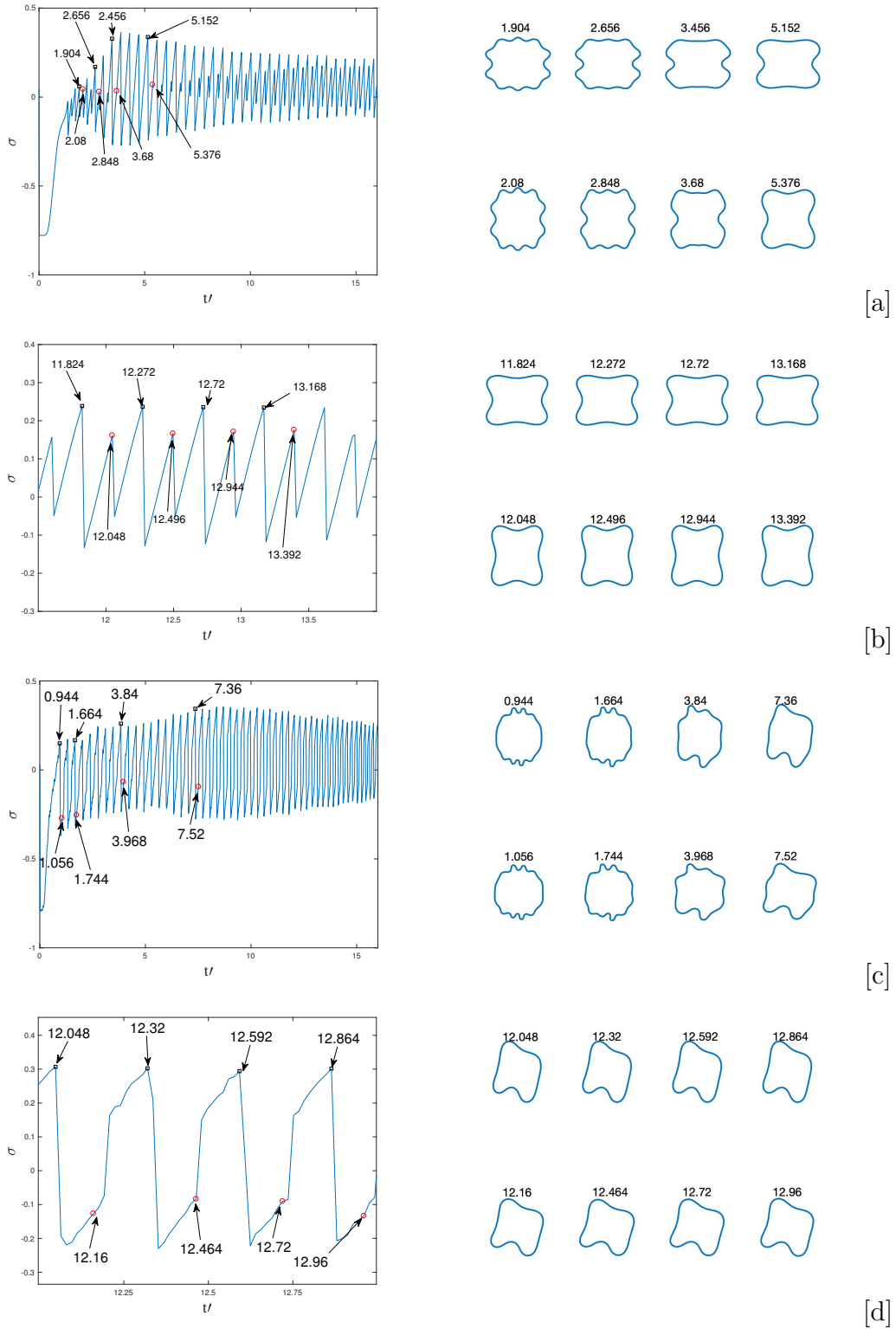
Figure 4.7: $C_h = 50$. [a] deterministic dynamics, [b] part of the deterministic dynamics where the morphological evolution of the vesicle is stable [c] stochastic dynamics, [d] part of the stochastic dynamics where the morphological evolution of the vesicle is stable.

70
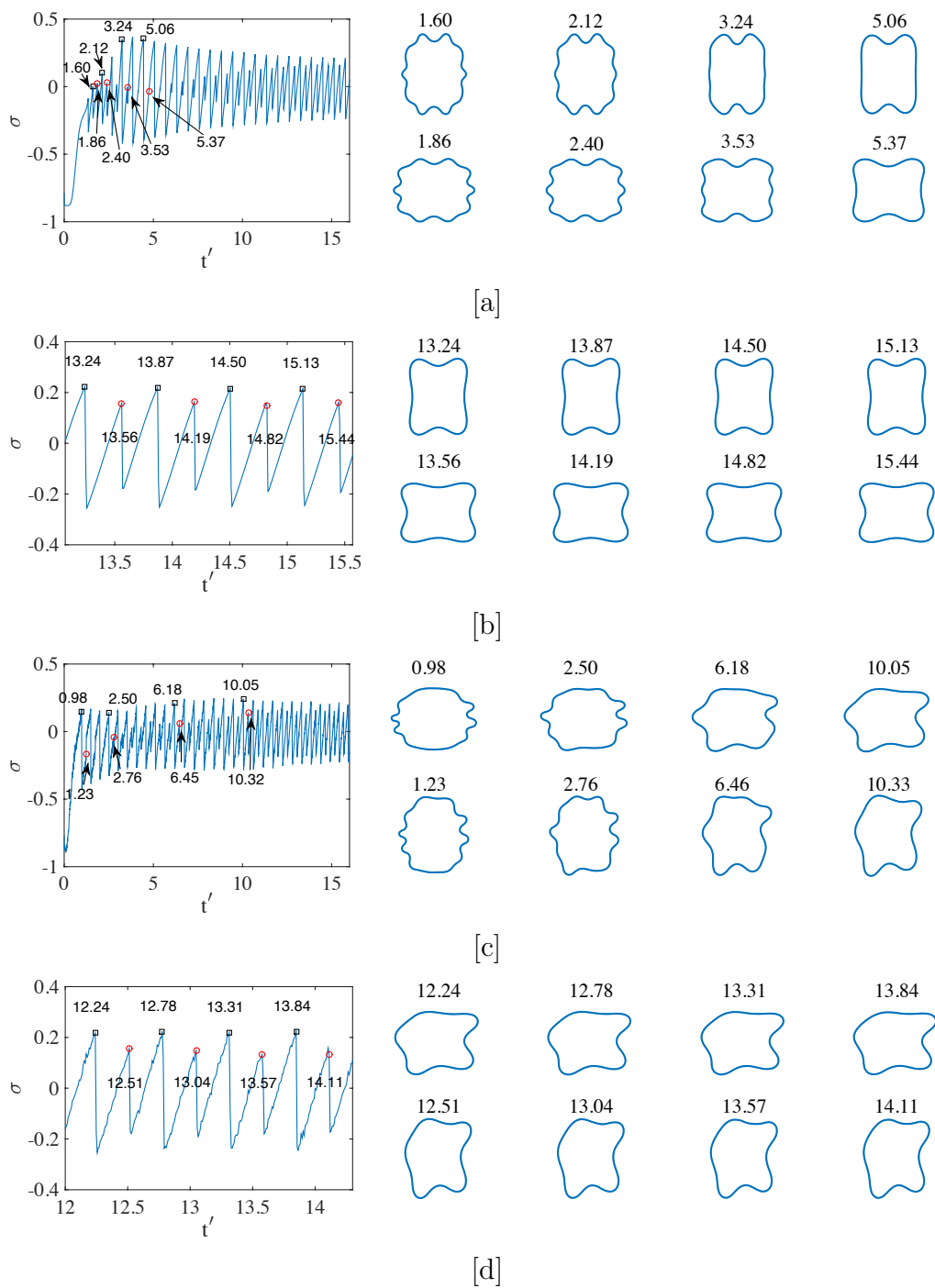
Figure 4.8: $C_h = 100$. [a] deterministic dynamics, [b] part of the deterministic dynamics where the morphological evolution of the vesicle is stable [c] stochastic dynamics, [d] part of the stochastic dynamics where the morphological evolution of the vesicle is stable.
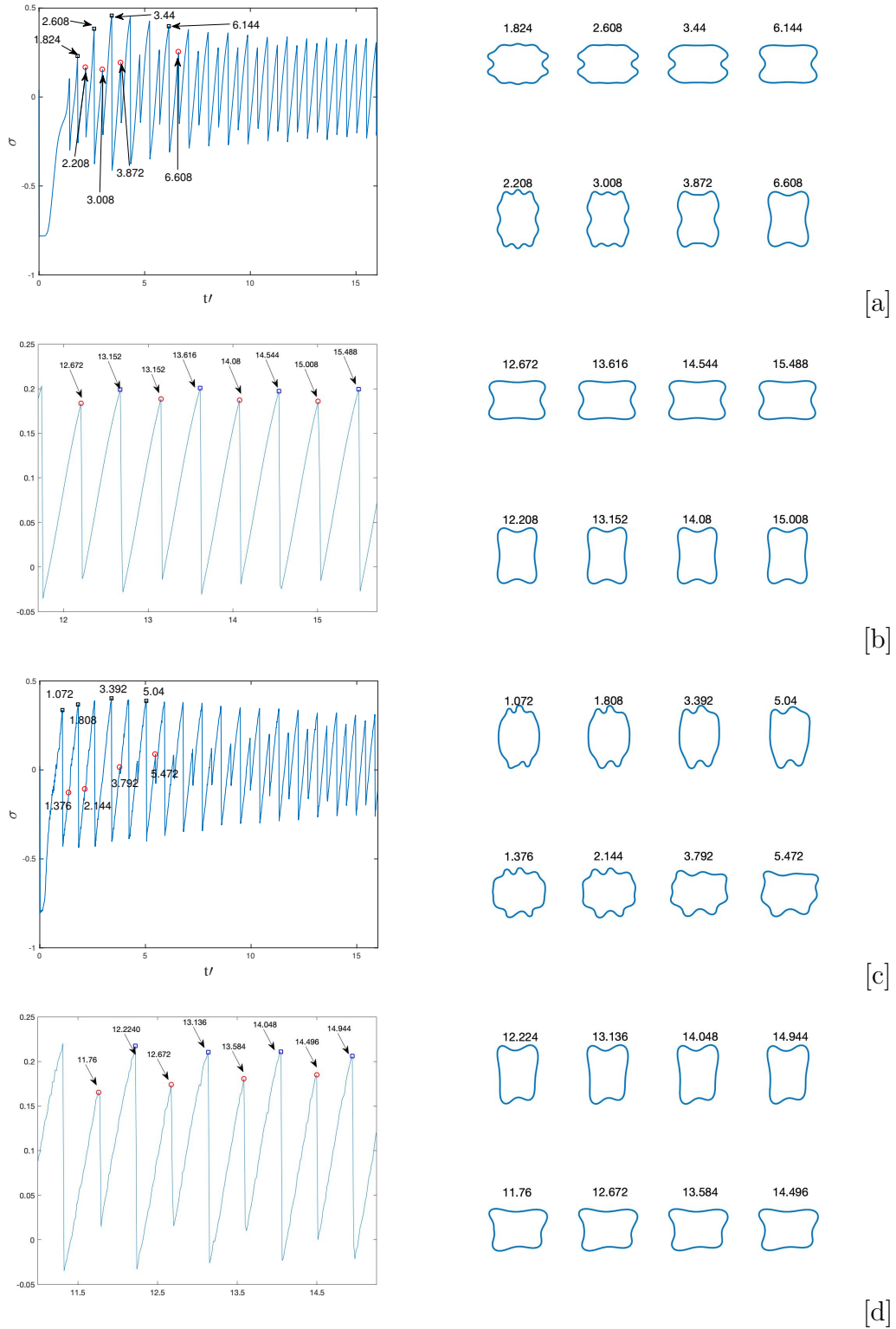
Figure 4.9: $C_h = 200$. [a] deterministic dynamics, [b] part of the deterministic dynamics where the morphological evolution of the vesicle is stable [c] stochastic dynamics, [d] part of the stochastic dynamics where the morphological evolution of the vesicle is stable.
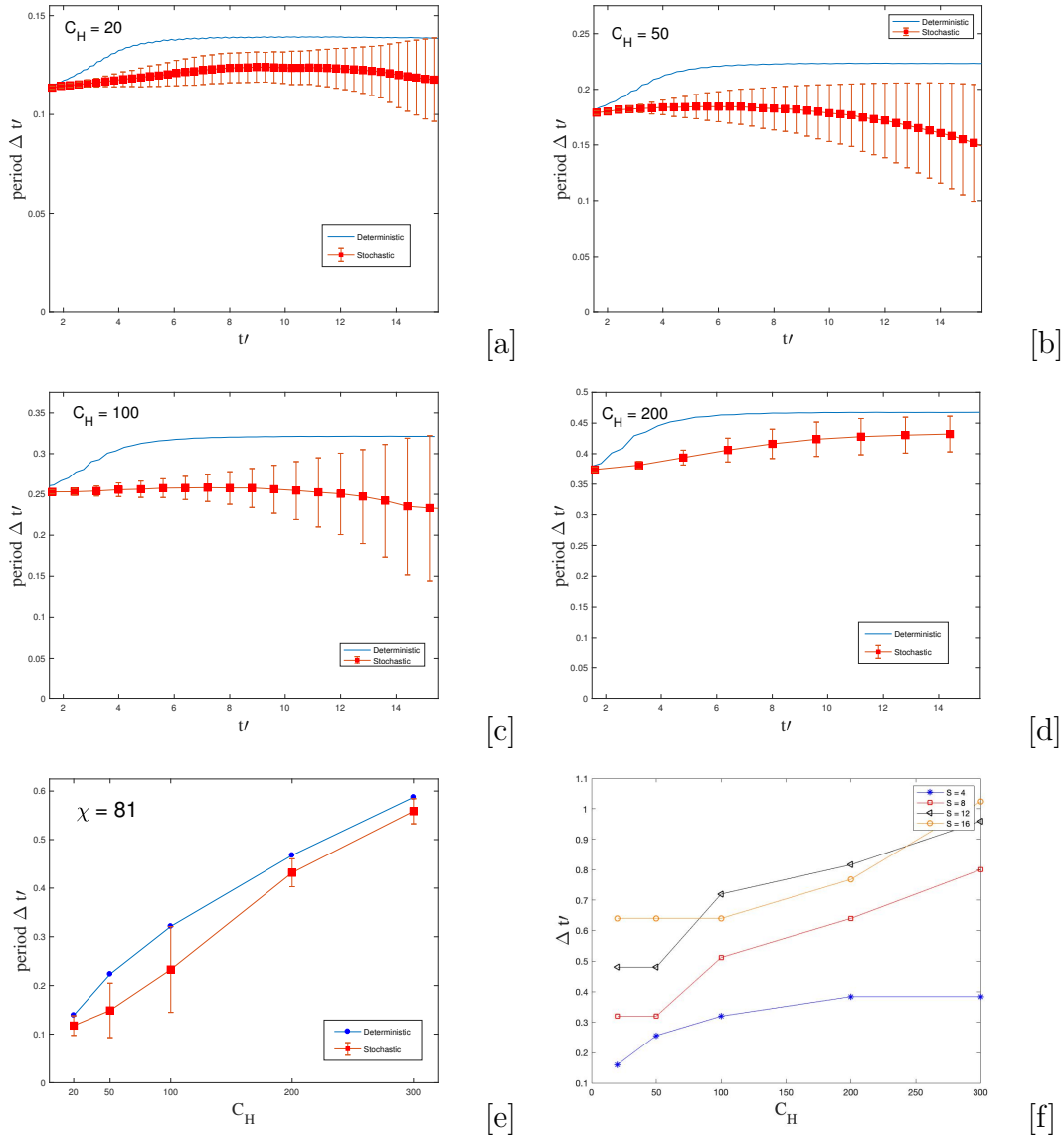
Figure 4.10: [a]-[d]Periods vs time in both deterministic and stochastic models. [e]Periods under different $C_h$ in both deterministic and stochastic models. [f] Periods as a function of $C_h$ with different $S$.

73

ch = 100 [a1]

ch = 50 [a2]

ch = 200 [a3]

[b]
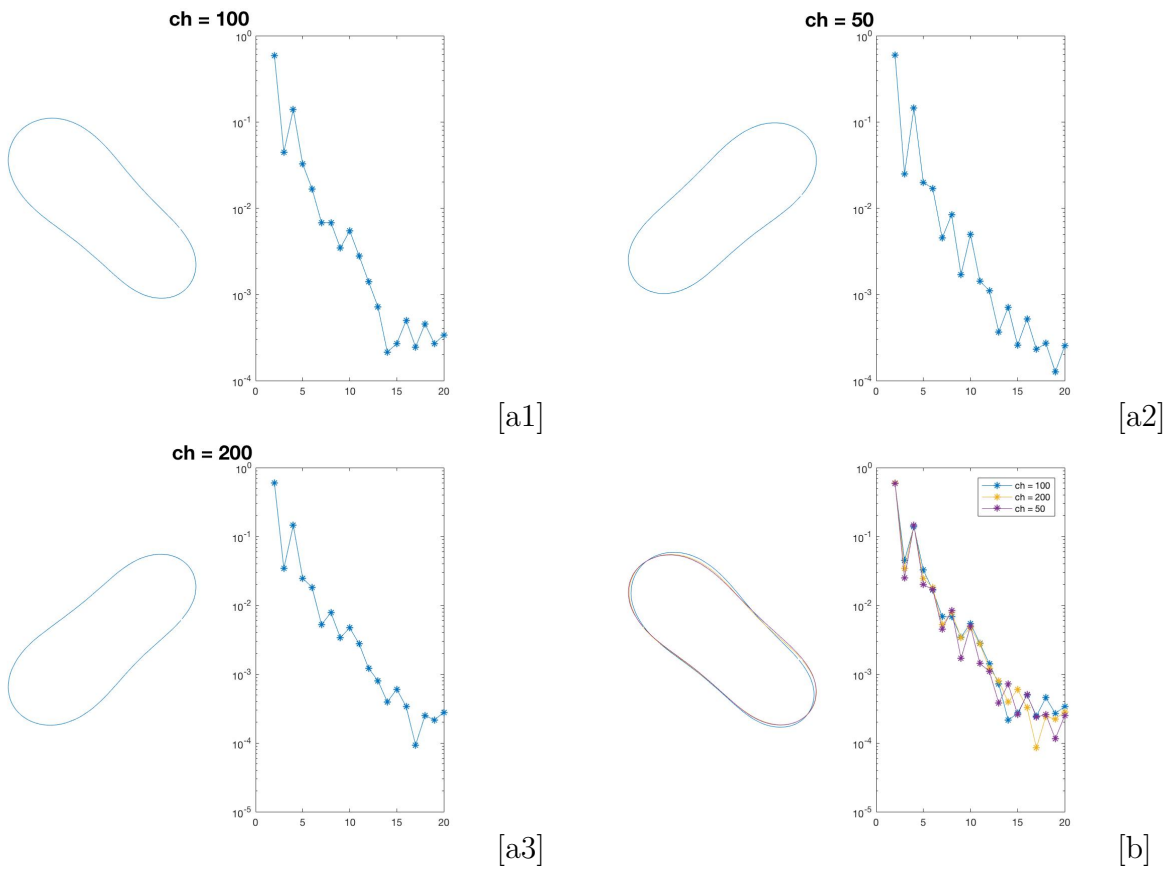
Figure 4.11: [a]The final shapes with different threshold. [b]Comparison at the same plot.

# Chapter 5

# Wrinkling Dynamics of Fluctuating Vesicles With Permeable Membrane

In this chapter, we focus on the microscopic vesicles with a permeable membrane, which is permeable to small particles in a fluid. We simulate the osmotic phenomenon relevant to the vesicles and extend the Stochastic Immersed Boundary Methods (SIBM) such that it is able to handle the permeability. We observe the vesicle shrinkage of a permeable vesicle in a viscous fluid with a high concentration difference.

## 5.1 Extension of Stochastic Immersed Boundary Methods (SIBM)

Consider a two-dimensional vesicle with a permeable membrane. The vesicle contains one viscous fluid inside and surrounded by another viscous fluid outside. Here we assume that the concentration of inside fluid is larger than the concentration of the outside fluid, i.e., $c_{in} < c_{out}$. This concentration difference causes an osmosis pressure and vesicle shrinking.

Because of the permeability of the membrane, the enclosed area of vesicles $A = A(t)$ is decreasing. We assume that the arclength of the vesicle is conserved.

In this section, we extend our method introduced in Chapter 2 such that it is able to capture the dynamics of mechanical structures that are permeable to the fluid [62]. Similar to Eq.(2.1), the stochastic time-dependent, incompressible Stokes equations are given by

$$\rho \frac{\partial \mathbf{u}}{\partial t}(\mathbf{x}, t) + \nabla p(\mathbf{x}, t) = \mu \Delta \mathbf{u}(\mathbf{x}, t) + \mathbf{f}_{\text{total}}(\mathbf{x}, t),$$
$$\nabla \cdot \mathbf{u}(\mathbf{x}, t) = 0, \tag{5.1}$$

where $\mathbf{f}_{\text{total}}(\mathbf{x}, t)$ is the total force density acting on the fluid arising from the immersed membrane and thermal fluctuations,

$$\mathbf{f}_{\text{total}}(\mathbf{x}, t) = \Lambda(\mathbf{F}_{\text{mem}}) + (\nabla_{\mathbf{x}} \cdot \Lambda) k_B T + \mathbf{f}_{\text{thm}}, \tag{5.2}$$

where $(\nabla_{\mathbf{x}} \cdot \Lambda) k_B T$ is a drift term coming from fluctuations of the immersed structure, which can be incorporated into the pressure, as it is a gradient. The force density $\mathbf{F}_{\text{mem}}$ is the variational derivative of the elastic energy function $\Phi[\mathbf{X}]$,

$$\mathbf{F}_{\text{mem}} = -\frac{\delta \Phi[\mathbf{X}]}{\delta \mathbf{X}}. \tag{5.3}$$

The equation of motion for the membrane is described as

$$\frac{\partial \mathbf{X}}{\partial t} = \Gamma \mathbf{u}(\mathbf{x}, t) + \psi (\mathbf{F}_{\text{mem}} + \mathbf{F}_{\text{thm}}), \tag{5.4}$$

where the second term is pressure-driven difference term due to the permeability [50, 21, 29, 62, 42], and $\psi$ denotes the permeability coefficient. Here we assume that the velocity difference has a linear relationship with the force density. The experimental estimate of $\psi$ is in the order $10^{-7} - 10^{-5} m^3/(N \cdot s)$[29, 42].

The free energy of the membrane is

$$\Phi[\mathbf{X}] = \Phi_{\text{bend}}[\mathbf{X}] + \Phi_{\text{tension}}[\mathbf{X}] + \Phi_{\text{osmosis}}[\mathbf{X}], \tag{5.5}$$

where $\Phi_{\text{bend}}[\mathbf{X}]$ is the bending energy, $\Phi_{\text{tension}}[\mathbf{X}]$ is elastic the energy defined in Eq. 2.9 and 2.10, and $\Phi_{\text{osmosis}}[\mathbf{X}]$ is the potential energy induced by the osmosis pressure.

Osmosis phenomenon is driven by a concentration difference of fluids inside and outside the membrane. It occurs in many biological systems and plays an important role [56, 44, 55, 7, 1, 61]. When diffusing particles are confined to a vesicle by a boundary which is permeable to fluid but less permeable to particles, a pressure difference develops between the inside and the outside of the vesicles. This pressure difference is called osmosis pressure.

van't Hoff describes the osmotic pressure difference $\Pi$ between two domains separated by a semi-permeable membrane as

$$\Pi = k_B T \Delta c, \tag{5.6}$$

where $k_B$ is the Boltzmann constant, $\Delta c = c_{out} - c_{in}$ is the concentration difference between domains separated by the semi-permeable barrier, and $T$ is the absolute temperature in degrees Kelvin.

Thus the osmosis force density is

$$\mathbf{F}_{\text{osmosis}} = k_B T \Delta c \tag{5.7}$$

An analytic estimation of the volume of the vesicle $V(t)$ is given in [24],

$$V(t) = V_0 \cdot \frac{c_{in,0}}{c_{out}} \cdot \left\{ 1 + \mathrm{L}\left[ \frac{c_\Delta}{c_{in,0}} \cdot \exp\left( \frac{c_\Delta}{c_{in,0}} - \frac{A \cdot \psi \cdot V_w \cdot c_{out}^2}{V_0 \cdot c_{in,0}} \cdot t \right) \right] \right\}, \tag{5.8}$$

where $V_w, V_0, A, c_{\text{in},0}$ and $c_{\text{out}}$ are the molar volume of water, initial vesicle volume, the constant surface area of the vesicle, the initial concentration inside the vesicles, and concentration in the external solution at time zero, respectively.

Applying Eq. 5.8[47], we have

$$\Delta c \sim \frac{d(V(t))}{dt} \sim \exp(-kt), \tag{5.9}$$

where $k$ is constant which linearly depends on the permeability coefficient $\psi$. So we estimate $\mathbf{F}_{\text{osmosis}}$ as a normal vector with the magnitude as an exponential decay function

$$F_{\text{osmosis}}(t) = F_0 \exp(-k \cdot t), \tag{5.10}$$

where $F_0 = k_B T \Delta c(0)$, $k = k_0 \cdot \psi$ is a constant depending on permeability coefficient $\psi$, and $k_0$ is the decay rate.

## 5.2  Wrinkling Dynamics in the Quiescent Fluid

Firstly we study the dynamics when a quasi-circular vesicle is immersed in a quiescent fluid with higher outside fluid concentration. The wrinkling dynamics of the vesicle in deterministic and stochastic simulations are displayed in Figure 5.1[a] and [b], respectively. The initial shape of the vesicle is an ellipse with excess arc length $\Delta = 0.058$. The permeability coefficient is $\psi = 5 \times 10^{-6} m^3/(N \cdot s)$. Due to the high osmosis pressure and the permeability of the membrane, the enclosed area $A(t)$ decreases exponentially to constants (see Figure 5.1[d]) and the vesicle shrinks. High-order Fourier modes are excited. As the concentration difference decreases to 0, the osmosis pressure $F_{\text{osmosis}}$ decays to 0 and the wrinkles are smoothed out and the vesicle releases to its equilibrium shape.
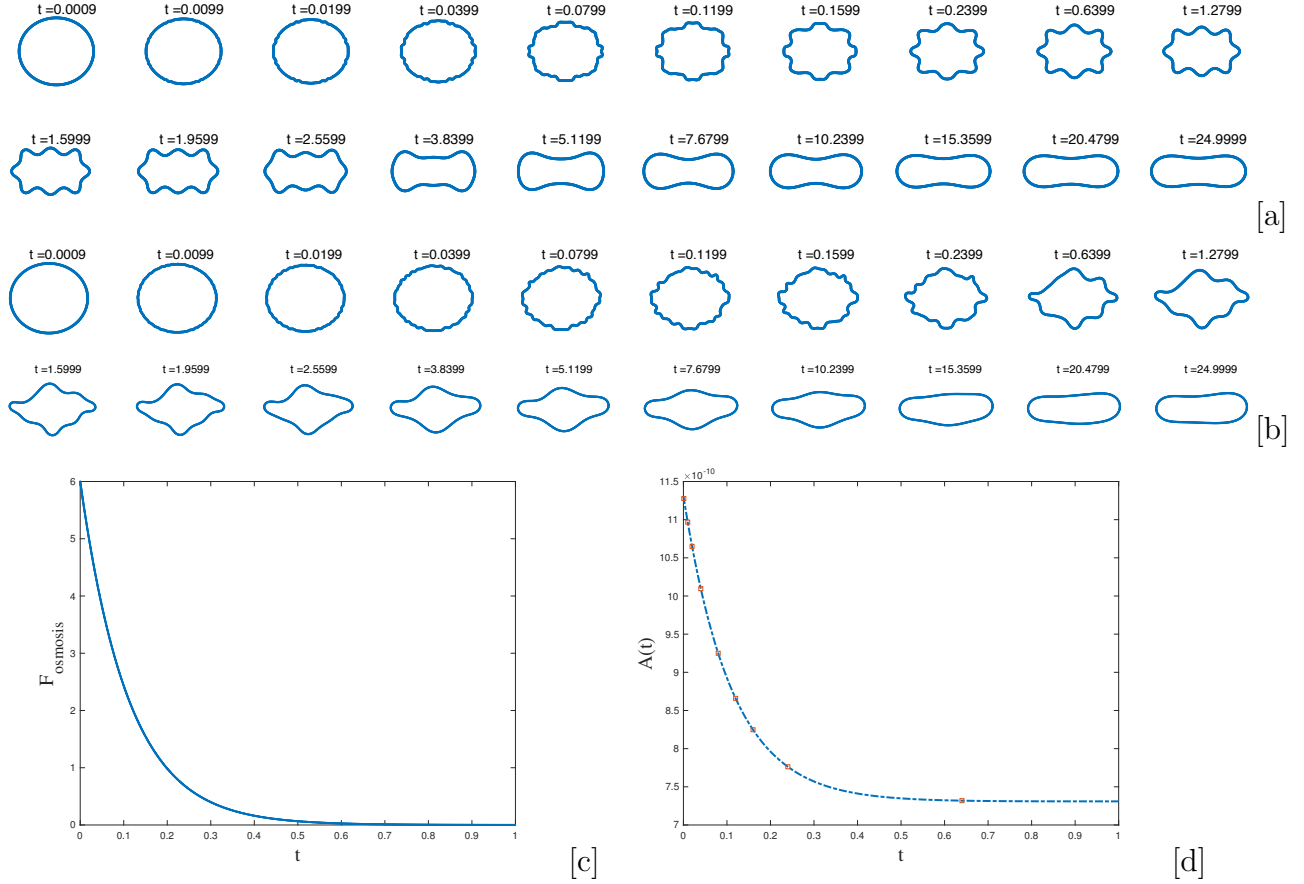
Figure 5.1: Dynamics of a quasi-circular vesicle in quiescent fluid. [a] Deterministic dynamics. [b] Dtochastic dynamics. [c]Magnitude of osmosis force $F_{\text{osmosis}}$. [d]Evolution of area versus time.

## 5.3 Nonlinear Dynamics in Time-dependent Viscous Flow

Secondly, we consider a vesicle is immersed in a viscous fluid with the extensional flow. At $t' = 1$, the direction of flow is suddenly reversed. The initial shape of the vesicle is an ellipse with aspect ratio $a : b = 1 : 0.8$. Here we set permeable coefficient $\psi = 1 \times 10^{-6} m^3/(pN \cdot s)$, the extensional flow rate $S = 4$, the bending stiffness $\kappa = 10^{-19} J$.

### 5.3.1  Wrinkling Dynamics

Wrinkling dynamics of the vesicles in deterministic and stochastic realizations are shown in Figure 5.2[a][b], respectively (upper: impermeable vesicle, bottom: permeable vesicle). Due to the osmosis pressure and permeability, the vesicle with a permeable membrane is shrinking, and more clear wrinkles are excited. At the same time, they postpone the disappearance of the wrinkles and extend the process. At $t' = 1.38$s, the impermeable vesicles are in their equilibrium shapes, while there still are some wrinkles on the permeable vesicles. Figure 5.2 [c] presents a shape comparison between impermeable and permeable vesicles (left: deterministic, right: stochastic). The permeability and nonzero $F_{\text{osmosis}}$, caused by the concentration difference, lead to the vesicle shrinkage. The areas of permeable vesicles are smaller than the ones for impermeable vesicles, and the wrinkles on the permeable vesicles are much easier to observe.

### 5.3.2  Dependence of Wrinkling on the Permeability Coefficient $\psi$

Next, we investigate the dependence of the wrinkling characteristics as a function of the permeability coefficient $\psi$ for a range of flow strength $S$. The results are presented in Figure. 5.3.

In both deterministic (Figure 5.3a(left)) and stochastic (Figure 5.3a(right)), the dominant mode $m^*$ increases as the flow strength increases. As $\psi$ increases, the variability in $m^*$ tends to decrease. This indicates that the interactions between flow strength and permeability can attenuate the variability of wrinkling dynamics. As $S$ and $\psi$ increase, the dominant modes in the deterministic and stochastic cases converge to 4th mode.

Figure 5.3[b] and [c] show the corresponding vesicle morphologies (top: deterministic, bottom: stochastic) at the nondimensional times $t'^*$ using $\psi = 10^{-8} m^2/(N \cdot s)$ in Figure 5.3[b]
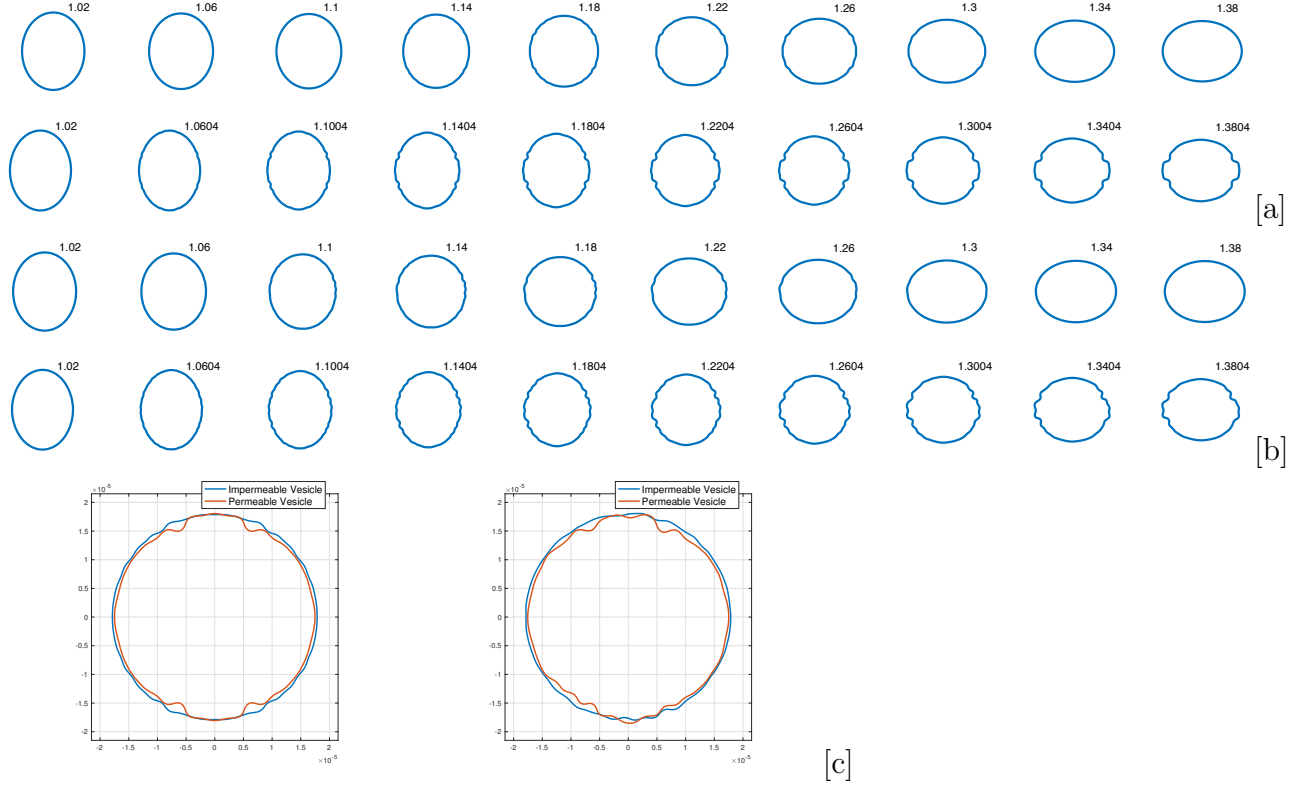
Figure 5.2: Wrinkling dynamics of a quasi-circular vesicle. [a] Deterministic dynamics of the impermeable and permeable vesicles. [b] Stochastic dynamics of the permeable and impermeable vesicles. (upper : impermeable vesicle, bottom : permeable vesicle) [c] Morphologies comparison (blue : impermeable, right : permeable).

and $\psi = 5 \times 10^{-6} m^2/(N \cdot s)$ in Figure 5.3[c].

### 5.3.3 Dependence of Wrinkling on the Initial Osmosis Pressure $F_p$

Here we study the dependence of the wrinkling characteristics as a function of the initial osmosis pressure $F_p$ and flow strength S. Figure 5.4[a], (deterministic (left) and stochastic (right)), shows that as $F_p$ increases, the dominate mode $m^*$ converge. For a fixed small osmosis force (e.g., $F_p = 2$), the dominate mode increases as the flow strength $S$ increases, which is consistent with the results for impermeable vesicles [38]. However, when the osmosis force is strong enough, it dominates the wrinkles, and the corresponding morphologies are

81

controlled by 4th mode.

## 5.3.4 Quasi-circular Approximation

The vesicle membrane is parametrized by $\mathbf{X}(t, \phi) : r = R(t)(1+p)$, where $R(t)$ is the effective radius defined as $R(t) = \sqrt{\frac{A(t)}{\pi}}$, and a small perturbation function $p$ is expanded in Fourier harmonics :

$$p(t, \phi) = \sum_{-\infty}^{+\infty} p_m \frac{\exp(im\phi)}{\sqrt{2\pi}}, \tag{5.11}$$

here $m$ is the perturbation mode, and $p_m(t) \ll 1$ is the perturbation amplitude of mode $m$.

We only keep up to the quadratic order terms, and neglect all higher order terms of $p_m$ in the following analysis.

The enclose area $A(t)$ is

$$A(t) = \pi R^2 \left(1 + \frac{2p_0}{\sqrt{2\pi}} + \frac{1}{2\pi} \sum_{m\neq 0} |p_m|^2\right). \tag{5.12}$$

The arclength is

$$L = 2\pi R \left(1 + \frac{1}{4\pi} \sum_{m\neq 0} (m^2 - 1) |p_m|^2\right) + O\left(p^3\right), \tag{5.13}$$

where $R = R(t)$. The force density acting on the membrane is given by

$$\mathbf{F} = \left(\kappa H_{ss} + \frac{\kappa}{2} H^3 - H\sigma + F_p\right) \mathbf{n} + \sigma_s \mathbf{t} \tag{5.14}$$

where $F_p$ is the magnitude of the osmosis pressure applied on the membrane. The magnitude

of **F** in the normal and tangent direction in Fourier harmonics are given by,

$$F_{\mathbf{n}} = \frac{\kappa}{R^3} \left[ \left( \frac{1}{2} + F_p + \sigma_0 \right) - \sum_{m \neq 0} \left[ (m^2 - 1)(m^2 - \frac{3}{2} + \sigma_0)p_m + \sigma_m \right] \frac{\exp(im\phi)}{\sqrt{2\pi}} \right],$$

(5.15)

$$F_{\mathbf{t}} = \frac{\kappa}{R^3} \sum_{m \neq 0} im\sigma_m \frac{\exp(im\phi)}{\sqrt{2\pi}}.$$

(5.16)

By solving the Stokes equation with boundary conditions, we have the induced velocity along the normal direction

$$v_m = -\frac{\kappa}{2R^2} \beta_m E_m p_m$$

(5.17)

where $v_m$ is the $m$-th Fourier mode of the induced velocity, $E_m = (m^2 - 1)\left(m^2 - \frac{3}{2} + \sigma_0\right)$ is elasticity coefficient and $\beta_m = \frac{|m|}{2(1+\lambda)(m^2-1)}$ is the mobility coefficient.

The external applied velocity field is

$$u_r^\infty(r, \phi) = \frac{S(t)r\cos 2\phi}{\sqrt{2\pi}}, \qquad u_\phi^\infty(r, \phi) = \frac{S(t)r\sin 2\phi}{\sqrt{2\pi}}$$

(5.18)

where $S(t) = -S\,\mathrm{sign}(t - t_0)$ indicates that the direction of the flow is reversed at $t = t_0$, $\bar{S}$ is the strength of the applied elongational flow.

Plugging (5.15) - (5.17) to the equation of motion for the membrane (5.4), we have the equation of motion for the amplitude of mode m

$$\frac{dp_m}{dt} = \bar{S}(t)\left(\delta_{m,2} + \delta_{m,-2}\right) - \left( \frac{R'}{R} + \frac{\kappa}{\eta_2 R^3}\beta_m E_m + \frac{\kappa\psi}{R^3}E_m \right) p_m, \quad \text{for } |m| > 0, t \geq 0 \quad (5.19)$$

$$\frac{dp_m}{dt} = \bar{S}(t) \left( \delta_{m,2} + \delta_{m,-2} \right) - \left( \frac{R'}{R} + A_m \sigma_0 + B_m \right) p_m, \quad \text{for } |m| > 0, t \geq 0 \tag{5.20}$$

where $A_m = am + b(m^2 - 1)$, $B_m = A_m(m^2 - \frac{3}{2})$, and $a = \frac{\kappa}{2R^3 \eta(1+\lambda)}$, $b = \frac{\kappa\psi}{R^3}$.

For $m = 0$

$$R' = \frac{\kappa\psi}{R^2} + \psi F_p + \frac{\kappa\psi}{R^2} \sigma_0. \tag{5.21}$$

Together with the arc length conservation (5.13)

$$d_t L = d_t \left( 2\pi R \left( 1 + \frac{1}{4\pi} \sum_{m \neq 0} (m^2 - 1) |p_m|^2 \right) \right) = 0 \tag{5.22}$$

Note that $R = R(t)$ is a function of time t. We have

$$\sigma = \frac{6S(t) Re(p_2) - \bar{\Gamma}}{\bar{A}} \tag{5.23}$$

where $\bar{A} = \sum_{m \neq 0} m^2 (A_m - b) |p_m|^2$, $\bar{\Gamma} = \sum_{m \neq 0} B_m |p_m|^2$

As we focus on the contribution of the thermal fluctuation, a stochastic force needs to be added to the force equation. Let $\xi_m(t)$ be the m-th mode of the stochastic force, then the equation of motion (5.24) becomes

$$\frac{dp_m}{dt} = \underbrace{\bar{S}(t) \left( \delta_{m,2} + \delta_{m,-2} \right)}_{\text{External flow}} - \underbrace{\left( \frac{R'}{R} + A_m \sigma_0 + B_m \right) p_m}_{\text{Elastic force}} + \underbrace{\xi_m}_{\text{Thermal noise}}, \tag{5.24}$$

where $A_m = am + b(m^2 - 1)$, $B_m = A_m(m^2 - \frac{3}{2})$, and $a = \frac{\kappa}{2R^3 \eta(1+\lambda)}$, $b = \frac{\kappa\psi}{R^3}$.

84

## Numerical Results

We solve the equation system of the motion and the surface tension constraint numerically. We set parameters $\kappa = 10^{-19}$J, $\eta_2 = 10^{-3}$Pa$\cdot$s which is the viscosity of water at temperature 293K, $\lambda = 1$, $R_0 = 2 \times 10^{-5}$m, the elongation rate $S = 4$, and the permeable coefficient $\psi = 1 \times 10^{-6} m^3/(N \cdot s)$, the time step $\Delta t = 10^{-6}s$.

Figure 5.5 compares the magnitudes of the $2^{\text{nd}}$ Fourier mode $|p_2|$ and dominant mode $|p_{12}|$ in linear and nonlinear simulations. The linear results capture the fact that $|p_2|$ keeps growing and exceed its initial value for the permeable vesicle (see Figure 3.4 for a comparison with impermeable vesicles). However, $|p_{12}|$ in the linear results doesn't increases again after it reaches its minimum, which is the dynamics of $|p_{12}|$ in the nonlinear simulation.

In this chapter, we applied an extended version of SIBM to investigate the wrinkling dynamics of a permeable vesicle in a quiescent fluid and in the fluid with time-varying flow. Due to the concentration difference, an osmotic pressure is applied on the membrane and generates wrinkles. Then we studied the effects of the permeability coefficient $\psi$ and initial osmotic pressure $F_p$. As $\psi$ increases, the vesicle shrinks faster and clearer wrinkles are shown on the membrane. The dominant mode $m^*$ converges to 4th mode for large $F_p$.
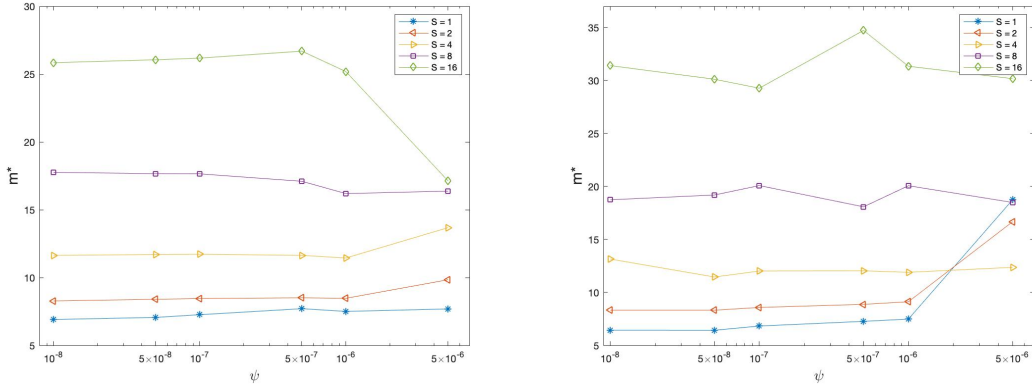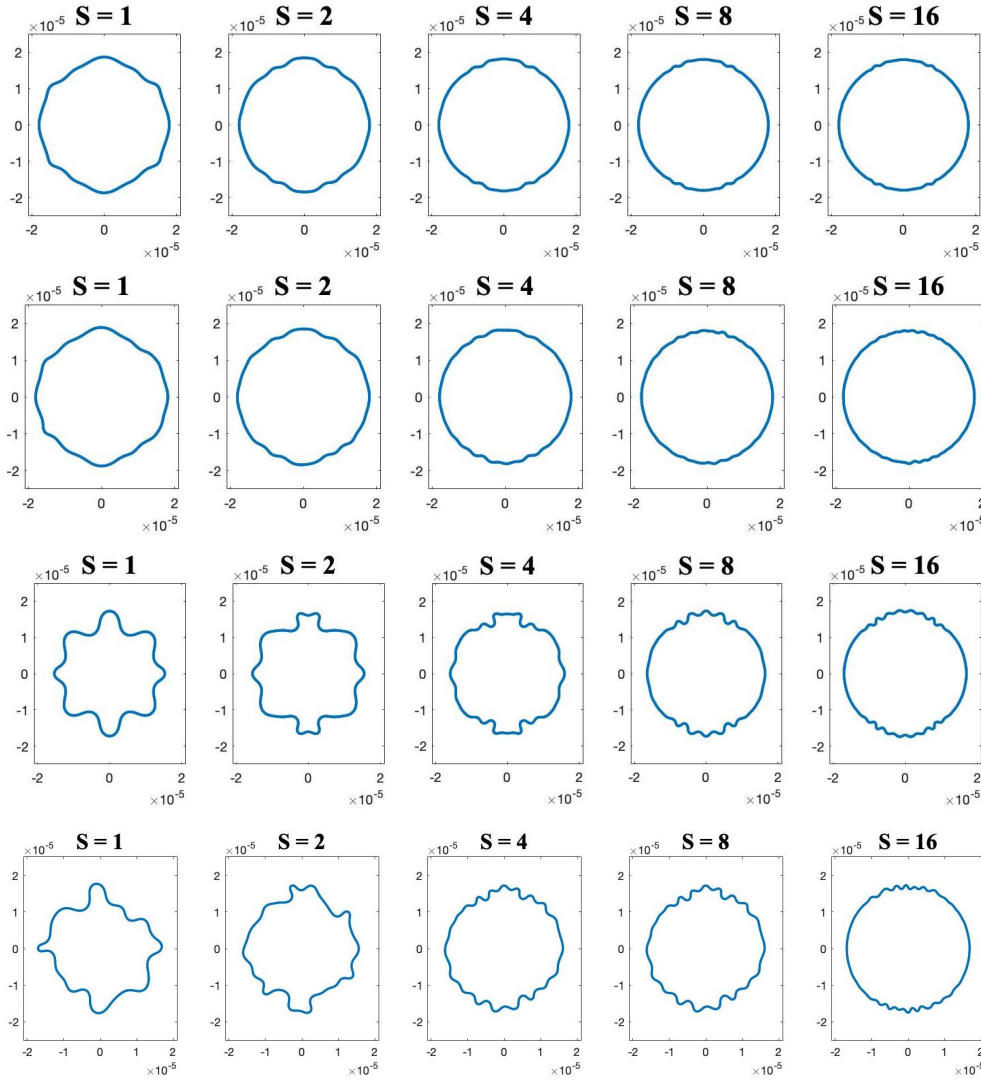
Figure 5.3: Wrinkling characteristics as a function of the membrane permeability coefficient $\psi$ and flow strength S. [a]The relation between the most dominant mode $m*$ and the membrane permeability coefficient $\psi$ at a fixed flow strength S as labeled.[b-c] The vesicle shapes from the deterministic (upper) and stochastic (lower) immersed boundary methods for different flow strength S and membrane permeability coefficients $\psi$, as labeled.
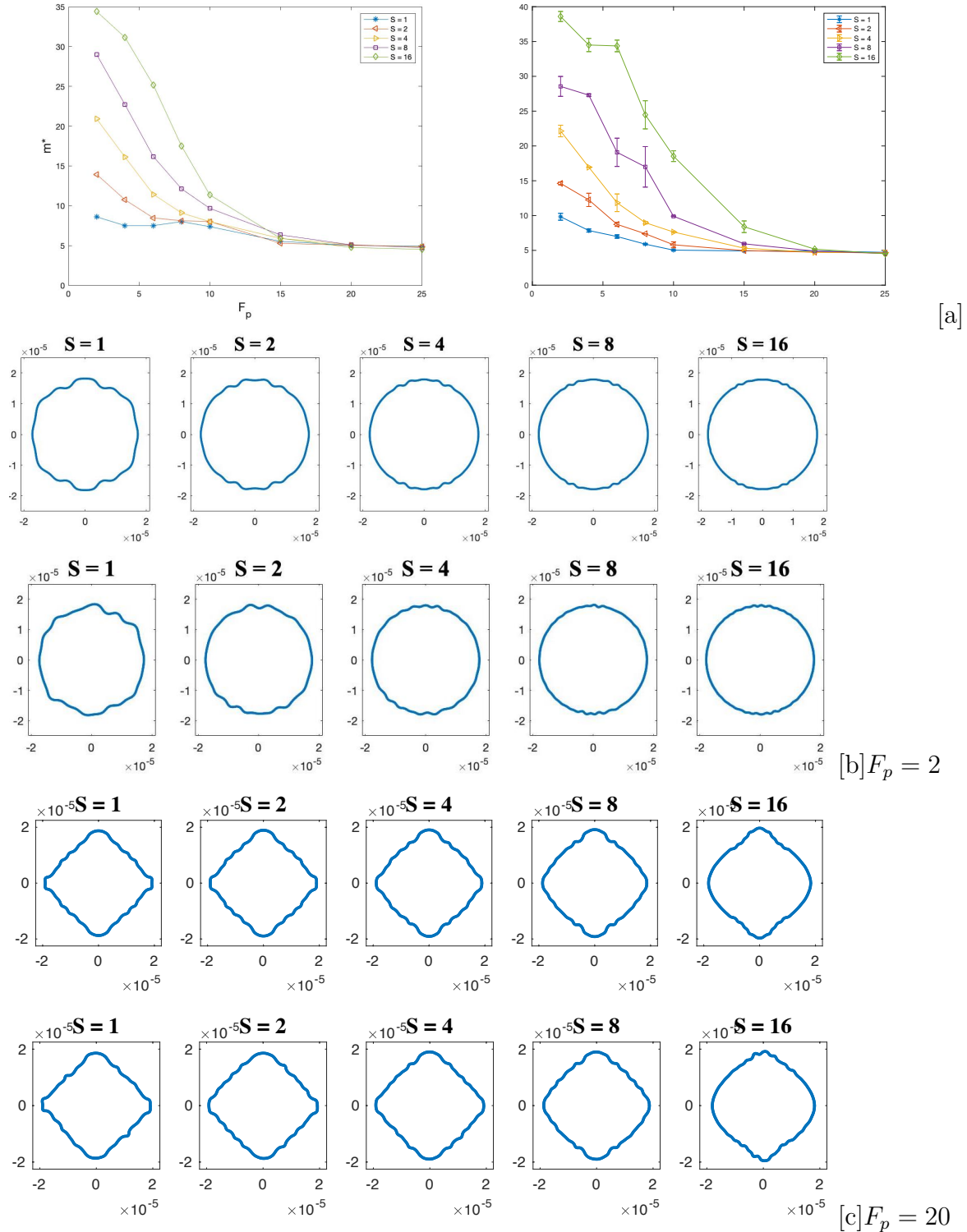
Figure 5.4: Wrinkling characteristics as a function of the initial osmosis pressure $F_p$ and flow strength S. [a]The relation between the most dominant mode m* and the initial osmosis pressure $F_p$ at a fixed flow strength S as labeled. (left: deterministic, right : stochastic) [b-c] The vesicle shapes from the deterministic (upper) and stochastic (lower) immersed boundary methods for different flow strength S and initial osmosis pressure $F_p$, as labeled.
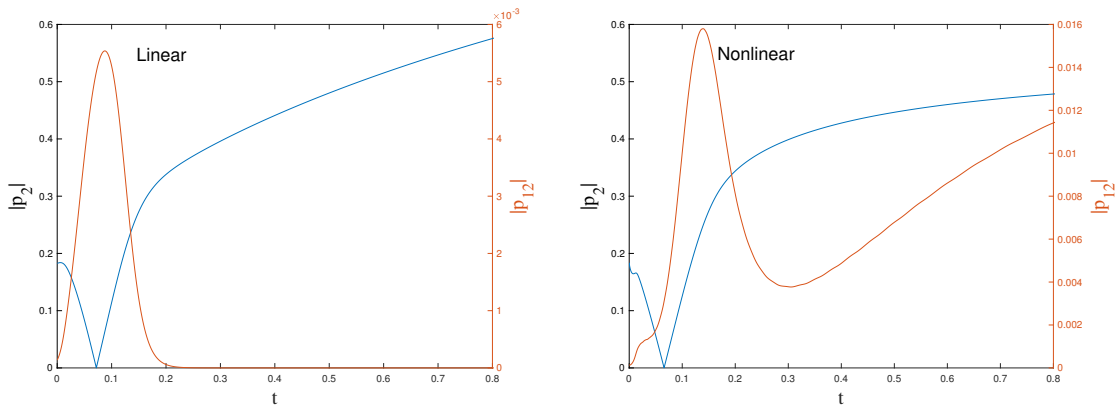
Figure 5.5: Fourier modes $|p_2|$ and $|p_{11}|$ (left: linear, right: nonlinear).

# Chapter 6

# Summary And Future Work

## 6.1   Summary

We explored the two-dimensional fully nonlinear dynamics of vesicles in a viscous fluid at finite temperature. Numerically we applied a stochastic immersed boundary method with a biophysically motivated choice of thermal fluctuations. Analytically we developed a two-dimensional linear theory for the wrinkling dynamics of a quasi-circular vesicle. The numerical results and analytical approach in this thesis are expected to lead a better understanding of related problems in biology.

We first developed a two-dimensional stochastic immersed boundary method and chose the 2D thermal fluctuations by matching the numerical results with a theoretical solution for a fluctuating filament. We discovered a quadratic relationship between the side length of the computational domain and the spatial scale, and explained the relationship analytically. Therefore, our studies can provide a bridge between two-dimensional and three-dimensional thermal fluctuations.

Secondly, we investigated the long-term dynamics of impermeable vesicles in a periodically reversed flow numerically.Our numerical results show that there are three stages in the dynamics. At the first stage, the negative surface tension generate high-order wrinkles on the vesicle boundary. At the second stage, the high-order wrinkles disappear and some low-frequency modes, like $p_3$, $p_4$ dominate the shape of the vesicle. As time increases, all the wrinkles are smoothed out and the second mode $p_2$ dominates again. Then we performed a two-dimensional linear theory of a quasi-circular vesicle. We derived and solved the equation system describing the motion of the membrane interface numerically. Our analytical results also indicated these three stages. This agreement between nonlinear and linear simulations can provide insight into the experiments.

Finally, we studied vesicles with permeable membranes. We extended the two-dimensional stochastic immersed boundary method and asymptotic approach such that both work for permeable membranes.We observed the vesicle shrinkage in a quiescent fluid where the inside fluid has a lower concentration than the outside fluid. The osmosis pressure activates wrinkles. As the enclosed area decreases exponentially, the shapes of the vesicle finally evolve to its equilibrium shape. Next, we compared the wrinkling dynamics of the permeable and impermeable vesicles in one-reverse flow. We observed more clear wrinkles on permeable membranes, and a slower disappearance of the wrinkles. The solutions of the linear theory agree with the corresponding solutions from the nonlinear simulation. Thus, our nonlinear results can bring us an expectation of the dynamics of the vesicle with a permeable membrane.

## 6.2   Future Work

In this thesis, we apply a two-dimensional SIBM, and results in 3D could be different. We plan to explore a three-dimensional SIBM to investigate the dynamics of the fluctuation

vesicles. However, there are many challenges.

The major challenge is the high computational cost. In 2D, we use the parallel computing techniques to optimize the models and reduce the computational time by 80%. While in 3D, we don't have an appropriate way to apply the parallel computing techniques. So it's almost impossible to investigate the long-term dynamics.

Another challenge is the complicated discretization of the membrane surface and calculation of the force density. For example, in 2D model, two neighboring nodes on the membrane connected by elastic springs and the tension between them is given by (See Appendix A.2 and [38] for details),

$$\mathbf{F}_{[i]} = \lambda_L \left( \Delta s_{i,i+1} - \Delta L \right) \mathbf{v}.$$

Here $\mathbf{v}$ is a unit vector acting on the i-th node pointing to the (i+1)-th node, $\lambda_L$ is the spring constant and $(\Delta s_{i,i+1} - \Delta L)$ is the distance changed between these two nodes. However, in $3D$, the surface tension is much more complex. A simple 3D model and the corresponding surface tensions at $p_1, p_2, p_3$ are shown in Figure 6.1.



$$(f_{x_1}, f_{y_1}, f_{z_1}) = \alpha \left( \vec{\xi} \times \vec{a}_{32} \right),$$
$$(f_{x_2}, f_{y_2}, f_{z_2}) = \alpha \left( \vec{\xi} \times \vec{a}_{13} \right),$$
$$(f_{x_3}, f_{y_3}, f_{z_3}) = \alpha \left( \vec{\xi} \times \vec{a}_{21} \right).$$
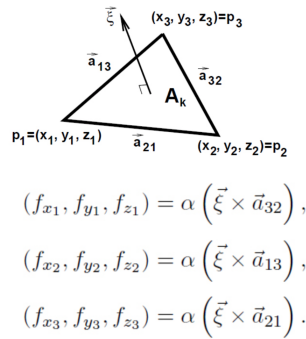
Figure 6.1: A schematic diagram of a surface tension model in 3D

Besides, the perturbation theory for a quasispherical vesicle is also more difficult than the 2D linear theory.

# Bibliography

[1] B. Alberts, A. Johnson, J. Lewis, M. Raff, K. Roberts, P. Walter, D. Bray, and J. Watson. The theory of measurement of osmotic pressure. new york: Garland science; 2002.

[2] B. Alberts, J. Wilson, and T. Hunt. Molecular biology of the cell (garland science, new york). *USA. 1601p*, 2008.

[3] T. M. Allen and P. R. Cullis. Drug delivery systems: entering the mainstream. *Science*, 303(5665):1818–1822, 2004.

[4] S. E. Andaloussi, I. Mäger, X. O. Breakefield, and M. J. Wood. Extracellular vesicles: biology and emerging therapeutic opportunities. *Nature reviews Drug discovery*, 12(5):347, 2013.

[5] P. J. Atzberger. A note on the correspondence of an immersed boundary method incorporating thermal fluctuations with stokesian–brownian dynamics. *Physica D: Nonlinear Phenomena*, 226(2):144–150, 2007.

[6] P. J. Atzberger. Stochastic eulerian lagrangian methods for fluid–structure interactions with thermal fluctuations. *Journal of Computational Physics*, 230(8):2821–2837, 2011.

[7] P. J. Atzberger, S. Isaacson, and C. S. Peskin. A microfluidic pumping mechanism driven by non-equilibrium osmotic effects. *Physica D: Nonlinear Phenomena*, 238(14):1168–1179, 2009.

[8] P. J. Atzberger, P. R. Kramer, and C. S. Peskin. A stochastic immersed boundary method for fluid-structure dynamics at microscopic length scales. *Journal of Computational Physics*, 224(2):1255–1292, 2007.

[9] F. Balboa, J. B. Bell, R. Delgado-Buscalioni, A. Donev, T. G. Fai, B. E. Griffith, and C. S. Peskin. Staggered schemes for fluctuating hydrodynamics. *Multiscale Modeling & Simulation*, 10(4):1369–1408, 2012.

[10] T. Biben, K. Kassner, and C. Misbah. Phase-field approach to three-dimensional vesicle dynamics. *Physical Review E*, 72(4):041921, 2005.

[11] D. Boal and D. H. Boal. *Mechanics of the Cell*. Cambridge University Press, 2012.

[12] P. B. Canham. The minimum energy of bending as a possible explanation of the biconcave shape of the human red blood cell. *Journal of theoretical biology*, 26(1):61–81, 1970.

[13] G.-H. Cottet and E. Maitre. A level-set formulation of immersed boundary methods for fluid–structure interaction problems. *Comptes Rendus Mathematique*, 338(7):581–586, 2004.

[14] G.-H. Cottet and E. Maitre. A level set method for fluid-structure interactions with immersed surfaces. *Mathematical models and methods in applied sciences*, 16(03):415–438, 2006.

[15] J. M. O. De Zarate and J. V. Sengers. *Hydrodynamic fluctuations in fluids and fluid mixtures*. Elsevier, 2006.

[16] J. Deschamps, V. Kantsler, and V. Steinberg. Phase diagram of single vesicle dynamical states in shear flow. *Physical review letters*, 102(11):118105, 2009.

[17] R. Dimova, K. A. Riske, S. Aranda, N. Bezlyepkina, R. L. Knorr, and R. Lipowsky. Giant vesicles in electric fields. *Soft matter*, 3(7):817–827, 2007.

[18] Q. Du and M. Li. On the stochastic immersed boundary method with an implicit interface formulation. *preprint*, 2009.

[19] R. Finken, A. Lamura, U. Seifert, and G. Gompper. Two-dimensional fluctuating vesicles in linear shear flow. *The European Physical Journal E*, 25(3):309–321, 2008.

[20] G. Gompper and M. Schiek. Lipid bilayers and red blood cells. Soft Matter: Volume 4, 2008.

[21] N. Gov, A. Zilman, and S. Safran. Hydrodynamics of confined membranes. *Physical Review E*, 70(1):011104, 2004.

[22] G. Gregoriadis. Engineering liposomes for drug delivery: progress and problems. *Trends in biotechnology*, 13(12):527–537, 1995.

[23] B. E. Griffith and C. S. Peskin. On the order of accuracy of the immersed boundary method: Higher order convergence rates for sufficiently smooth problems. *Journal of Computational Physics*, 208(1):75–105, 2005.

[24] C. Hannesschläger, T. Barta, C. Siligan, and A. Horner. Quantification of water flux in vesicular systems. *Scientific reports*, 8(1):8516, 2018.

[25] W. Helfrich. Elastic properties of lipid bilayers: theory and possible experiments. *Zeitschrift für Naturforschung C*, 28(11-12):693–703, 1973.

[26] T. Y. Hou, Z. Li, S. Osher, and H. Zhao. A hybrid method for moving interface problems with application to the hele–shaw flow. *Journal of Computational Physics*, 134(2):236–252, 1997.

[27] V. Kantsler, E. Segre, and V. Steinberg. Vesicle dynamics in time-dependent elongation flow: Wrinkling instability. *Physical review letters*, 99(17):178102, 2007.

[28] M. Karlsson, M. Davidson, R. Karlsson, A. Karlsson, J. Bergenholtz, Z. Konkoli, A. Jesorka, T. Lobovkina, J. Hurtig, M. Voinova, et al. Biomimetic nanoscale reactors and networks. *Annu. Rev. Phys. Chem.*, 55:613–649, 2004.

[29] K. Keren, P. T. Yam, A. Kinkhabwala, A. Mogilner, and J. A. Theriot. Intracellular fluid flow in rapidly moving cells. *Nature cell biology*, 11(10):1219, 2009.

[30] Y. Kim and M.-C. Lai. Simulating the dynamics of inextensible vesicles by the penalty immersed boundary method. *Journal of Computational Physics*, 229(12):4840–4853, 2010.

[31] P. Kramer and C. Peskin. Incorporating thermal fluctuations into the immersed boundary method. In *Computational Fluid and Solid Mechanics 2003*, pages 1755–1758. Elsevier, 2003.

[32] R. Kubo. The fluctuation-dissipation theorem. *Reports on progress in physics*, 29(1):255, 1966.

[33] V. Lebedev, K. Turitsyn, and S. Vergeles. Dynamics of nearly spherical vesicles in an external flow. *Physical review letters*, 99(21):218101, 2007.

[34] S. Leung, J. Lowengrub, and H. Zhao. A grid based particle method for solving partial differential equations on evolving surfaces and modeling high order geometrical motion. *Journal of Computational Physics*, 230(7):2540–2561, 2011.

[35] M. Levant, D. Abreu, U. Seifert, and V. Steinberg. Wrinkling instability of vesicles in steady linear flow. *EPL (Europhysics Letters)*, 107(2):28001, 2014.

[36] R. Lipowsky. The conformation of membranes. *Nature*, 349(6309):475, 1991.

[37] R. Lipowsky and E. Sackmann. *Structure and dynamics of membranes: I. from cells to vesicles/II. generic and specific interactions.* Elsevier, 1995.

[38] K. Liu, C. Hamilton, J. Allard, J. Lowengrub, and S. Li. Wrinkling dynamics of fluctuating vesicles in time-dependent viscous flow. *Soft matter*, 12(26):5663–5675, 2016.

[39] K. Liu and S. Li. Nonlinear simulations of vesicle wrinkling. *Mathematical Methods in the Applied Sciences*, 37(8):1093–1112, 2014.

[40] E. Maitre, T. Milcent, G.-H. Cottet, A. Raoult, and Y. Usson. Applications of level set methods in computational biophysics. *Mathematical and Computer Modelling*, 49(11-12):2161–2169, 2009.

[41] S. Meßlinger, B. Schmidt, H. Noguchi, and G. Gompper. Dynamical regimes and hydrodynamic lift of viscous vesicles under shear. *Physical Review E*, 80(1):011901, 2009.

[42] A. Mogilner and A. Manhart. Intracellular fluid mechanics: Coupling cytoplasmic flow with active cytoskeletal gel. *Annual Review of Fluid Mechanics*, 50:347–370, 2018.

[43] H. Naito, M. Okuda, and O.-Y. Zhong-Can. Counterexample to some shape equations for axisymmetric vesicles. *Physical Review E*, 48(3):2304, 1993.

[44] J. Nardi, R. Bruinsma, and E. Sackmann. Vesicles as osmotic motors. *Physical Review Letters*, 82(25):5168, 1999.

[45] V. Noireaux and A. Libchaber. A vesicle bioreactor as a step toward an artificial cell assembly. *Proceedings of the National Academy of Sciences*, 101(51):17669–17674, 2004.

[46] T. Odijk. Stiff chains and filaments under tension. *Macromolecules*, 28(20):7016–7018, 1995.

[47] K. Oglecka, P. Rangamani, B. Liedberg, R. S. Kraut, and A. N. Parikh. Oscillatory phase separation in giant lipid vesicles induced by transmembrane osmotic differentials. *Elife*, 3:e03695, 2014.

[48] R. G. Parr. Density functional theory of atoms and molecules. In *Horizons of Quantum Chemistry*, pages 5–15. Springer, 1980.

[49] C. S. Peskin. The immersed boundary method. *Acta numerica*, 11:479–517, 2002.

[50] J. Prost, J.-B. Manneville, and R. Bruinsma. Fluctuation-magnification of non-equilibrium membranes near a wall. *The European Physical Journal B-Condensed Matter and Complex Systems*, 1(4):465–480, 1998.

[51] L. E. Reichl. A modern course in statistical physics, 1999.

[52] U. Seifert. Fluid membranes in hydrodynamic flow fields: Formalism and an application to fluctuating quasispherical vesicles in shear flow. *The European Physical Journal B-Condensed Matter and Complex Systems*, 8(3):405–415, 1999.

[53] J. Sohn, S. Li, X. Li, and J. S. Lowengrub. Axisymmetric multicomponent vesicles: A comparison of hydrodynamic and geometric models. *International journal for numerical methods in biomedical engineering*, 28(3):346–368, 2012.

[54] J. S. Sohn, Y.-H. Tseng, S. Li, A. Voigt, and J. S. Lowengrub. Dynamics of multicomponent vesicles in a viscous fluid. *Journal of Computational Physics*, 229(1):119–144, 2010.

[55] T. M. Squires and S. R. Quake. Microfluidics: Fluid physics at the nanoliter scale. *Reviews of modern physics*, 77(3):977, 2005.

[56] A. Staverman. The theory of measurement of osmotic pressure. *Recueil des Travaux Chimiques des Pays-Bas*, 70(4):344–352, 1951.

[57] K. Turitsyn and S. Vergeles. Wrinkling of vesicles during transient dynamics in elongational flow. *Physical review letters*, 100(2):028103, 2008.

[58] M. Uhlmann. An immersed boundary method with direct forcing for the simulation of particulate flows. *Journal of Computational Physics*, 209(2):448–476, 2005.

[59] S. K. Veerapaneni, D. Gueyffier, G. Biros, and D. Zorin. A numerical method for simulating the dynamics of 3d axisymmetric vesicles suspended in viscous flows. *Journal of Computational Physics*, 228(19):7233–7249, 2009.

[60] S. K. Veerapaneni, D. Gueyffier, D. Zorin, and G. Biros. A boundary integral method for simulating the dynamics of inextensible vesicles suspended in a viscous fluid in 2d. *Journal of Computational Physics*, 228(7):2334–2353, 2009.

[61] D. Voet, J. G. Voet, and C. W. Pratt. *Fundamentals of biochemistry: life at the molecular level.* Number 577.1 VOE. 2013.

[62] C.-H. Wu, T. G. Fai, P. J. Atzberger, and C. S. Peskin. Simulation of osmotic swelling by the stochastic immersed boundary method. *SIAM Journal on Scientific Computing*, 37(4):B660–B688, 2015.

[63] J.-J. Xu, Z. Li, J. Lowengrub, and H. Zhao. A level-set method for interfacial flows with surfactant. *Journal of Computational Physics*, 212(2):590–616, 2006.

[64] O.-Y. Zhong-Can and W. Helfrich. Instability and deformation of a spherical vesicle by pressure. *Physical review letters*, 59(21):2486, 1987.

# Appendix A

# Appendix Title

## A.1 Variational Derivative of the Elastic Energy

The variational derivative of the elastic energy (Eqn. (2.8)) is given by the following part. The bending energy $E_b$ is

$$E_b = \frac{1}{2} \int_{\Sigma} \kappa H^2 ds$$

where $\Sigma$ is the $\kappa$ is the bending rigidity, $H$ is the mean curvature.

We have the geometric relations [54] [53]

$$H_t = -\left(\partial_s^2 + H^2\right) V + TH_s \tag{A.1}$$

$$s_{\alpha t} = (T_s + HV)s_{\alpha} \tag{A.2}$$

where $V$ is the outward normal velocity, $T$ is the tangential velocity, $\alpha$ is a parameterization of the membrane that bounds the vesicle ($0 \le \alpha \le 2\pi$).

Rewriting $E_b$ as

$$E_\kappa = \int_\Sigma \left( \frac{1}{2}\kappa H^2 \right) s_\alpha d\alpha \tag{A.3}$$

and taking time derivative of it, we have

$$
\begin{aligned}
\dot{E}_\kappa &= \int_\Sigma \left( \kappa H H_t \right) s_\alpha d\alpha + \int_\Sigma \left( \frac{1}{2}\kappa H^2 \right) s_\alpha t d\alpha \\
&= \kappa \int_\Sigma H \left( -\left( \partial_s^2 + H^2 \right) V + T H_s \right) s_\alpha d\alpha + \frac{1}{2} \int_\Sigma H^2 (T_s + HV) s_\alpha d\alpha \\
&= \kappa \int_\Sigma \partial_s V H_s ds + \kappa \int_\Sigma H H_s T ds - \frac{1}{2}\kappa \int_\Sigma T d(H^2) - \frac{1}{2}\kappa \int_\Sigma H^3 V ds \\
&= \kappa \int_\Sigma H_s dV + \kappa \int_\Sigma H H s T ds - \kappa \int_\Sigma H H_s T ds - \frac{1}{2}\kappa \int_\Sigma H^3 V ds \\
&= -\kappa \int_\Sigma V H_{ss} ds - \frac{1}{2}\kappa \int_\Sigma H^3 V ds \\
&= \int_\Sigma \left( -\kappa H_{ss} - \frac{\kappa}{2}H^3 \right) V ds
\end{aligned}
\tag{A.4}
$$

Here we use formula A.1 and A.2 in the second equality, and we apply the integration by parts to get the third and forth equality.

Similarly, the elastic energy can be rewritten as $E_\sigma = \int_\Sigma \sigma ds = \int_\Sigma \sigma s_\alpha d\alpha$. Take the time derivative, we have

$$
\begin{aligned}
\dot{E}_\sigma &= \int_\Sigma \dot{\sigma} ds + \int_\Sigma \sigma (T_s + HV) s_\alpha d\alpha \\
&= \int_\Sigma \dot{\sigma} ds + \int_\Sigma \sigma T_s ds + \int_\Sigma H \sigma V ds \\
&= \int_\Sigma \dot{\sigma} ds + \int_\Sigma \sigma dT + \int_\Sigma H \sigma V ds \\
&= \int_\Sigma \dot{\sigma} ds - \int_\Sigma T \sigma_s ds + \int_\Sigma H \sigma V ds
\end{aligned}
\tag{A.5}
$$

The force density $\mathbf{F}$ is the variational derivative of the free energy (Eqn. 2.8)[48], is given

by

$$\mathbf{F} = -\frac{\delta E}{\delta \mathbf{X}} = \left( \kappa \frac{\partial^2 H}{\partial s^2} + \frac{\kappa}{2} H^3 - H\sigma \right) \mathbf{n} + \frac{\partial \sigma}{\partial s} \mathbf{t} \qquad (A.6)$$

where $\mathbf{n}$ is the outward normal vector and $\mathbf{t}$ is the tangent vector.

## A.2 Numerical Discretization for a Vesicle

### A.2.1 Numerical Discretization

The discretization of the fluid equations are the same as the for the filament (Section 2.2.2). Here we calculate the free energy $E$ and force $\mathbf{F_X}$ for a vesicle[38].

Initially, a vesicle is considered as an ellipse with the nodes $\mathbf{X}_{[i]}$, $i = 1, 2, ..., N$ equally-distributed along the membrane with spacing $\Delta L = L/N$, where $L$ is the total arclength of the membrane. Nodes are connected by elastic springs with neighbors. $\mathbf{X}_{[N+1]} = \mathbf{X}_{[1]}$ because the vesicle is closed.

Let $\lambda_L$ be the elastic constant, then the spring potential is

$$E_L = \frac{\lambda_L}{2} \sum_{i=1}^{N} (\Delta s_{i,i+1} - \Delta L)^2, \qquad (A.7)$$

where $\Delta s_{i,i+1}$ is the arclength from $\mathbf{X}_{[i]}$ to $\mathbf{X}_{[i+1]}$. The tension between two neighboring nodes is

$$\mathbf{F}_{[i],L} = \lambda_L \left( \Delta s_{i,i+1} - \Delta L \right) \frac{\mathbf{X}_{[i+1]} - \mathbf{X}_{[i]}}{\left| \mathbf{X}_{[i+1]} - \mathbf{X}_{[i]} \right|}, \qquad (A.8)$$

for $i = 1, 2, \cdots, N$, acting on the $i$-th node and pointing to the $(i+1)$-th node.

The discrete bending energy is written as

$$E_\kappa = \frac{1}{2} \sum_{i=1}^{N} H_{[i]}^2 \Delta s_{i,i+1} \tag{A.9}$$

and the bending force density is given by

$$\mathbf{F}_{[i],\kappa} = -\left(\delta\mathbf{E}_\kappa/\delta\mathbf{X}\right)_{[i]} = \left(\kappa(H)_{ss,[i]} + \kappa H_{[i]}^3/2\right)\mathbf{n}_i, \quad \text{for } i = 1, 2, ..., N. \tag{A.10}$$

where $H_{[i]}$ is the mean curvature and $(H)_{ss,[i]}$ is its second derivative

The total force acting on the $i$-th node is the sum of the elastic and bending forces:

$$\mathbf{F}_{\mathbf{X}_{[i]}}(t) = \mathbf{F}_{[i],L} - \mathbf{F}_{[i-1],L} - \mathbf{F}_{[i],\kappa}, \quad \text{for } i = 1, 2, ..., N. \tag{A.11}$$

The average of the local surface tensions, $\sigma(t)$ can be calculated as:

$$\sigma(t) = \lambda_L(L_s(t) - L)/N, \tag{A.12}$$

where the $L_s(t) = \sum_{i=1}^{N} \Delta s_{i,i+1}$ is the total arclength of the discrete membrane.

## A.2.2 Convergence Test

Here we check the convergence for our numerical algorithm. We set the computational domain $\Omega$ to be a square with side length $L_C = 4 \times 10^{-4}m$. The initial shape of the vesicle is an ellipse with the aspect ratio $a : b = 1 : 0.4$. We choose the long axis $a = 2 \times 10^{-5}m$ and short axis $b = 0.8 \times 10^{-5}m$ to match the vesicle in the experiment [27], and use the same values of the parameters in the experiment (extensional flow rate $S = 4$, the bending stiffness is $\kappa = 10^{-19}J$). We set $\lambda_L = 4 \times 10^4 N/m$ to ensure the variation of local arclength is less than 0.1% for deterministic simulations, and 0.3% for stochastic simulations. We assume

that the fluid in the interior and exterior of the vesicle are water at the temperature 293K, i.e. $\eta = 10^{-3} Pa\ s$ and $\rho = 10^3 kg/m^3$. We use $N = 256$ to discretize the vesicle interface, and run the simulations up to $T = 0.1$s. We run the algorithms with time step $h = 10^{-5}$s, $h/2$, $h/4$, $h/8$ and $h/16$ and check the convergence in time by measuring the vesicle area and calculating the rate of convergence $r_C$ by

$$r_C = \log\left(|A_{\Delta t} - A_{\Delta t/2}|/|A_{\Delta t/2} - A_{\Delta t/4}|\right)/\log 2. \qquad (A.13)$$

The results for the deterministic and stochastic immersed boundary methods are summarized in Table A.1 and demonstrate that our numerical schemes are second-order convergent in time.

Table A.1: Convergence test in time for the vesicle area ($\Delta A = |(A_s - A_{s/2}|/A)$

| Time Step | Deterministic R-K 2 | | Stochastic R-K 2 | |
|---|---|---|---|---|
| | $\Delta A$ | $r_C$ | $\Delta A$ | $r_C$ |
| $\Delta t$ | - | - | - | |
| $\Delta t/2$ | 2.43e-8 | - | 3.68e-7 | - |
| $\Delta t/4$ | 6.08e-9 | 2.002 | 9.18e-8 | 2.004 |
| $\Delta t/8$ | 1.51e-9 | 2.008 | 2.34e-8 | 2.007 |

## A.3 Dynamics of Impermeable Vesicles in the Quiescent Fluid

The dynamics of impermeable vesicles in the quiescent fluid are shown in Figure A.1, and their equilibrium shape are shown in Figure 3.1. The initial shapes are ellipse with major axes $a = 2 \times 10^{-5}$ m and the minor axes $b$ decreasing from $2 \times 10^{-5}$ m to $0.6 \times 10^{-5}$ m.

The equilibrium shape for a circular vesicle is a circle (Figure A.1[a]), while as $\Delta$ increases,

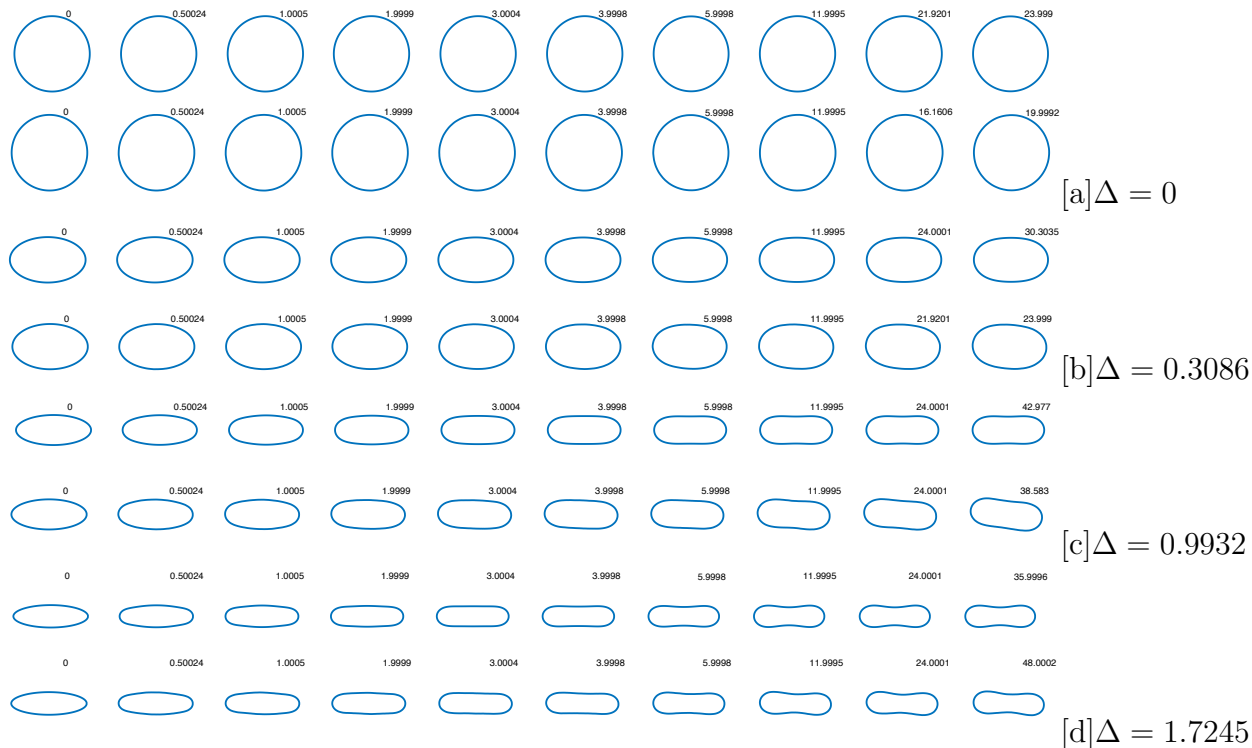the equilibrium shapes are more like biconcave.



Figure A.1: Dynamics of impermeable vesicles in the quiescent fluid with different excess arc length $\Delta$ at labeled time [a] $\Delta = 0$, [b] $\Delta = 0.3086$, [c] $\Delta = 0.9932$, [d]$\Delta = 1.7245$(top: deterministic, bottom: stochastic).

# A.4 Additional Realizations of Wrinkling Dynamics in Time-varying Extensional Flow

In Section 3.3.3, we presented a single realization of the stochastic dynamics of a single vesicle with excess area $\Delta = 0.994$ the extensional flow rate S $= 4$ and threshold $C_h = 100$. Here, we present multiple realizations for these cases to demonstrate that the results presented in Section 3.3.3 are characteristic.
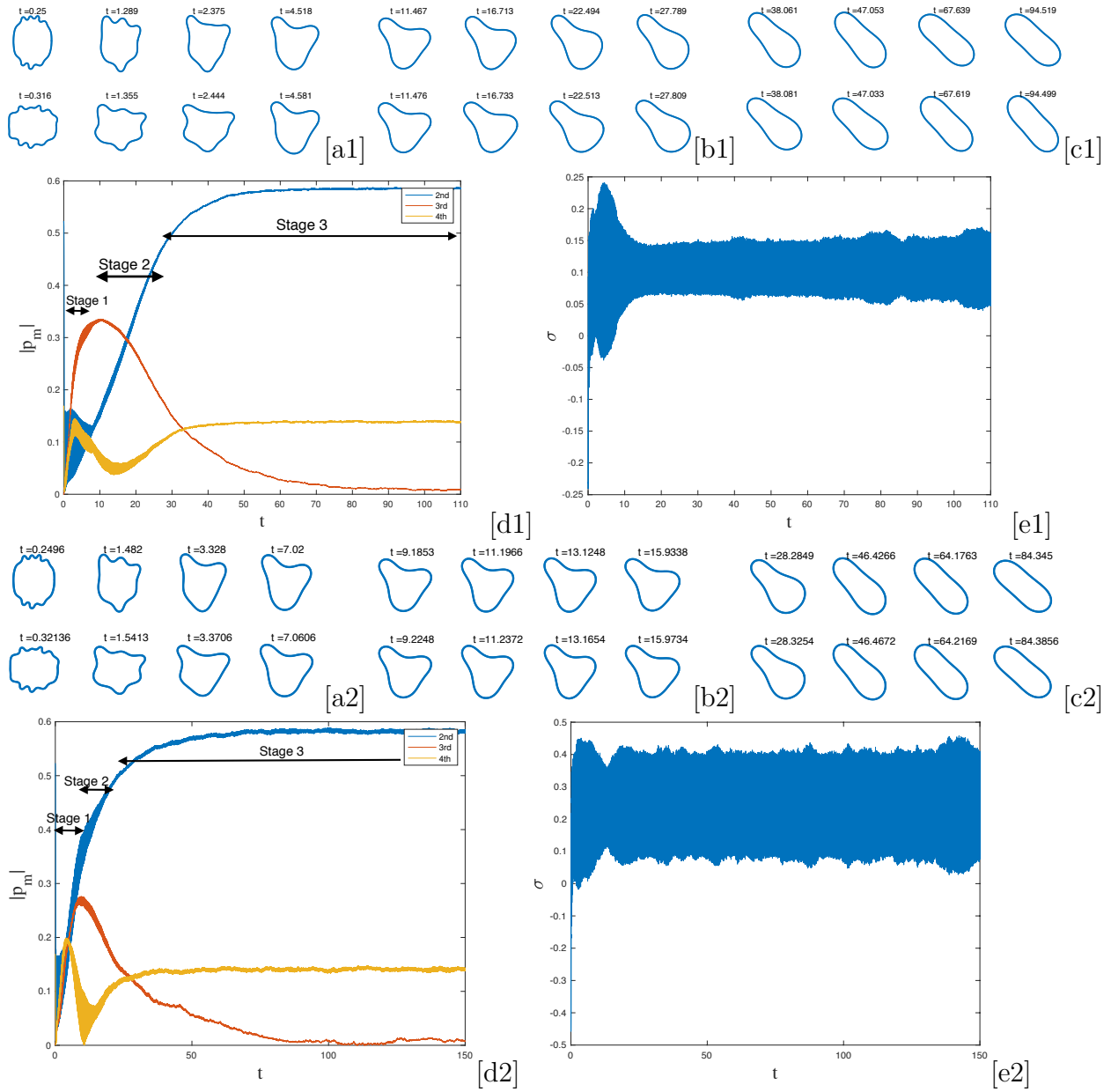
Figure A.2: Two Stochastic Realizations of Elongated Vesicles [a]Stage 1 [b] Stage 2 [c] Stage 3 [c] Fourier modes[d] Surface tension

103